M31N 2008-12a—THE REMARKABLE RECURRENT NOVA IN M31: PANCHROMATIC OBSERVATIONS OF THE 2015 ERUPTION

M. J. Darnley[1], M. Henze[2], M. F. Bode[1], I. Hachisu[3], M. Hernanz[2], K. Hornoch[4], R. Hounsell[5], M. Kato[6], J.-U. Ness[7], J. P. Osborne[8], K. L. Page[8], V. A. R. M. Ribeiro[9], P. Rodríguez-Gil[10,11], A. W. Shafter[12], M. M. Shara[13], I. A. Steele[1], S. C. Williams[1,14], A. Arai[15], I. Arcavi[16,17], E. A. Barsukova[18], P. Boumis[19], T. Chen[20], S. Fabrika[18,21], J. Figueira[22,23], X. Gao[24], N. Gehrels[25], P. Godon[26], V. P. Goranskij[27], D. J. Harman[1], D. H. Hartmann[28], G. Hosseinzadeh[16,29], J. Chuck Horst[12], K. Itagaki[30], J. José[22,23], F. Kabashima[31], A. Kaur[28], N. Kawai[32], J. A. Kennea[33], S. Kiyota[34], H. Kučáková[35], K. M. Lau[20], H. Maehara[36], H. Naito[37], K. Nakajima[37,38], K. Nishiyama[31], T. J. O'Brien[39], R. Quimby[12], G. Sala[22,23], Y. Sano[37,40], E. M. Sion[26], A. F. Valeev[18,21], F. Watanabe[37], M. Watanabe[41,42], B. F. Williams[43], and Z. Xu[44]

[1] Astrophysics Research Institute, Liverpool John Moores University, IC2 Liverpool Science Park, Liverpool, L3 5RF, UK; M.J.Darnley@ljmu.ac.uk
[2] Institut de Ciències de l'Espai (CSIC-IEEC), Campus UAB, C/Can Magrans s/n, E-08193 Cerdanyola del Valles, Spain; henze@ice.cat
[3] Department of Earth Science and Astronomy, College of Arts and Sciences, University of Tokyo, 3-8-1 Komaba, Meguro-ku, Tokyo 153-8902, Japan
[4] Astronomical Institute, Academy of Sciences, CZ-251 65 Ondřejov, Czech Republic
[5] Astronomy Department, University of Illinois at Urbana-Champaign, 1002 W. Green Street, Urbana, IL 61801, USA
[6] Department of Astronomy, Keio University, Hiyoshi, Yokohama 223-8521, Japan
[7] European Space Astronomy Centre, Camino Bajo del Castillo s/n, Urb. Villafranca del Castillo, E-28692 Villanueva de la Cañada, Madrid, Spain
[8] X-Ray and Observational Astronomy Group, Department of Physics & Astronomy, University of Leicester, LE1 7RH, UK
[9] Department of Astrophysics/IMAPP, Radboud University, P.O. Box 9010, 6500 GL Nijmegen, The Netherlands
[10] Instituto de Astrofísica de Canarias, Vía Láctea, s/n, La Laguna, E-38205, Santa Cruz de Tenerife, Spain
[11] Departamento de Astrofísica, Universidad de La Laguna, La Laguna, E-38206, Santa Cruz de Tenerife, Spain
[12] Department of Astronomy, San Diego State University, San Diego, CA 92182, USA
[13] American Museum of Natural History, 79th Street and Central Park West, New York, NY 10024, USA
[14] Physics Department, Lancaster University, Lancaster, LA1 4 YB, UK
[15] Koyama Astronomical Observatory, Kyoto Sangyo University, Motoyama, Kamigamo, Kita-ku, Kyoto, Kyoto 603-8555, Japan
[16] Las Cumbres Observatory Global Telescope Network, 6740 Cortona Dr., Suite 102, Goleta, CA 93117, USA
[17] Kavli Institute for Theoretical Physics, University of California, Santa Barbara, CA 93106-4030, USA
[18] Special Astrophysical Observatory of Russian Academy of Sciences, Nizhnij Arkhyz, Karachai-Cherkessian Republic 369167, Russia
[19] Institute for Astronomy, Astrophysics, Space Applications and Remote Sensing, National Observatory of Athens, 15236 Penteli, Greece
[20] Corona Borealis Observatory, Kunsha Town, Ngari, Tibet, PR China
[21] Kazan Federal University, Kazan 420008, Russia
[22] Departament de Física, EUETIB, Universitat Politècnica de Catalunya, c/Compte d'Urgell 187, E-08036 Barcelona, Spain
[23] Institut d'Estudis Espacials de Catalunya, c/Gran Capità 2-4, Ed. Nexus-201, E-08034, Barcelona, Spain
[24] Xingming Observatory, Mt. Nanshan, Urumqi, Xinjiang, PR China
[25] Astrophysics Science Division, NASA Goddard Space Flight Center, Greenbelt, MD 20771, USA
[26] Department of Astronomy and Astrophysics, Villanova University, 800 Lancaster Avenue, Villanova, PA 19085, USA
[27] Sternberg Astronomical Institute, Moscow University, Universitetsky Prospect, 13, Moscow 119899, Russia
[28] Department of Physics and Astronomy, Clemson University, Clemson, SC 29634, USA
[29] Department of Physics, University of California, Santa Barbara, CA 93106-9530, USA
[30] Itagaki Astronomical Observatory, Teppo, Yamagata 990-2492, Japan
[31] Miyaki-Argenteus Observatory, Miyaki, Saga 840-1102, Japan
[32] Department of Physics, Tokyo Institute of Technology, 2-12-1 Ookayama, Meguro-ku, Tokyo 152-8551, Japan
[33] Department of Astronomy and Astrophysics, 525 Davey Lab, Pennsylvania State University, University Park, PA 16802, USA
[34] Variable Stars Observers League in Japan (VSOLJ), 7-1 Kitahatsutomi, Kamagaya 273-0126, Japan
[35] Astronomical Institute of the Charles University, Faculty of Mathematics and Physics, V Holešovičkách 2, 180 00 Praha 8, Czech Republic
[36] Okayama Astrophysical Observatory, NAOJ, NINS, 3037-5 Honjo, Kamogata, Asakuchi, Okayama 719-0232, Japan
[37] Nayoro Observatory, 157-1 Nisshin, Nayoro, Hokkaido 096-0066, Japan
[38] Rikubetsu Space and Earth Science Museum, Uenbetsu, Rikubetsu-cho, Ashoro, Hokkaido 089-4301, Japan
[39] Jodrell Bank Centre for Astrophysics, Alan Turing Building, University of Manchester, Manchester, M13 9PL, UK
[40] Observation and Data Center for Cosmosciences, Faculty of Science, Hokkaido University, Kita-ku, Sapporo, Hokkaido 060-0810, Japan
[41] Department of Cosmosciences, Hokkaido University, Kita 10, Nishi 8, Kita-ku, Sapporo, Hokkaido 060-0810, Japan
[42] Department of Applied Physics, Okayama University of Science, 1-1 Ridai-cho, Kita-ku, Okayama, Okayama 700-0005, Japan
[43] Department of Astronomy, Box 351580, University of Washington, Seattle, WA 98195, USA
[44] Nanjing Putian Telecommunications Co., Ltd., 1 Putian Rd, Qinhuai, Nanjing, 210012 Jiangsu, PR China

ABSTRACT

The Andromeda Galaxy recurrent nova M31N 2008-12a had been observed in eruption 10 times, including yearly eruptions from 2008 to 2014. With a measured recurrence period of $P_{\rm rec} = 351 \pm 13$ days (we believe the true value to be half of this) and a white dwarf very close to the Chandrasekhar limit, M31N 2008-12a has become the leading pre-explosion supernova type Ia progenitor candidate. Following multi-wavelength follow-up observations of the 2013 and 2014 eruptions, we initiated a campaign to ensure early detection of the predicted 2015 eruption, which triggered ambitious ground- and space-based follow-up programs. In this paper we present the 2015 detection, visible to near-infrared photometry and visible spectroscopy, and ultraviolet and X-ray observations from the *Swift* observatory. The LCOGT 2 m (Hawaii) discovered the 2015 eruption, estimated to have commenced at August 28.28 ± 0.12 UT. The 2013–2015 eruptions are remarkably similar at all wavelengths. New early spectroscopic observations reveal short-lived emission from material with velocities ~13,000 km s^{-1},

possibly collimated outflows. Photometric and spectroscopic observations of the eruption provide strong evidence supporting a red giant donor. An apparently stochastic variability during the early supersoft X-ray phase was comparable in amplitude and duration to past eruptions, but the 2013 and 2015 eruptions show evidence of a brief flux dip during this phase. The multi-eruption *Swift*/XRT spectra show tentative evidence of high-ionization emission lines above a high-temperature continuum. Following Henze et al. (2015a), the updated recurrence period based on all known eruptions is $P_{rec} = 174 \pm 10$ days, and we expect the next eruption of M31N 2008-12a to occur around 2016 mid-September.

1. INTRODUCTION

Novae are powerful eruptions resulting from a brief thermonuclear runaway (TNR) occurring at the base of the surface layer of an accreting white dwarf (WD; see Schatzman 1949, 1951; Gurevitch & Lebedinsky 1957; Cameron 1959; Starrfield et al. 1972, 2008, 2016; José & Shore 2008; José 2016, for recent reviews). Belonging to the group of cataclysmic variables (Sanford 1949; Joy 1954; Kraft 1964), the companion star in these interacting close-binary systems transfers hydrogen-rich material to the WD usually via an accretion disk around the WD. The TNR powers an explosive ejection of the accreted material, with a rapidly expanding pseudo-photosphere initially increasing the visible luminosity of the system by up to eight orders of magnitude (see Bode & Evans 2008; Bode 2010; Woudt & Ribeiro 2014, for recent reviews). Following the TNR the nuclear fusion enters a period of short-lived, approximately steady-state burning until the accreted fuel is exhausted, partly because it has been ejected and partly because what remained has been burned to helium (Prialnik et al. 1978). As the optical depth of the expanding ejecta becomes progressively smaller, the pseudo-photosphere begins to recede back toward the WD surface, subsequently shifting the peak of the emission back to higher energies until ultimately a supersoft X-ray source (SSS) may emerge (see, for example, Hachisu & Kato 2006; Krautter 2008; Osborne 2015). The "turn-off" of the SSS indicates the end of the nuclear burning, after which the system eventually returns to its quiescent state.

All nova eruptions are inherently recurrent, with the WD and companion surviving each eruption, and accretion reestablishing or continuing shortly afterward. By definition, classical novae (CNe) have had a single *observed* eruption, whereas recurrent novae (RNe) have been detected in eruption at least twice. Observed intervals between eruptions range from ~1 year (Darnley et al. 2014b, for M31N 2008-12a) up to 98 years (Schaefer 2010, for V2487 Ophiuchi), with the shortest predicted recurrence period—albeit derived from incomplete observational data—being just six months (Henze et al. 2015a). The theoretical limits on the recurrence period of all novae may be as short as 50 days (Hillman et al. 2015) or even 25 days (Hachisu et al. 2016)[45] and as long as mega-years (see, for example, Starrfield et al. 1985; Kovetz & Prialnik 1994; Yaron et al. 2005). The shorter recurrence periods are driven by a combination of a high-mass WD and a high mass accretion rate. Such high accretion rates are typically driven by an evolved companion star, such as a Roche lobe overflowing sub-giant star (SG-novae; also the U Scorpii type of RNe) or

the stellar wind from a red giant companion (RG-novae: symbiotic novae, or the RS Ophiuchi type RNe; see Darnley et al. 2012, 2014a, for recent reviews).

With the most luminous novae reaching peak visible magnitudes $M_V < -10$ (Shafter et al. 2009, S. C. Williams et al. 2017, in preparation), novae are readily observable out to the distance of the Virgo Cluster and beyond (see, for example, Curtin et al. 2015; Shara et al. 2016). But it is the nearby Andromeda Galaxy (M 31), with an annual nova rate of 65^{+16}_{-15} yr^{-1} (Darnley et al. 2006), that provides the leading laboratory for the study of galaxy-wide nova populations (see, for example, Ciardullo et al. 1987, 1990a; Shafter & Irby 2001; Darnley et al. 2004, 2006; Henze et al. 2008, 2010, 2011, 2014b; Shafter et al. 2011a, 2011b, 2015a; Williams et al. 2014, 2016). Since the discovery of the first M 31 nova by Ritchey (1917, also spectroscopically confirmed) and the pioneering work of Hubble (1929), more than 1000 nova candidates have been discovered (see Pietsch et al. 2007; Pietsch 2010, and their on-line database[46]), with over 100 now spectroscopically confirmed (see, for example, Shafter et al. 2011b).

Recently, pioneering X-ray surveys with *XMM-Newton* and *Chandra* have revealed that novae are the major class of SSSs in M 31 (Pietsch et al. 2005, 2007). A dedicated multi-year follow-up program with the same telescopes studied the multi-wavelength population properties of M 31 novae in detail (Henze et al. 2010, 2011, 2014b). A major result of this work was the discovery of strong correlations between various observable parameters, indicating that novae with a faster visible decline tend to show a shorter SSS phase with a higher temperature (Henze et al. 2014b). This is consistent with the trends seen in Galactic novae (see Schwarz et al. 2011). Theoretical models indicate that a shorter SSS phase corresponds to a higher-mass WD (e.g., Hachisu & Kato 2006, 2010; Wolf et al. 2013). Thus, the M 31 nova population provides a unique framework within which to understand the properties of individual novae and their ultimate fate.

Supernovae Type Ia (SNe Ia) are the outcome of a thermonuclear explosion of a carbon–oxygen (CO) WD as it reaches and surpasses the Chandrasekhar (1931) mass limit (see, for example, Whelan & Iben 1973; Hachisu et al. 1999a, 1999b; Hillebrandt & Niemeyer 2000). An accreting oxygen–neon WD, however, is predicted to undergo electron capture and subsequent neutron star formation (see, for example, Gutierrez et al. 1996). It seems increasingly likely that there is not a single progenitor pathway producing all observed SNe Ia but a combination of different double-degenerate (WD–WD) and single-degenerate (SD; WD–donor) binary systems, with the

---

[45] In both the Hillman et al. (2015) and Hachisu et al. (2016) studies, accretion is assumed to completely stop during the eruption period.

[46] http://www.mpe.mpg.de/~m31novae/opt/m31/index.php

Table 1
List of All Observed Eruptions of M31N 2008-12a

Eruption Date[a] (UT)	SSS-on Date[b] (UT)	Days Since Last Eruption[c]	Detection Wavelength (Observatory)	References
(1992 Jan 28)	1992 Feb 03	...	X-ray (*ROSAT*)	(1), (2)
(1993 Jan 03)	1993 Jan 09	341	X-ray (*ROSAT*)	(1), (2)
(2001 Aug 27)	2001 Sep 02	...	X-ray (*Chandra*)	(2), (3)
2008 Dec 25	...	...	Visible (Miyaki-Argenteus)	(4)
2009 Dec 02	...	342	Visible (PTF)	(5)
2010 Nov 19	...	352	Visible (Miyaki-Argenteus)	(2)
2011 Oct 22.5	...	337.5	Visible (ISON-NM)	(5), (6)–(8)
2012 Oct 18.7	<2012 Nov 06.45	362.2	Visible (Miyaki-Argenteus)	(8)–(11)
2013 Nov 26.95 ± 0.25	≤2013 Dec 03.03	403.5	Visible (iPTF); UV/X-ray (*Swift*)	(5), (8), (11)–(14)
2014 Oct 02.69 ± 0.21	2014 Oct 08.6 ± 0.5	309.8 ± 0.7	Visible (LT); UV/X-ray (*Swift*)	(8), (15)
2015 Aug 28.28 ± 0.12	2015 Sep 02.9 ± 0.7	329.6 ± 0.3	Visible (LCOGT); UV/X-ray (*Swift*)	(14), (16)–(18)

Notes. Modified and updated version of Table 1 from Tang et al. (2014), Darnley et al. (2015e), and Henze et al. (2015a).
[a] Estimated times of the visible eruption; those in parentheses have been extrapolated from the X-ray data (see Henze et al. 2015a). The rapid evolution of the eruption (see Figure 1) limits any associated uncertainties to just a few days.
[b] Turn-on time of the SSS emission. The *ROSAT* detections from 1992 and 1993 permit accurate estimates of SSS-on. There was only a single *Chandra* data point obtained on 2001 September 08, sometime during the 12 day SSS phase (cf. Figure 4). Therefore, we take September 08 as the midpoint of the SSS phase (with an uncertainty of ±6 days) to extrapolate the eruption date and SSS-on.
[c] Time since last eruption only quoted when consecutive detections occurred in consecutive years, under the assumption of $P_{rec} \simeq 1$ year. Time is taken as the period between estimated eruption dates.
References. (1) White et al. (1995), (2) Henze et al. (2015a), (3) Williams et al. (2004), (4) Nishiyama & Kabashima (2008), (5) Tang et al. (2014), (6) Korotkiy & Elenin (2011), (7) Barsukova et al. (2011), (8) Darnley et al. (2015e), (9) Nishiyama & Kabashima (2012), (10) Shafter et al. (2012), (11) Henze et al. (2014a), (12) Tang et al. (2013), (13) Darnley et al. (2014b), (14) this paper, (15) Henze et al. (2015d), (16) Darnley et al. (2015b), (17) Darnley et al. (2015d), (18) Henze et al. (2015c).

metallicity and age of the parent stellar population possibly determining the weighting of those pathways (see, for example, Maoz et al. 2014). Novae, particularly RNe with their already high mass WDs, are potentially a leading SD pathway. Recent studies have indicated that the mass of a WD can indeed grow over time in RN systems (see, for example, Hernanz & José 2008; Starrfield et al. 2012; Hillman et al. 2016). A number of questions remain over the size of their contribution to the SN Ia rate, including the composition of the WD in RN systems, the feasibility of growing a CO WD from their formation mass to the Chandrasekhar limit, and the size of the population of high-mass WD novae. Of course, the lack of observational signatures of hydrogen following *most* SN Ia explosions still provides a significant hurdle for the SD scenario (see, for example, Wang & Han 2012; Maoz et al. 2014). But the unmistakable presence of hydrogen in PTF 11kx (Dilday et al. 2012) and the possible presence of hydrogen in SN 2013ct (Maguire et al. 2016) support the view that at least some SNe Ia arise in SD systems.

At the time of writing, there have been around 450 detected eruptions of nova candidates in the Milky Way (Darnley et al. 2014a), of which just ten confirmed RN systems are known (Schaefer 2010), accounting for ~3% of known Galactic nova systems or ~9% of detected Galactic eruptions. A number of recent detailed studies of archival observations have uncovered new results relating to the RN populations of both the Milky Way and M 31, which are summarized below:

Pagnotta & Schaefer (2014) used a combination of three different methods to estimate that the RN population (essentially $10 \leqslant P_{rec} \leqslant 100$ years; A. Pagnotta 2016, private communication) of the Milky Way is 25 ± 10% of the Galactic nova population. However, the range of methodologies employed predicted a wide range of contributions, from 9%–38%, with the authors themselves indicating that the statistical

errors are likely to be "much too small" (Pagnotta & Schaefer 2014).

Shafter et al. (2015a) uncovered multiple eruptions of 16 RN systems in M 31. The subsequent analysis predicted a historic M 31 RN discovery efficiency of just 10% and that as many as 33% of M 31 nova eruptions may arise from RN systems ($P_{rec} \leqslant 100$ years).

Williams et al. (2014, 2016) employed a different approach: by recovering the progenitor systems of 11 M 31 RG-novae, they determined that $30^{+13}_{-10}\%$ of all M 31 nova eruptions occur in RG-nova systems, a sub-population that also appears to be strongly associated with the M 31 disk.

Additionally, other recent results for the Milky Way (Shafter 2016), Magellanic Clouds (Mróz et al. 2016), M 31 (Chen et al. 2016; Soraisam et al. 2016), and M 87 (Shara et al. 2016) all indicate that the luminosity-specific nova rate (see, for example, Ciardullo et al. 1990b) may be much higher than previously thought. Together, all these results boost the size of the available "pool" of novae that may contribute to the SN Ia population by a factor of >5.

2. A REMARKABLE RN

M31N 2008-12a was originally discovered far out in the disk of M 31 in visible observations while undergoing an eruption in 2008 (Nishiyama & Kabashima 2008). Subsequent eruptions were discovered in each of the next six years: 2009 (Tang et al. 2014, first reported in 2013), 2010 (Henze et al. 2015a, only recovered in 2015), 2011 (Korotkiy & Elenin 2011), 2012 (Nishiyama & Kabashima 2012), 2013 (Tang et al. 2013), and 2014 (Darnley et al. 2014c). See Table 1 for a summary of all detected eruptions. Henze et al. (2015a; hereafter, HDK15) calculated that the mean recurrence period, based only on these seven consecutive eruptions, is $P_{rec} = 351 \pm 13$ days.

Henze et al. (2014a; hereafter, HND14) and Tang et al. (2014; hereafter, TBW14) independently uncovered earlier eruptions from 1992, 1993, and 2001. These were based on archival X-ray data from *ROSAT* and *Chandra* first reported by White et al. (1995) and Williams et al. (2004), respectively. Using these additional eruptions, HDK15 predicted that the actual mean recurrence period of M31N 2008-12a is only $P_{rec} = 175 \pm 11$ days and subsequently predicted that the next *observable* eruption would occur between early 2015 September and mid-October.

The shortest observed inter-eruption period seen in the Galactic nova population is eight years, between the 1979 and 1987 eruptions of U Scorpii (Bateson & Hull 1979; Overbeek et al. 1987, respectively). The Large Magellanic Cloud recurrent nova LMCN 1968-12a (Shore et al. 1991) may have an eruption cycle of only six years (Darnley et al. 2016b). Furthermore, a five-year cycle has been observed for the M 31 nova M31N 1963-09c (Shafter et al. 2015a; Williams et al. 2015), and a four-year cycle for M31N 1997-11k (Shafter et al. 2015a). Nevertheless, the discovery of a nova with a recurrence period as short as one year or even six months presents an unprecedented and significant advance over any of these objects. Such a short recurrence period suggests the presence of a WD with a mass very close to the Chandrasekhar mass (see, for example, Prialnik & Kovetz 1995; Yaron et al. 2005; Wolf et al. 2013; Kato et al. 2014). Based on population synthesis models, Chen et al. (2016) predicted that the nova rate for systems with $P_{rec} < 1$ year in "M 31-like" galaxies should be ~ 4 yr^{-1}, whereby M31N 2008-12a *could* account for 2 yr^{-1} in M 31. But the question of the true population size of such ultra-short-cycle RNe remains an open one.

The 2012 eruption of M31N 2008-12a was chronologically the third to be discovered but spectroscopically the first to be confirmed (Shafter et al. 2012), and it provided the first hint of the true nature and short recurrence period of this system. Subsequently, the 2013 eruption was expected, and results of visible, UV, and X-ray observations were published by Darnley et al. (2014b; hereafter, DWB14) and HND14 and independently by TBW14. By employing the technique developed by Bode et al. (2009), Williams et al. (2013) recovered the progenitor system from archival *Hubble Space Telescope* (*HST*) data. These *HST* visible and near-UV (NUV) photometric data indicated the presence of a bright accretion disk, similar in luminosity to that seen around RS Oph (DWB14, TBW14; also see Evans et al. 2008, for detailed reviews of the RS Oph system). *Swift* X-ray observations began six days after the 2013 discovery and immediately revealed the presence of SSS emission (HND14). Blackbody fits to the X-ray spectra indicated a particularly hot source (~ 100 eV) compared to the M 31 nova population (see Henze et al. 2014b). The SSS phase lasted for only twelve days; at the time, M31N 2008-12a had the fastest SSS turn-on and turn-off ever observed (these were both surpassed by the 2014 eruption of the Galactic RN V745 Scorpii, an RG-nova; see Page et al. 2015 and Section 7.6). The X-ray properties pointed to a combination of a high-mass WD and low ejected mass, with the *HST* data indicating a high mass accretion rate. Modeling of the system reported by TBW14 pointed toward $M_{WD} > 1.3\,M_{\odot}$ and $\dot{M} > 1.7 \times 10^{-7}\,M_{\odot}$ yr^{-1}.

A successful campaign to discover the predicted 2014 eruption was reported by Darnley et al. (2015e; hereafter, DHS15). The discovery triggered a swathe of pre-planned high-cadence visible, UV, and X-ray observations, led by the fully robotic 2 m Liverpool Telescope (LT; Steele et al. 2004) from the ground and by *Swift* from low-Earth orbit. DHS15 reported a visible light curve that evolved faster than all known Galactic RNe ($t_3(V) = 3.84 \pm 0.24$ days; also see Section 5.2) before entering a short-lived "plateau" phase, as seen in other RNe (see, for example, Pagnotta & Schaefer 2014). The plateau coincided approximately with the start of the SSS phase (see HND15). A series of visible spectra was collected, the first just 1.27 days after the eruption, and these showed modest expansion velocities ($\bar{v}_{ej} = 2600 \pm 100$ km s^{-1}) for such a fast nova, which significantly decreased over the course of just a few days. Such an inferred deceleration is reminiscent of the interaction of the ejecta with pre-existing circumbinary material (such as the red giant wind in the case of RS Oph; Bode & Kahn 1985; Bode et al. 2006).

Independently of any eruptions from the system, DHS15 also reported that deep Hα imaging of M31N 2008-12a at quiescence uncovered a vastly extended elliptical shell centered on the system; the structure is larger than most Galactic supernova remnants. Serendipitous spectra of the shell obtained during the 2014 eruption revealed strong Hα, [N II] (6584 Å), and [S II] (6716/6731 Å) emission (DHS15). The measured [S II]/Hα ratio and the lack of any [O III] emission suggest a non-SN origin and hence a possible association with M31N 2008-12a.

Henze et al. (2015b; hereafter, HND15) reported the fruits of an intensive X-ray follow-up campaign of the 2014 eruption using *Swift*. Their main results included a precise measurement of the SSS turn-on time (5.9 ± 0.5 day), a fast effective temperature evolution during the SSS phase, and a strong aperiodic X-ray variability that decreased significantly around day 14 after eruption. HND15 found the 2014 SSS properties to be remarkably similar to those of the 2013 eruption.

Theoretical studies of hypothetical systems similar to M31N 2008-12a (before such a short recurrence period system was discovered) consistently show that the combination of a high-mass WD and a high mass accretion rate is required to achieve a short recurrence period and drive the rapid turn-on of a short-lived SSS phase (see, for example Yaron et al. 2005). Based on a recurrence period of 1 year, Kato et al. (2015) determined that the M31N 2008-12a eruptions are consistent with a WD mass of $1.38\,M_{\odot}$, an accretion rate $\dot{M} = 1.6 \times 10^{-7}\,M_{\odot}$ yr^{-1}, and an ejected mass of $\sim 0.6 \times 10^{-7}\,M_{\odot}$, leading to a mass accumulation efficiency of the WD of $\eta \simeq 0.63$—i.e., the WD retains 63% of the accreted material and therefore is expected to be increasing in mass.

Overall, the striking similarities between the past eruptions facilitated the development of a detailed observing strategy for the detection and follow-up of the expected 2015 eruption.

3. QUIESCENT MONITORING AND DETECTION OF THE 2015 ERUPTION

Following the 2014 eruption of M31N 2008-12a, a dedicated quiescent monitoring campaign was again put in place to detect the next eruption, as had been employed to discover the 2014 eruption (DHS15). For the 2015 eruption detection campaign, a large array of telescopes was employed. These included the Kiso Schmidt Telescope, the Okayama Telescope, and the Miyaki-Argenteus Observatory, all in Japan; the Xingming Observatory, China; the Ondřejov Observatory, Czech Republic; Montsec Observatory, Spain; and the Kitt Peak

Observatory, USA. The majority of the quiescent monitoring was performed by three facilities, the sister telescopes LT and Las Cumbres Observatory Global Telescope Network (LCOGT) 2 m telescope on Haleakala, Hawaii (formally, the Faulkes Telescope North), and the *Swift* observatory.

The LT began monitoring the system immediately after the cessation of the 2014 eruption, although these observations were tempered by the diminishing visibility of M 31. From 2015 May 27 onward, the LT obtained nightly (weather permitting) observations at the position of M31N 2008-12a using the IO:O visible CCD camera[47] (a 4096 × 4112 pixel e2v detector which provided a $10' \times 10'$ field of view). From 2015 June 10 onward, the LT data were supplemented by observations from LCOGT (2 m, Hawaii; Brown et al. 2013), which employed the Spectral visible CCD camera[48] (a 4k × 4k pixel detector providing a $10.'5 \times 10.'5$ field of view).

Each LT and LCOGT observation consisted of a single 60 s exposure taken through a Sloan-like r'-band filter, with a target cadence of 24 hr—although this was decreased to 2 hr within the ∼1σ eruption prediction window (from the night beginning 2015 July 30 onward; HDK15). The LT and LCOGT data were automatically pre-processed by a pipeline running at the LT and LCOGT, respectively, and were automatically retrieved, typically within minutes of the observation. An automatic data analysis pipeline (based on a real-time M 31 difference image analysis pipeline; see Darnley et al. 2007; Kerins et al. 2010) then further processed the data and searched for transient objects in real time. Any object detected with significance ⩾5σ above the local background, within one seeing-disk of the position of M31N 2008-12a, would generate an automatic alert.

An ambitious *Swift* program to monitor the quiescent system with the aim of detecting the predicted initial X-ray flash of the eruption (Kato et al. 2015) was also active. Full details of this campaign are to be reported in a companion paper (Kato et al. 2016). While focusing on X-ray emission, the *Swift* UV/optical telescope (UVOT; Roming et al. 2005) was also employed to monitor the system. To complement the UVOT observations, the LT monitoring program included additional Sloan u'-band observations from 2015 August 16.121 UT onward.

A transient was detected with high significance in LCOGT r'-band data taken on 2015 August 28.425 ± 0.001 UT by the automated pipeline at a position of $\alpha = 0^h45^m28.^s82$, $\delta = 41°54'10.''0$ (J2000), with separations of $0.''09 \pm 0.''07$ and $0.''16 \pm 0.''07$ from the position of the 2013 (DWB14) and 2014 (DHS15) eruptions, respectively. Preliminary photometry at the time (see Appendix A.1 for detailed photometric analysis) indicated that this object had a magnitude of $r' = 19.09 \pm 0.04$, around one magnitude below the peak brightness of previous eruptions of M31N 2008-12a (DWB14, DHS15, TBW14). Our pre-planned follow-up observations were immediately triggered, and a request for further observations was released (Darnley et al. 2015b).

A transient was also detected in the *Swift* UVOT uvw1 data with $m_{w1} = 17.7 \pm 0.1$ at the position of M31N 2008-12a taken on 2015 August 28.41 UT—marginally before the LCOGT detection. However, the longer data retrieval time for *Swift* meant these data were received and processed after the LCOGT data.

No object was detected at the position of M31N 2008-12a in an LT IO:O observation 0.265 ± 0.001 days earlier down to a 3σ limiting magnitude of $r' > 21.8$. Additional LT IO:O observations 0.353 ± 0.001 and 0.444 ± 0.001 days before detection also detected no sources down to $r' > 21.8$. LT Sloan u'-band observations taken 0.452 ± 0.001, 0.442 ± 0.001, and 0.264 ± 0.001 days before the LCOGT detection found no source at the position of M31N 2008-12a down to limits of $u' > 19.8, > 21.6$, and >21.5, respectively. Similarly, no object was detected in the *Swift* UVOT uvw1 data on 2015 August 28.01 down to a 3σ limit of $m_{w1} > 20.3$.

A full analysis of all the inter-eruption (quiescent) data will be published in a later paper.

4. OBSERVATIONS OF THE 2015 ERUPTION

In this section we will describe the strategy and various data analysis techniques employed for the near-infrared (NIR), visible, UV, and X-ray follow-up observations of the 2015 eruption of M31N 2008-12a.

4.1. Visible and NIR Photometry

The 2015 eruption of M31N 2008-12a was followed photometrically by a large number of ground-based visible/NIR facilities. These include the aforementioned LT and LCOGT, the Mount Laguna Observatory (MLO) 1.0 m, the Ondřejov Observatory 0.65 m, the Bolshoi Teleskop Alt-azimutalnyi (BTA) 6.0 m, the Corona Borealis Observatory (CBO) 0.3 m, the Nayoro Observatory of Hokkaido University 1.6 m Pirka telescope, the Okayama Astrophysical Observatory (OAO) 0.5 m MITSuME telescope, and the iTelescope.net T24. The data acquisition and analysis for each of these facilities are described in detail in Appendix A. The resulting photometric data are presented in Table 11, and the subsequent light curves are shown in Figure 1. Where near-simultaneous multi-color observations are available *from the same facility*, the color data are presented in Table 12, and the color evolution plots are shown in Figure 2.

4.2. Visible Spectroscopy

The primary aim of spectroscopy of the 2015 eruption was to obtain the earliest spectra post-eruption and to confirm the nature of the apparent ejecta deceleration reported by DHS15. Spectroscopy was obtained by the LT, LCOGT, and Kitt Peak National Observatory 4 m telescope. The text in Appendix B describes the resulting data acquisition and processing, and a log of the spectroscopic observations is provided in Table 2.

4.3. Swift X-Ray and UV Observations

The high-cadence *Swift* observations employed for the initial X-ray flash monitoring of M31N 2008-12a (see Kato et al. 2016) were continued for a further 20 days following the eruption to study the UV and X-ray light curves of the eruption. The observations are summarized in Table 13.

The decline of the UV light curve and the early SSS phase received a high-cadence coverage with on average a single 1 ks pointing obtained every six hours (see Table 13). However, the coverage of the later SSS light curve was occasionally interrupted by higher-priority observations, such as γ-ray bursts. This resulted in the omission of certain ObsIDs in the otherwise consecutive list in Table 13. Some other ObsIDs
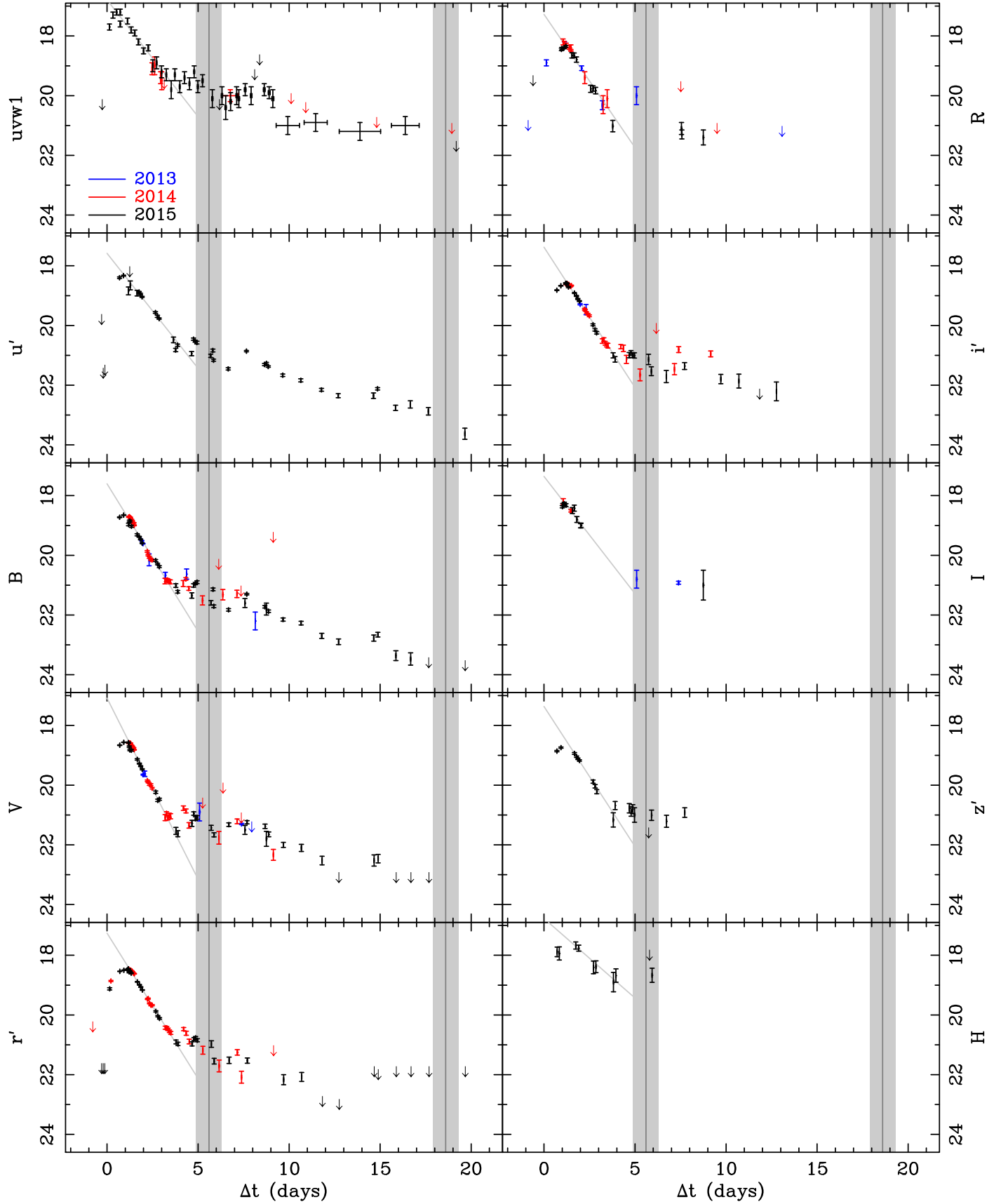

Figure 1. Near-ultraviolet through near-infrared photometry of the 2013–2015 eruptions of M31N 2008-12a. Black points indicate the 2015 eruption, with all data taken from Tables 11 and 13; red points indicate data from the 2014 eruption (DHS15; HND15); and blue points indicate the 2013 eruption (DWB14; TBW14). The vertical gray lines indicate the turn-on and turn-off times of the SSS from the 2015 eruption (the shaded areas, their associated uncertainties). The gray lines show a linear fit (an exponential decay in luminosity) to each light curve over the interval $1 \leqslant \Delta t \leqslant 4$ days (see Table 4 for the decline times and other characteristics).
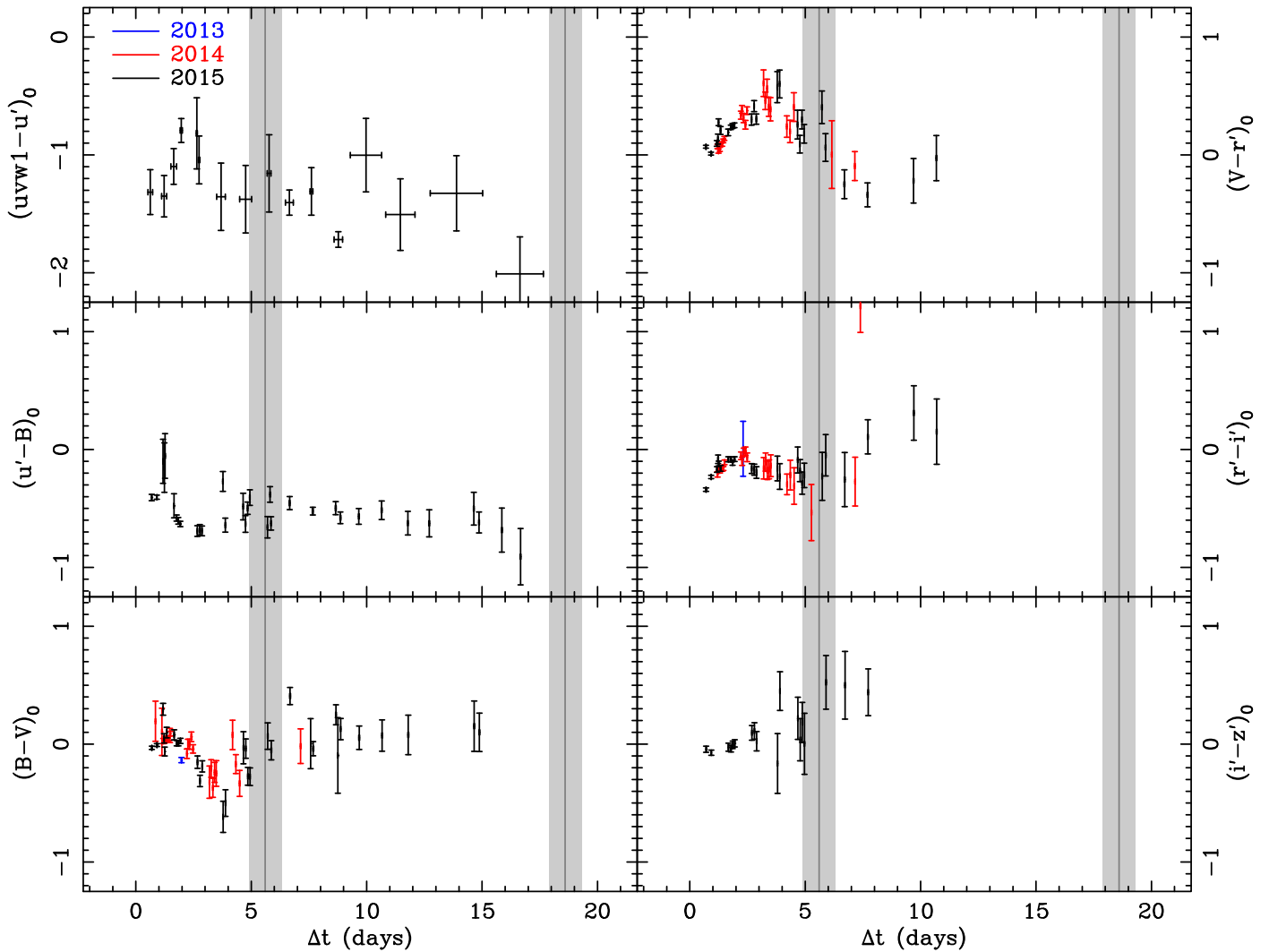
Figure 2. Similar to Figure 1 but showing the dereddened color evolution of the eruptions of M31N 2008-12a, assuming $E_{B-V} = 0.096 \pm 0.026$ (M. J. Darnley et al. 2017, in preparation). The (uvw1–u')$_0$ plot uses a different y-axis and mixes 2014 and 2015 uvw1 data.

were not included because they collected less than 20 s of exposure. In the text of this paper, individual *Swift* observations are referred to by their segment ID (e.g., "ObsID 123" is shorthand for ObsID 00032613123).

All our *Swift* data analysis is based on the cleaned level 2 files locally reprocessed at the *Swift* UK Data Centre[49] with HEASOFT (v6.15.1). For our higher-level analysis we used the *Swift* software packages included in HEASOFT (v6.16) together with XIMAGE (v4.5.1), XSPEC (v12.8.2; Arnaud 1996), and XSELECT (v2.4c).

Before extracting light curves and spectra, we carefully inspected the level 2 event files for the *Swift* X-ray telescope (XRT; Burrows et al. 2005) and UVOT. We found that five observations were affected by the star trackers not being continuously "locked on" during some observations. Of those, ObsIDs 109, 122, and 178 corresponded to non-detections, and the intermittent tracking did not affect the derived upper limits. During ObsIDs 149 and 161 the source was detected, and the loss of tracking might have resulted in somewhat larger count rate uncertainties than those given in Table 13. Both ObsIDs were excluded from the X-ray variability analysis in

Section 5.7. In the case of the UVOT, ObsIDs 122, 149, and 178 showed strong indications of unstable pointing and were excluded from the UVOT analysis and light curve. In other UVOT images the point-spread functions (PSFs) were slightly elongated but still acceptable for photometry.

Furthermore, we inspected the XRT exposure maps for bad columns and bad pixels. As a result, we excluded a small number of ObsIDs from the X-ray variability analysis because those observations had bad detector columns going through the source count extraction region. The excluded ObsIDs were 128, 137, 140, 151, and 160. All of the excluded observations except 151, which has the most severe bad column issue, are included in the overall X-ray light curve described in Section 5.

All XRT data were obtained in photon counting (PC) mode. We applied the standard charge distribution grade selection (0–12) for XRT/PC data. The XRT count rates and upper limits presented here were extracted using the ximage sosta tool, which applies corrections for vignetting, dead-time, and PSF losses. The PSF model used is the same as that for the 2014 observations (see HND15) and was based on all merged XRT detections of the 2014 eruption. We visually inspected all XRT images and confirmed that the detections were realistic.

Table 2
Log of Spectroscopic Observations of the 2015 Eruption of M31N 2008-12a

Date (2015 UT)	Δt^a (days)	Telescope	Exp. Time (s)
Aug 28.95	0.67 ± 0.02	LT	3×900
Aug 29.24	0.96 ± 0.02	LT	3×900
Aug 29.38	1.10 ± 0.01	KPNO 4 m	1200
Aug 29.42	1.14 ± 0.02	LCOGT 2 m	3600
Aug 30.07	1.79 ± 0.11	LT	6×900^b
Aug 30.41	2.03 ± 0.02	LCOGT 2 m	3600
Aug 31.12	2.84 ± 0.11	LT	6×900^b
Sep 01.12	3.84 ± 0.02	LT	$3 \times 1,200$
Sep 02.19	4.91 ± 0.02	LT	$3 \times 1,200$

Notes.
[a] The quoted uncertainty on Δt relates to the total elapsed time during each observation.
[b] Two epochs of spectroscopy (both with 3×900 s exposure time) were collected by the LT on each of the nights of 2015 August 30 and 31; these were combined into single "nightly" spectra to improve the overall signal-to-noise ratio.

The X-ray spectra were extracted with the XSELECT software (v2.4c) and fitted for energies above 0.3 keV using XSPEC (v12.8.2; Arnaud 1996). Our XSPEC models assumed the ISM abundances from Wilms et al. (2000), the Tübingen–Boulder ISM absorption model (TBabs in XSPEC), and the photoelectric absorption cross-sections from Balucinska-Church & McCammon (1992). The spectra were binned to include at least one count per bin and fitted in XSPEC assuming Poisson statistics according to Cash (1979). We describe the fitting of blackbody models, some of which include additional emission or absorption features, in Section 6.4.

For the UVOT data, we examined all the individual sky images by eye. We found that ObsIDs 126 and 180 had no aspect correction, and we manually adjusted the source and background regions for consistent UVOT photometry.

We optimized the uvotsource source and background extraction regions, with respect to the 2013/14 analysis, based on a stacked image of all 2015 observations. The new source region has a 3″.6 radius, and uvotsource was operated with a curve-of-growth aperture correction. The background is derived from a number of smaller regions in the vicinity of the source that show a background luminosity similar to that of the source region in the deep image. All magnitudes assume the UVOT photometric system (Poole et al. 2008) and have not been corrected for extinction.

Statistical analysis was performed using the R software environment (R Development Core Team 2011). All uncertainties correspond to 1σ confidence, and all upper limits to 3σ confidence, unless otherwise noted.

4.4. Time of Eruption

For all observations of the 2015 eruption of M31N 2008-12a, we use the reference date ($\Delta t = 0$) defined as 2015 August 28.28 UT (MJD = 57262.28) as the epoch of the eruption. This date is defined as the midpoint between the last non-detection by the LT visible monitoring (2015 August 28.16 UT) and the first detection of the eruption by *Swift* UVOT (August 28.41), with an uncertainty of 0.12 day. We draw direct comparison to data from the 2014 and 2013 eruptions by assuming reference dates of 2014 October 2.69
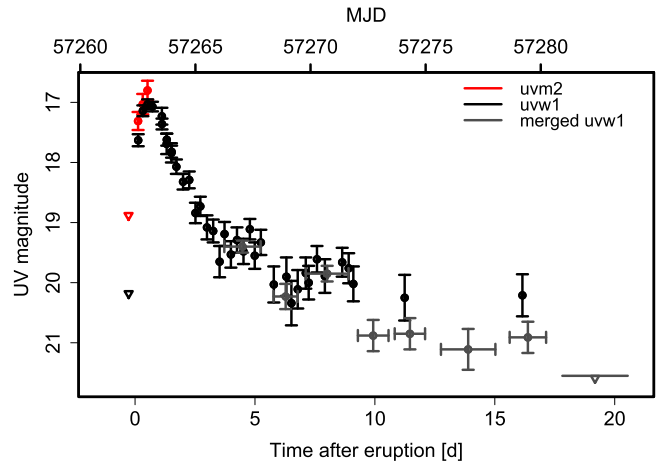

Figure 3. Unprecedentedly detailed *Swift* UVOT light curve for the 2015 eruption of M31N 2008-12a, showing for the first time the rising phase, the rapid smooth decline, and various plateaus. The black data points are the individual uvw1 snapshots. The gray points are based on stacked images (see Table 3). For clarity, no individual uvw1 upper limits after day zero are shown (see Table 13 for those). The red data points show a few initial uvm2 snapshots. Open triangles indicate 3σ upper limits. Uncertainties are combined 1σ statistical and systematic. Day zero is defined as MJD = 57262.28 ± 0.12 (see Section 4.4).

UT (MJD = 56932.69) and 2013 November 26.95 UT (MJD = 56622.95)[50], respectively.

5. PANCHROMATIC ERUPTION LIGHT CURVE (SOFT X-RAY TO NIR)

The NIR/visible light curve of the 2015 eruption, obtained via an array of ground-based telescopes, matched the high cadence achieved in 2014. However, the 2015 data surpass those from previous eruptions by virtue of their broader wavelength coverage (H–u'-band) and depth—extending the light curve from ~9 days (2014) to just under 20 days and following the decline through almost 6 mag (u'-band). The 2015 light curve data alone are the most extensive visible data compiled for a nova beyond the Milky Way and Magellanic Clouds. When combined with data from past eruptions, the light curve data are now comparable in detail to those on many Galactic novae.

The multi-color, high-cadence light curves of the eruption of M31N 2008-12a are presented in Figure 1. Here the black data points are the new 2015 data, the red points the 2014 data, and the blue points the 2013 data, all plotted relative to their respective eruption times (see Table 1). It is clear from inspecting these plots that the agreement between the light curves of the last three eruptions is indeed remarkable.

The unprecedentedly detailed and complete UV light curve of the 2015 eruption of M31N 2008-12a is the focus of Figure 3 (the combined 2014/2015 UV light curve is shown in Figure 1). The corresponding magnitudes are given in Table 13. For the first time, we observed the rise of the UV flux to the maximum and can put very tight constraints on the time of the UV peak. We followed the UV light curve for almost 20 days with a high cadence, until the UV flux finally dropped below our sensitivity limit. The result is by far the best UV light curve recorded for M31N 2008-12a and indeed for any M 31 nova.

---

[50] The epoch of the 2013 eruption has been updated from November 26.60 UT in HND14 by the fitting of the linear early decline (see Section 5) of the light curve to the 2014 and 2015 data.
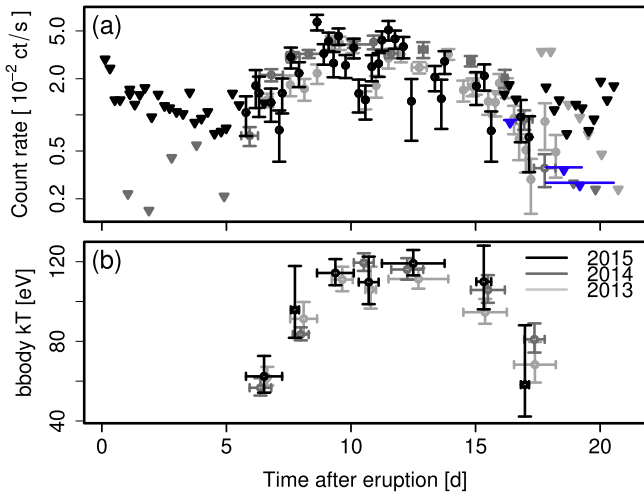
Figure 4. *Swift* XRT (a) count rate light curve (0.2–10 keV) and (b) effective blackbody temperature evolution of M31N 2008-12a during the 2015 eruption (black). In light/dark gray we show the corresponding data of the 2013/14 eruption. The time is in days after 2015 August 28.28 UT for the 2015 data. Panel (a): Triangles indicate upper limits. The blue points are merged detections and upper limits. Panel (b): Sets of observations with similar spectra have been fitted simultaneously, assuming a fixed $N_H = 1.4 \times 10^{21}$ cm^{-2}. The error bars in time represent either (a) the duration of the observation or (b) the time covering the sets of observations. The three eruptions show very similar timescales and luminosity/temperature evolution.

Figure 5. Evolution of the time of maximum light with wavelength. These data are consistent with the time of the maximum increasing linearly with wavelength with a gradient of 0.61 ± 0.11 days μm^{-1} (indicated by the red line).

Our observations used the UVOT `uvw1` filter throughout, which has a central wavelength of 2600 Å (FWHM 693 Å) and the highest throughput of the three UV filters (Poole et al. 2008). On the rise to the maximum, these were accompanied by occasional `uvm2` filter measurements. Those magnitudes, for a shorter central wavelength of 2250 Å (FWHM 657 Å), appear slightly brighter than the quasi-simultaneous `uvw1` values.

In Figure 4 we show the 0.2–10.0 keV X-ray light curve of the 2015 eruption compared to the 2014/13 results. Also shown is the evolution of the effective temperature based on a simple blackbody parametrization with a constant $N_H = 1.4 \times 10^{21}$ cm^{-2}. A more detailed spectral analysis is the subject of Section 6.4. Overall, the count rate and temperature evolution are very similar between the three eruptions. The X-ray count rate was initially very variable as the effective temperature rose to the maximum. After around day 13, we observed a decrease in the variability amplitude (see discussion below), although our observations became sparser in the second part of the SSS phase.

For further X-ray variability and spectral analysis, we assume that the last three eruptions evolved sufficiently similarly to warrant a combined treatment. Figure 4 indicates that this assumption is justified. The combined data provide improved statistics and signal-to-noise ratio to further explore the initial result presented by HND15 and investigate features such as the "dip" in the X-ray light curve around day eleven.

The far blue (u'-band) to NIR light curves and the early UV evolution can be separated into four distinct phases on the basis of their rate of change of flux: the final rise, from $t = 0$ to $t \simeq 1$ day; the initial decline, $1 \lesssim t \lesssim 4$ day; the "plateau" and SSS onset, $4 \lesssim t \lesssim 8$ day; and the SSS peak and decline, $8 \lesssim t \lesssim 19$ day (when the SSS is still detected). Here we define and discuss each of these four phases in turn.

5.1. The Final Rise (Day 0–1)

Like the 2014 eruption, the 2015 eruption was discovered before the peak in the visible light curves, and for the first time,
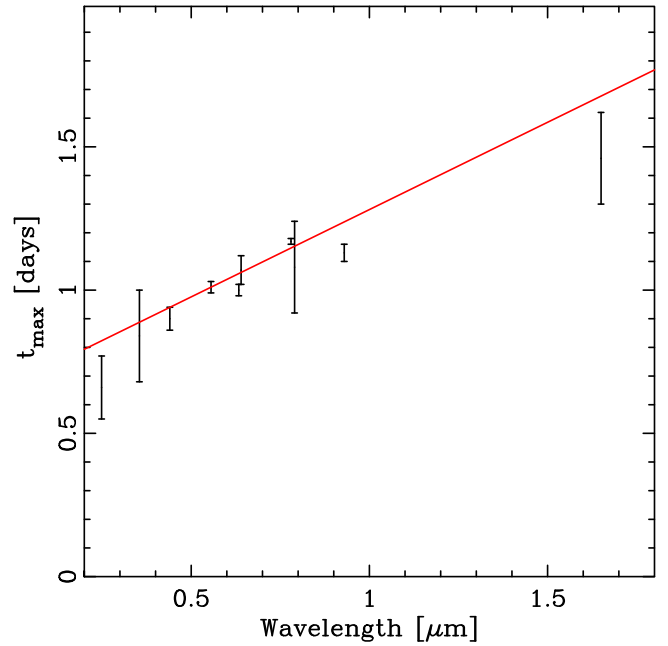
detailed pre-visible peak data have been compiled, particularly in the r' and i' bands. However, other than single-filter initial detections, there are still limited data before the final magnitude of the rise to the peak—a regime which must be a target for future eruptions. These eruptions appear to be characterized by a relatively slow rise to maximum light, compared to CNe of similar speed class (see Hounsell et al. 2010, 2016, and below), with the final magnitude of the rise taking around 1 day.

Based on data from the 2013–2015 eruptions, the time of the maximum in each filter (t_{max}) was estimated by fitting a quadratic function to the data around the peak ($0 \leqslant t \leqslant 2$ day). In all cases the peak data were well fit by this simple model. The resulting t_{max} estimates are reported in Table 4 and are shown in Figure 5. Here, any systematic uncertainties arising from the estimation of the eruption time for the separate years are ignored. As expected, the uncertainties on the values of t_{max} are dominated by the sampling around the peak of the light curves. The time of the maximum shows a strong trend of increasing with wavelength, consistently increasing linearly with wavelength with a gradient of 0.61 ± 0.11 days μm^{-1} (within the range $0.25 \lesssim \lambda \lesssim 1.6$ μm; $\chi^2_{/dof} = 3.4$).

The UV flux rose quickly from a >20.5 mag upper limit (`uvw1`) on day -0.27 to a 17.7 ± 0.1 mag detection on day 0.13 (see Table 13). The maximum of 17.13 ± 0.08 mag and 17.17 ± 0.09 mag was reached on days 0.52 and 0.73, respectively. The preceding observation on day 0.32 had shown 17.3 ± 0.01 mag. In the next observation, on day 1.12, the nova had declined to 17.3 ± 0.1 mag.

5.2. Initial Decline (Day 1–4)

In all filters (`uvw1`–H), the combined three-eruption light curves between t_{max} and 4 days post-eruption are well fit by a linear decline (an exponential decline in luminosity; see the diagonal gray lines in Figure 1; also noted by TBW14 and DHS15). We use this simple model to determine the t_2 decline

times for each filter (see Table 4). The derived t_2 values are consistent with those determined based on the 2014 data alone (DHS15) but are better constrained. With the light curve decaying fastest in the B- and V-bands ($t_2 \lesssim 2$ day), this method also allowed the determination of t_3 (in both cases $t_3 \lesssim 3$ day). For the remaining filters, t_3 was determined by linear interpolation between the light curve points bracketing $\Delta m = 3$ mag from the peak, where the data were available. The redder filters suffer more severely from the crowding of nearby bright sources in M 31 (typically red giants; see DWB14); therefore, it was not possible to follow the z'-band light curve down to t_3, and the H-band light curve could only be followed for around 1 mag from the peak (here, t_2 is extrapolated but poorly constrained, under the assumption that the linear behavior seen in other bands would be replicated).

To date, at least 14 Galactic novae (including three confirmed and one suspected RN) have been observed with a decline time $t_2 \lesssim 4$ days (see Hounsell et al. 2010; Strope et al. 2010; Munari et al. 2011; Orio et al. 2015), and these are summarized in Table 5. M31N 2008-12a resides at the faster end of this rapidly declining sample, exhibiting decline times very similar to those of the RN U Sco (marginally slower to t_2 but faster to t_3, assuming V-band luminosities), and exhibits the only known decline with $t_3 < 3$ days. The decline time of a nova is fundamentally linked to the WD mass and the accretion rate, with the shortest decline times corresponding to the combination of a high-mass WD and a high accretion rate (see, for example, Yaron et al. 2005, their Figure 2(d)). From the extremely short t_3 of M31N 2008-12a, we can infer that the WD in this system must be among the most massive yet observed.

5.3. The "Plateau" and SSS Onset (Day 4–8)

Strope et al. (2010) define a nova light curve plateau as an approximately flat interval occurring within an otherwise smooth decline. Those authors also point out that observed plateaus often include some scatter and that the light curve may still decline slightly during such times.

Following the linear decline from the peak to $t \simeq 4$ days, the visible light curves appear to enter such a plateau phase lasting until at least day 8. This plateau phase is observed in the u'-band through the i'-band, but the nova is already too faint to be detected above the crowded unresolved stellar background of M 31 in the z'- and H'-band observations (see above). The plateau phase in the combined light curves shows a small decrease in brightness over this period. The plateau occurs around 2.5–3 mag below the peak and, in the combined light curves, displays apparent variability with an amplitude of up to 1 mag.

Following the 2014 eruption, DHS15 also noted the plateau phase, but the more limited data led them to conclude that the light curve was essentially flat during this stage. Hence the "upturn" in brightness at the end of the plateau noted by DHS15 is likely to be related to the variability of this stage seen in the combined data. The onset of the quasi-plateau occurs around 1–2 days before the SSS is unveiled and may be related to (see, for example, Hachisu et al. 2008).

The UV light curve also shows similar behavior around this time, although these data have larger associated uncertainties (see Figure 1). However, an alternative interpretation could include a series of two shorter-lived UV plateaus (see in particular the gray combined points in Figure 3): The first
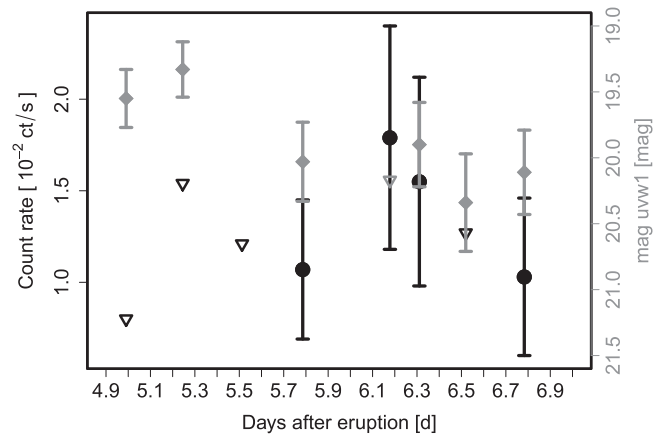

Figure 6. *Swift* XRT count rates (black circles) and UVOT uvw1 magnitudes (gray diamonds) used for estimating the SSS turn-on time as day 5.6 ± 0.7 after eruption (cf. Figures 3 and 4; XRT/UVOT upper limits are shown as open triangles in black/gray).

plateau, at 19.5 ± 0.1 mag, was centered around day 4.5, lasting about 1.5 days. The end of this plateau, at around day 5.5, roughly coincided with the appearance of the SSS in X-rays (cf. Figure 4). The UV magnitude then dropped to a second plateau at around 20.4 ± 0.3 mag for about 1.5 days around day 6.5 but soon showed indications for another slight rebrightening to 19.9 ± 0.1 mag. This phase lasted for another 1.3 day until around day 9.0.

The X-ray and UV light curves around the time of the SSS turn-on are shown in Figure 6. As the SSS flux gradually emerged, the UV magnitude was seen to drop from the first plateau seen in Figure 3. Based on the last deep XRT upper limit on day 5.0 (ObsID 120) and the second detection on day 6.2 (ObsID 124), with a count rate significantly above this upper limit, we estimate the SSS turn-on time as $t_{on} = 5.6 \pm 0.7$ days (cf. Table 13). This supersedes the initial estimate by Henze et al. (2015c) and includes the uncertainty of the eruption date.

This uncertainty range is a conservative estimate. By day 5.8 (ObsID 123), a clear concentration of source counts can already be seen at the nova position. Note that ObsID 122 (day 5.5) had severe star tracking issues that would have affected the XRT PSF (see Section 4.3). However, the XRT event file showed no indication of an increase in counts within a generous radius of the source position. Therefore, it is unlikely that the SSS was already visible before day 5.8.

We emphasize that the early SSS flux of M31N 2008-12a is highly variable, which limits the precision of turn-on time estimates. Nevertheless, the observed turn-on timescale is consistent with the 2013 (6 ± 1 days) and 2014 (5.9 ± 0.5 days) eruptions (see HND14, HND15).

5.4. The "SSS Peak and Decline" (>8 day)

Once the plateau phase ended on day ~8, the far blue-NIR light curve entered a second phase of apparent linear decline in magnitude (an exponential decline in flux). With the nova again fading rapidly, the system only remained visible through the i'-, r'-, and V-band filters for a few more days. However, this near-linear decline was followed until day ~17 in the B-band and day ~20 in the u'-band (just beyond the SSS turn-off). The decay rate of this decline phase of the light curve was steeper than that of the quasi-plateau phase but much shallower than

Table 3
Stacked *Swift* UVOT Images and Magnitudes

ObsIDs[a]	Exp[b] (ks)	Date[c] (UT)	MJD[c] (d)	Δt[c] (d)	Duration[d] (d)	uvw1 (mag)
00032613115/121	6.3	2015 Sep 01.76	57266.76	4.48	1.52	19.5 ± 0.1
00032613123/127	4.4	2015 Sep 03.56	57268.56	6.28	1.00	20.3 ± 0.2
00032613128/135	6.1	2015 Sep 05.29	57270.29	8.01	1.79	19.9 ± 0.1
00032613137/142	6.2	2015 Sep 07.21	57272.21	9.93	1.28	21.0 ± 0.3
00032613142/148	6.4	2015 Sep 08.61	57273.61	11.33	1.52	20.6 ± 0.3
00032613151/160	4.4	2015 Sep 11.17	57276.17	13.89	2.27	21.2 ± 0.3
00032613162/168	5.5	2015 Sep 13.66	57278.66	16.38	1.52	21.0 ± 0.3
00032613171/182	9.5	2015 Sep 16.46	57281.46	19.18	2.73	<21.6

Notes.
[a] First and last observations of the stack (cf. Table 13).
[b] Combined exposure time.
[c] Midpoint of the stack with Δt referring to the eruption date on 2015 August 28.28 UT (MJD 57262.28; see Section 4.4).
[d] Time between the first and last observations of the stack.

that of the early decline. The mean decline rate in the u'-, B-, and V-bands during this phase was 0.2 mag day^{-1} (five times as slow as the mean early decline in the same bands).

The end of the SSS phase was first reported by Henze et al. (2015b). Based on the overall X-ray light curve in Figure 4, we estimated the SSS turn-off time as $t_{\rm off} = 18.6 \pm 0.7$ days after eruption. This is a conservative estimate that takes into account the last X-ray detection on day 17.1 (ObsID 168) and the midpoint of the merged deep upper limit on day 19.2. The uncertainty includes the eruption date range. Within the errors, the estimate is consistent with the 2013 (19 ± 1) and 2014 (18.4 ± 0.5) eruptions as well as the 2012 X-ray non-detection on day 20 (see HND14).

However, in the UV, the decline after day 9 reached ~ 21 mag where the source remained, with typical uncertainties of 0.3 mag, until about day 17–18. All average magnitudes are based on sets of stacked UVOT images, which are summarized in Table 3 and shown in Figure 3.

The extent of the UV light curve is consistent with the duration of the SSS phase. After day 10, there were only two detections in individual images: around the time of the possible X-ray dip around day 11 and during the SSS decline around day 16 (cf. Figure 4 and Table 13). After the SSS turn-off, the UV flux dropped sharply, and nothing was detected in 10 merged observations (9.5 ks covering 2.7 days) around day 19.2 with a 3σ upper limit of 21.7 mag.

We were able to follow the light curve in the u'-band until ~ 1 mag above quiescence (as determined from *HST* photometry; DWB14; TBW14; M. J. Darnley et al. 2017, in preparation). Utilizing the pre-existing *HST* quiescent photometry of this system (see DWB14 and TBW14), we can estimate that, assuming a continuation of this linear decline, the time to return to quiescent luminosity would be only 25–30 days post-eruption. This, of course, assumes that there is no dip below quiescence as seen in, for example, RS Oph as the accretion disk in that system reestablishes post-eruption (Worters et al. 2007; Darnley et al. 2008).

It is worth noting that this decline phase can also be fit with a power-law decline in flux (providing a marginally better fit than a linear decline). The index of the best-fit power law ($f \propto t^\alpha$) to the u'-band data is $\alpha = -1.8 \pm 0.2$. This is inconsistent with the late-time decline predicted by the universal nova decline law of Hachisu & Kato (2006, 2007, $\alpha = -3.5$) but is consistent with the "middle" part of their decline law

($\alpha = -1.75$). Based on such a power law decline in this phase, we would predict a timescale of 30–35 days to return to quiescent luminosity.

5.5. Light Curve Color Evolution

In Figure 2 we present the dereddened color evolution of the 2013–2015 eruptions of M31N 2008-12a (blue, red, and black points, respectively). With the exception of the UV data, here, color data are only provided where there are near-simultaneous multi-color observations available from the same facility. We also note that the $(u' - B)_0$ and $(V - r')_0$ plots contain a mix of photometric systems (Vega and AB); no attempt was made to correct between the photometric systems due to the non-blackbody nature of the M31N 2008-12a spectra. In order to provide better temporal matches with the ground-based 2015 data, the UV data from all eruptions are combined here.

Ground-based u'- and z'-band data were only collected during the 2015 eruption. Therefore, the coverage in the $(u' - B)_0$ and $(i' - z')_0$ colors is less complete; the $(i' - z')_0$ plot is also compounded by crowding. The color plots all cover the final rise of the eruption (from $t \simeq 0$ until $t \simeq 1$ day). The $(u' - B)_0$, $(B - V)_0$, $(V - r')_0$, and $(r' - i')_0$ plots all indicate that the emission from the system is becoming redder during this phase—as might be expected if the pseudo-photosphere was still expanding at this stage (however, the spectral energy distribution [SED] snapshots during the final rise do not show evidence of a change in slope; see Section 7.2). However, as will be discussed in Sections 6 and 7.2, even at these early times line emission in the visible spectra is already important, and this may significantly affect the color behavior.

From $t \simeq 1$ to $t \simeq 4$ day, during the linear early-decline phase, the $(B - V)_0$ and $(V - r')_0$ plots exhibit a linear evolution in the color, although, interestingly, in $(B - V)_0$ the emission becomes significantly bluer, whereas the opposite is true for $(V - r')_0$. The $(V - r')_0$ evolution is almost certainly affected by the change in the Hα line profile and flux (see again Section 6). The $(u' - B)_0$ data, albeit sparser, initially become bluer but appear to stabilize around day 3, whereas $(r' - i')_0$ continues to redden until day 2 and then becomes systematically bluer. In general, the very uniform panchromatic linear early decline seen from the NIR to the NUV in this phase is not replicated in the color data, probably due to the additional complications of line emission.

The color behavior during the plateau phase ($4 \lesssim t \lesssim 8$ days) is again varied. The $(u' - B)_0$ color remains approximately constant, although there is some variability. Again $(B - V)_0$ and $(V - r')_0$ colors have opposing behavior, with the former becoming redder and the latter bluer. This behavior may again be related to line emission, but with no spectra beyond day 5 (see Section 6) we can only speculate; the trends seen in these colors may be due to diminishing Balmer emission with increased nebular line emission (e.g., [O III] $4959/5007$ Å). Let us compare this to the behavior observed from the 2006 eruption of RS Oph. Iijima (2009) reported that between days 50 and 71 a broad component of the [O III] lines began to grow, peaking in intensity around day 90; a similar analysis was reported by Tarasova (2009). These timescales are roughly consistent with that of the SSS evolution reported by Osborne et al. (2011; also see references therein), with the SSS roughly constant in luminosity between days 45 and 60. We also note that somewhat of a plateau phase is observed between days 50 and 76 (in B- and V-band data; Schaefer 2010). The effective consistency of these three timescales in RS Oph supports our prediction of nebular emission driving the color evolution during the plateau phase in M31N 2008-12a.

As the color plots enter SSS decline at $t \gtrsim 8$ days, where there are data on $(uvw1 - u')_0$, $(u' - B)_0$, and $(B - V)_0$, the color of the system remains approximately constant during the later part of the SSS phase. However, the $(uvw1 - u')_0$ and $(u' - B)_0$ color plots show a marked shift to blue as the SSS begins to turn-off.

5.6. Color–Magnitude Evolution

Color–magnitude diagrams of RNe are useful for distinguishing the evolutionary stage of the companion star. Hachisu & Kato (2016) demonstrated a clear difference between the color–magnitude tracks of eruptions from systems hosting a red giant companion (RG-nova) and those having a sub-giant or main-sequence companion (SG- or MS-nova). The color–magnitude track evolves almost vertically along the line of $(B - V)_0 = -0.03$ (the intrinsic color of optically thick free–free emission; as shown in Figure 7, along with $(B - V)_0 = 0.13$ for optically thin free–free emission; also see the discussion in Section 7.2) for RNe harboring a red giant companion, such as V745 Sco (2014 eruption, data from Page et al. 2015; also see Section 7.6) and RS Oph (1958, 1985, and 2006 eruptions; data from Connelley & Sandage 1958; Sostero & Guido 2006a, 2006b; Sostero et al. 2006; Hachisu et al. 2008, AAVSO[51], VSOLJ[52], and SMARTS[53]; see Hachisu & Kato 2016 for full details)—see Figures 7(a) and (b), respectively. On the other hand, the track goes blueward and then turns back redward near the two-headed arrow, as shown in Figure 7(c), for RNe with a sub-giant or main-sequence companion—for example, U Sco, CI Aquilae, and T Pyxidis (data from Pagnotta et al. 2015, VSOLJ, and AAVSO/SMARTS, respectively). The tracks of these three RNe are very similar to one another and clearly different from those for V745 Sco and RS Oph. Color–magnitude diagrams are plotted for only five Galactic RNe due to the general lack of

panchromatic (X-ray/UV/visible) eruption data for Galactic RNe (see discussion in Hachisu & Kato 2016).

If we adopt the newly constrained extinction of $E_{B-V} = 0.10$ (M. J. Darnley et al. 2017, in preparation) and therefore the *apparent* distance modulus $\mu_V = 24.75$ (Freedman & Madore 1990), the track of M31N 2008-12a appears closer to those of V745 Sco and RS Oph than to those of U Sco, CI Aql, and T Pyx, as shown in Figures 7(a)–(c). This is consistent with the interpretation, drawn in this paper from the eruption spectroscopy, that the companion in M31N 2008-12a is a red giant.

However, it should be noted that the position of the color–magnitude track depends strongly on the assumed extinction (and distance). If we increase the value of the extinction—for example, to $E_{B-V} = 0.30$ (as originally proposed in DHS15; see Figure 7(d))—the track moves closer to those of U Sco, CI Aql, and T Pyx.

The conclusion reached here differs from the conclusion drawn by Kato et al. (2016), who favored (based partly on the M31N 2008-12a color–magnitude diagram published by Hachisu & Kato 2016) that the companion is a sub-giant. This earlier analysis used the less detailed data available at the time but also had no strong constraint on the extinction. It should be noted that the color–magnitude analysis presented in this paper supersedes the same analysis for M31N 2008-12a presented by Hachisu & Kato (2016).

5.7. The X-Ray Variability

The SSS phase variability is examined in detail in Figure 8. There, we show the 2013–2015 XRT count rates based on the individual XRT snapshots. In the case of the 2015 data, there is no difference between the count rates binned by ObsID (see Figure 4) because all detections during the SSS phase only consisted of single snapshots.

Early high-amplitude variability is particularly clearly visible in Figure 8(b). During the 2015 campaign, we collected only a few observations during the late SSS phase. However, the combined light curve of the last three eruptions suggests a relatively sudden drop in variability after day 13.

As in HND15, we identified snapshots with count rates significantly above or below the (smoothed) average for the time around the SSS maximum. Those measurements are marked in Figure 8(b) in red (high rate) or blue (low rate). The combined XRT spectra of these data points for all three eruptions are shown in Figure 8(c) using the same color scheme. Those spectra are discussed in the context of spectral variability in Section 7.3 below. All three eruptions show a consistent factor of 2.6 in difference between high- and low-count-rate snapshots.

We note that in 2015 there appears to be less variability during the first two days of the SSS phase than in 2013 and 2014. This is reflected in a less significant statistical difference between the X-ray count rate before and after day 13. An F-test results in a p-value of 0.03, which, while still significant at the 95% confidence level, is considerably reduced with respect to the 2013 (2.1×10^{-6}) and 2014 (1.8×10^{-5}) results (see HND15).

In fact, the SSS variability in 2015 might be almost entirely explained by a dip in flux on day 10–11. To investigate this possibility, we plot the three XRT snapshot light curves separately in Figure 9(a). The smoothed fits now exclude a 1 day window centered on day 10.75, during which the 2015

---

[51] American Association of Variable Star Observers, https://www.aavso.org.
[52] Variable Star Observers League in Japan, http://vsolj.cetus-net.org/.
[53] The Stony Brook/SMARTS Spectral Atlas of Southern Novae, http://www.astro.sunysb.edu/fwalter/SMARTS/NovaAtlas; see Walter et al. (2012).
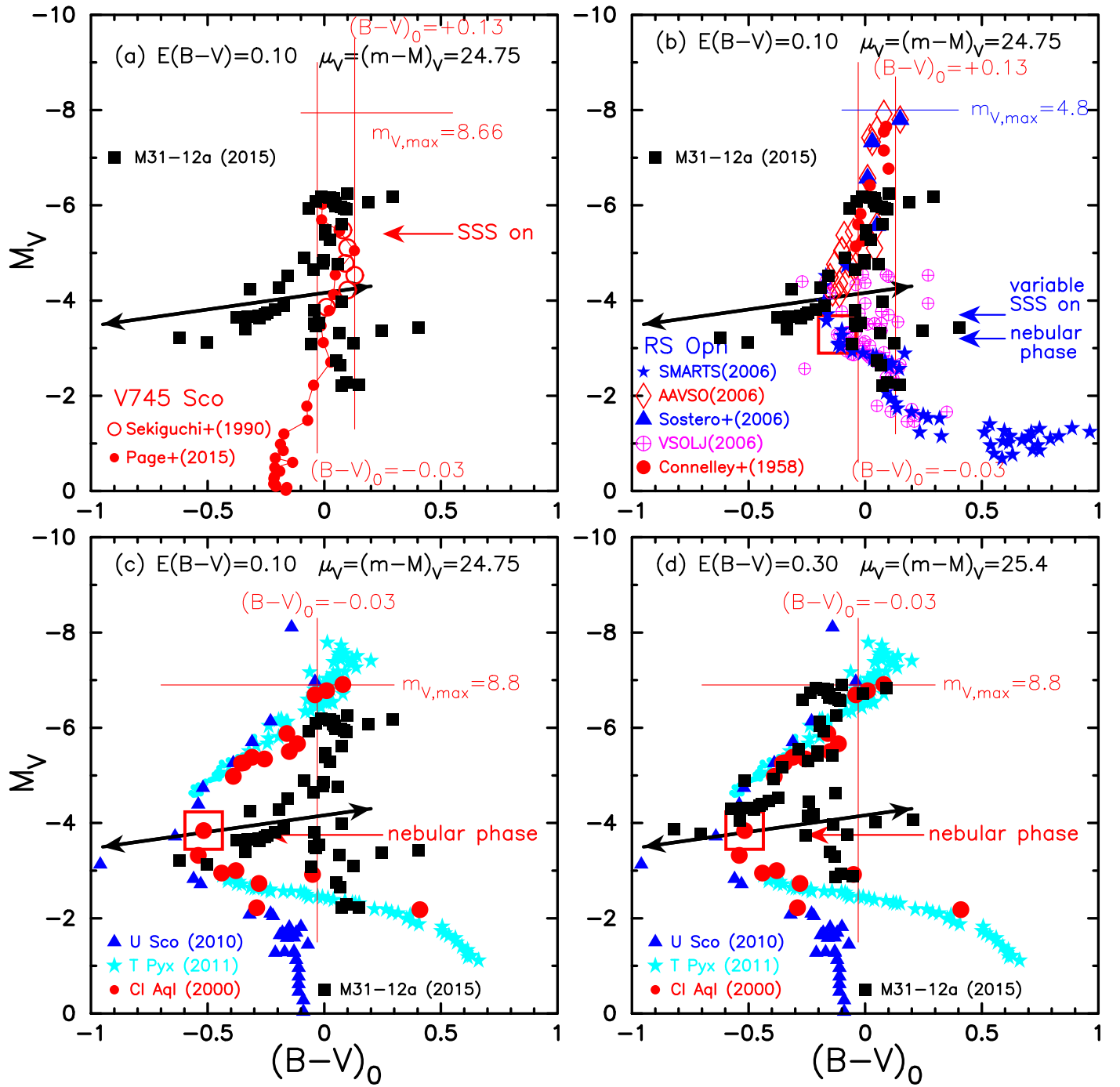
Figure 7. Color–magnitude diagrams of M31N 2008-12a for various extinctions and *apparent* distance moduli (indicated at the top of each plot) are compared with those of Galactic RNe. Throughout, the filled black squares denote the color–magnitude points of M31N 2008-12a from the 2013, 2014, and 2015 eruptions. In each plot the evolution of M31N 2008-12a is compared directly to those of (a) V745 Sco (RG-nova), (b) RS Oph (RG-nova), and (c)–(d) U Sco and CI Aql (SG-novae) and T Pyx (MS-nova); see the plot keys and text for further details. The horizontal lines labeled "$m_{V,max}$" show the maximum brightnesses of (a) V745 Sco, (b) RS Oph, and (c)–(d) CI Aql. The vertical red lines show the intrinsic colors of optically thick ($(B - V)_0 = -0.03$) and optically thin ($(B - V)_0 = +0.13$) winds (see Hachisu & Kato 2014 for further details). In panel (a) the red arrow labeled "SSS on" indicates the optical luminosity at the SSS turn-on of V745 Sco. In panel (b) the blue arrows labeled "variable SSS on" and "nebular phase" indicate the onset of the variable SSS phase and nebular phase of RS Oph. In panels (c) and (d) the red arrows indicate where the nebular phase of CI Aql started. The two-headed black arrows indicate where the color–magnitude tracks of some novae show a turning from toward blue to toward red (see Hachisu & Kato 2016 for more details). In plot (d) the extinction toward M31N 2008-12a was allowed to vary for illustrative purposes. Given the known extinction, the track of M31N 2008-12a is closer to those of the RG-novae (a)–(b) than to those of the other RNe (c)–(d), consistent with the interpretation from the eruption spectra that the companion is a red giant.

dip occurred. Interestingly, there seems to be a similar feature in the 2013 light curve. For both years, the X-ray flux dropped by a factor of ∼2 during this window. In 2014 there is no clear dip during this time. However, there were only two snapshots within the 1 day window.

The 2014 X-ray light curve might instead show a dip between days eight and nine, during which time there were fewer observations in 2013 and 2015 (see Figure 9(a)). In any case, all light curves display additional variability besides the potential dip features. This can be seen in Figure 9(b), where
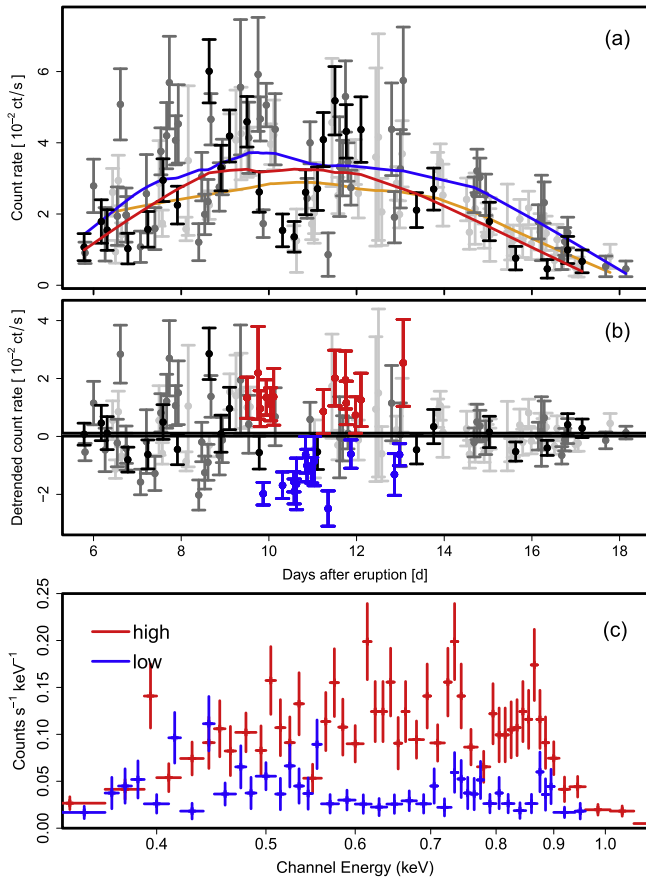
Figure 8. Panel (a): The short-term X-ray light curve of M31N 2008-12a based on the individual XRT snapshots. Data points with error bars show the XRT count rates and corresponding errors for the 2015 (black), 2014 (dark gray), and 2013 (light gray) eruptions. Note that the count rate axis uses a linear scale in contrast to the logarithmic scale in Figure 4. Solid lines represent smoothed fits, based on local regression, on the 2015 (red), 2014 (blue), and 2013 (orange) data. The three eruptions display very similar behavior. Panel (b): The light curves from panel (a) have been de-trended by subtracting the smoothed fits from the respective data. The red data points mark the count rates that are at least 1σ above the smoothed fit for the 2015 (2014/13) data during the temperature maximum. The blue data are at least 1σ below the average 2015 (2014/13) count rate for the same time range. The drop in variability amplitude around day 13 is clearly visible in all three eruptions. Panel (c): Binned XRT spectra for all the high- (red colors) and low-luminosity (blue colors) snapshots of the 2015/14/13 monitoring that are indicated in panel (b) with corresponding colors. There are indications that the spectra are different in more than the overall luminosity (see Section 7.3 and Table 14).

we subtracted the smoothed fits in Figure 9(a) to highlight the potential dip and residual variability.

If the potential dip as the main source of variability is removed, then the light curves of the 2013 and, in particular, the 2015 SSS phase appear to show significantly less residual variability (see Figure 9). However, the 2014 light curve does not seem to show the same behavior. Clearly, high-cadence coverage of several future observations is needed for a proper statistical treatment of this peculiar variability.

Interestingly, the *ROSAT* light curve of the 1993 detection in White et al. (1995) might also show a tentative, one-bin dip between day 9 and 10 (days 10 and 11 in the lower panel of their Figure 2). The *ROSAT* data of the preceding 1992 detection only extend to about day 8 after eruption but show significant variability over their coverage.
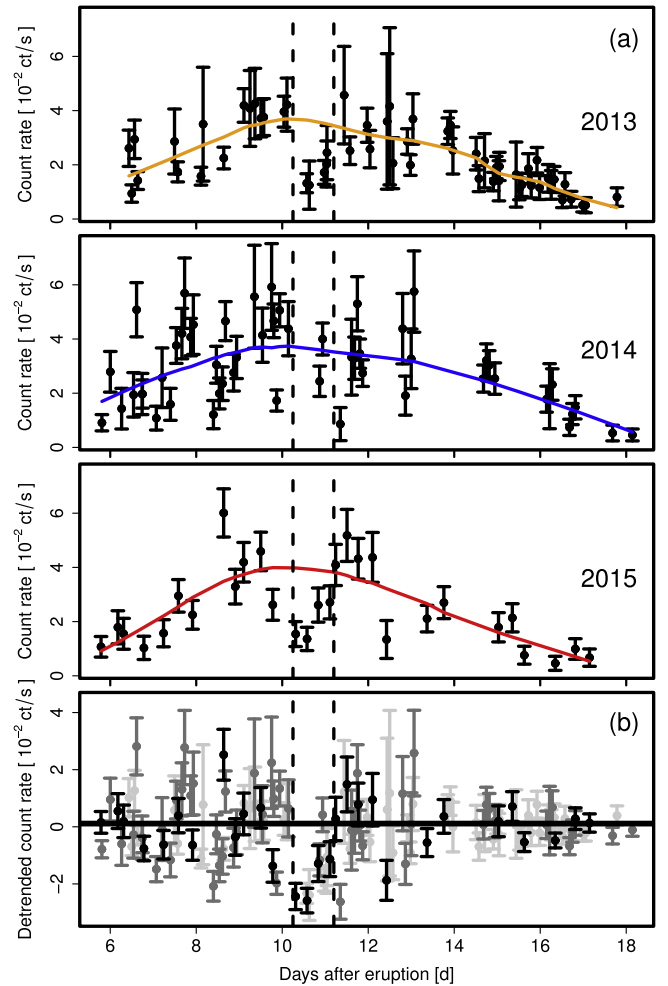

Figure 9. Same as Figure 8, but for the individual XRT snapshot light curves (panel (a)) and the combined de-trended light curves (panel (b)). Here, the smoothed fits (solid lines with the same colors as in Figure 8(a)) were determined excluding the data points within the time range indicated by the vertical dashed lines. Panel (b) shows the 2015 data, in black, overlaid on the 2013/2014 data, in light/dark gray. A possible dip on days 10–11 is clearly visible in 2013 and 2015, with 2014 having insufficient data to reject such a feature.

As in 2013 and 2014, there is no evidence for any periodicities during the SSS variability phase (Figure 8(b)), according to a Lomb–Scargle test (Lomb 1976; Scargle 1982). The apparently aperiodic variability is present on all accessible timescales (hours to several days), and the amplitude shows no significant relation with the frequency. We have been granted a 100 ks *XMM-Newton* (RGS) ToO observation to study the (spectral) variability of M31N 2008-12a with higher time resolution in a future eruption. However, because of the stringent (anti-)Sun constraints of the *XMM-Newton* observatory, there are only two possible observing windows in January–mid-February and July–mid-August, respectively. Given the remaining uncertainty in predicting future eruption dates (see Section 7.5), a successful *XMM-Newton* trigger might take several years.

Due to the very short duration of the SSS plateau phase and the XRT count rate of the source, our analysis was only sensitive to periods of a few hours to a few days (and sensitive to amplitudes larger than 1.5×10^{-2} ct s^{-1} on the 99% confidence level, following Scargle 1982). This time range includes typical orbital periods of Roche lobe-overflow RNe,

Table 4
Light Curve Parameters of the Eruption of M31N 2008-12a, Based on Combined Data from the 2013, 2014, and 2015 Eruptions

Filter	t_{max} (days)	m_{max} (mag)	t_2 (days)	t_3 (days)	Decline Rates (mag day^{-1})		
					Early Decline $t_{max} \leqslant t \leqslant 4$ day	"Plateau" $4 \leqslant t \leqslant 8$ day	Final Decline $t > 8$ day
$uvw1$	0.66 ± 0.11	17.34 ± 0.08	2.55 ± 0.16	$5.65^{+0.22}_{-0.40}$	0.78 ± 0.05	0.19 ± 0.05	0.08 ± 0.03
u'	0.84 ± 0.16	18.35 ± 0.03	2.60 ± 0.08	$5.74^{+1.02}_{-0.84}$	0.77 ± 0.03	0.11 ± 0.08	0.16 ± 0.02
B	0.90 ± 0.04	18.67 ± 0.02	2.02 ± 0.07	3.03 ± 0.10[a]	0.99 ± 0.03	0.14 ± 0.06	0.18 ± 0.02
V	1.01 ± 0.02	18.55 ± 0.01	1.65 ± 0.04	2.47 ± 0.06[a]	1.21 ± 0.03	0.09 ± 0.03	0.17 ± 0.05
R	1.07 ± 0.05	18.38 ± 0.02	2.24 ± 0.13	⋯	0.89 ± 0.05	⋯	⋯
r'	1.00 ± 0.02	18.45 ± 0.01	2.05 ± 0.04	$4.72^{+0.26}_{-0.15}$	0.97 ± 0.02	0.30 ± 0.05	⋯
i'	1.17 ± 0.01	18.60 ± 0.01	2.13 ± 0.05	$3.40^{+0.53}_{-0.31}$	0.94 ± 0.02	0.11 ± 0.06	⋯
I	1.08 ± 0.16	18.31 ± 0.03	2.54 ± 0.28	⋯	0.79 ± 0.09	⋯	⋯
z'	1.13 ± 0.03	18.73 ± 0.02	2.13 ± 0.09	⋯	0.94 ± 0.04	0.06 ± 0.04	⋯
H	1.46 ± 0.16	17.66 ± 0.13	3.75 ± 0.45[b]	⋯	0.53 ± 0.06	⋯	⋯

Notes.
[a] A linear fit to the data over the interval $t_{max} \leqslant \Delta t \leqslant 4$ days includes a decline of $\geqslant 3$ mag.
[b] H-band t_2 is determined by extrapolation of a linear fit to the data as less than two magnitudes of decline was recorded.

e.g., U Sco, with ∼1.2 day (Ness et al. 2012), and Nova LMC 2009a, also with ∼1.2 day (Bode et al. 2016). The spin periods of high-mass WDs in CVs without strong magnetic fields (i.e., not polars) are typically shorter (several 100–1000 s; see, for example, Norton et al. 2004). For instance, a period of ∼1110 s was reported for the suspected intermediate polar (and suggested RN; see Bode et al. 2009) M31N 2007-12b (Pietsch et al. 2011). Polars, like the old nova V1500 Cyg (see, for example, Litvinchova et al. 2011), have generally longer spin cycles of several hours due to a magnetic synchronization of the orbital and spin periods that slow down the WD rotation (see, for example, Norton et al. 2004). Even shorter transient periods <100 s have been found in the RNe RS Oph (35 s) and LMC 2009a (33 s) as well as in a few other CNe and the canonical SSS Cal 83 by Ness et al. (2015), who discuss pulsation mechanisms as the possible origin.

6. PANCHROMATIC ERUPTION SPECTROSCOPY

The earliest spectroscopic observations of M31N 2008-12a prior to the 2015 eruption were obtained by the William Herschel Telescope (WHT) 1.27 days after the 2014 eruption (DHS15). Following the 2015 eruption, the first three visible spectra were obtained at 0.67 days, 0.96 days, and 1.10 days post-eruption. For a nova with a V-band decline time as fast as $t_2 = 1.65$ days (see Table 4), the early 2015 spectra capture significantly earlier portions of the eruption than had been seen previously. Additionally, with the peak V-band luminosity occurring 1.01 days after eruption (see Table 4), the first two 2015 spectra were taken while the nova light curve was still rising in the visible, but notably 0.01 days and 0.3 days *after* the UV light curve peak. The final 2015 spectrum captures the eruption 0.3 days later than any previous spectra. All of the flux-calibrated spectra of the 2015 eruption are shown in the top portion of Figure 10.

An initial summary following the first spectrum of the 2015 eruption of M31N 2008-12a was reported in Darnley et al. (2015d). As in 2012 (Shafter et al. 2012), 2013 (TBW14), and 2014 (DHS15), the individual spectra are dominated by hydrogen Balmer series emission lines (Hα through Hδ) in 2015. Emission lines from He I (4471, 5015, 5876, 6678, and 7065 Å), He II (4686 Å), N II (5679 Å), and N III (4640 Å) are

also clearly visible but appear to fade significantly in the later spectra. There is a clear detection of continuum emission in each of the spectra. Despite collecting spectra from much earlier in the eruption process, we see no clear absorption components (i.e., P Cygni profiles) in any of the spectra, which point to low-mass ejecta. No Fe II or O I lines, characteristic of "Fe II novae," or any Ne lines are detected in the individual spectra. As in previous eruptions, the observed spectral lines and velocities (see Sections 6.2 and 6.3) are consistent with the eruption of a nova belonging to the He/N taxonomic class (Williams 1992, 2012; Williams et al. 1994).

6.1. Multi-eruption Combined Visible Spectrum

In the bottom plot of Figure 10 we present a combined spectrum using data from the 2012 (HET), 2014 (LT and WHT), and 2015 (LT, LCOGT, and KPNO) eruptions. Here we have re-sampled all spectra to the wavelength scale of the LT SPRAT data (linear 6.4 Å pixel^{-1}), re-scaled them, and median-combined the data. We have excluded the final epoch data from 2014 and 2015 as the signal-to-noise ratios of these spectra were particularly low. As such, this combined spectrum covers the period from 0.67 to 3.84 days post-eruption. When accounting for the relevant exposure time and telescope collecting area, this combined spectrum would be the equivalent of a single 48 ks spectrum as taken by the LT with SPRAT—by far the deepest spectrum of an M31 nova yet obtained. The combined spectrum is, as expected, very similar to the individual spectra, but a number of fainter features increase in significance. For example, we note that the He I (5015 Å) line identified in the individual spectra is likely to be a blend of the He I 5015 and 5048 Å lines. In the combined spectrum, there is still no convincing evidence for the presence of Fe II, O I, or Ne lines.

Newly visible lines at ∼4200 and ∼4542 Å are roughly coincident with the H-like He II Pickering series (Pickering & Fleming 1896, transitions to the $n = 4$ state). Many stronger Pickering lines are blended with the Balmer series, but the apparent lack of the He II (5412 Å) line makes these identifications unlikely. The line at ∼4200 may therefore be C III (4187 Å). The second line remains unidentified, and we believe it is unlikely to be Fe II (4549 Å) due to the lack of
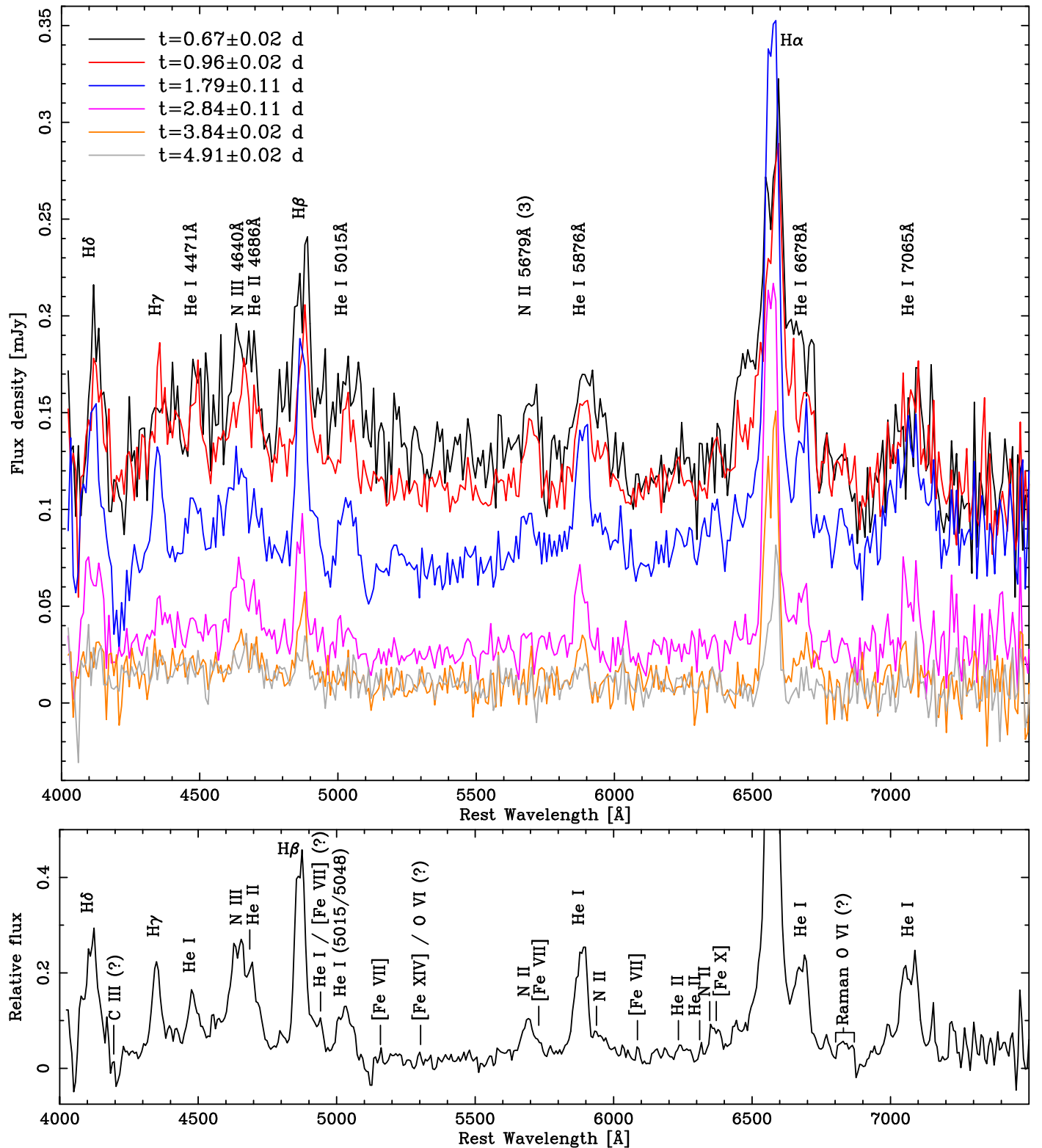
Figure 10. Top: Liverpool Telescope SPRAT flux-calibrated spectra of the 2015 eruption of M31N 2008-12a—see the key for line identifiers. The continuum flux decreases for each successive spectrum. The spectra are consistent with the He/N canonical class of novae. Bottom: combined spectra from the 2012, 2014, and 2015 eruptions; see text for details. Additional features, not identifiable in the individual spectra, are indicated. These include tentative detections of the coronal [Fe VII], [Fe X], and [Fe XIV] emission lines, typically associated with shocks between the ejecta and the surrounding material, and possibly the Raman-scattered O VI emission band, a signature of symbiotic stars. The data used to create this figure are available.

other visible multiplet 38 lines (see Moore 1945). Here, we also note that a number of apparently strong lines in the combined spectrum remain unidentified.

One of the most prominent (see Figure 10) features newly resolved in the combined spectrum is the double-peaked line at ∼6360 Å. If this nova belonged to the Fe II taxonomic class,

Table 5
Galactic Novae with *V*-band Decline Times $t_2 \lesssim 4$ day

Nova	t_2 (days)	t_3 (days)	$P_{\rm rec}$ (years)[†]
T CrB	4	6	80[a]
V1500 Cyg	2	4	…
V2275 Cyg	3	8	…
V2491 Cyg[‡]	4	16	($\gtrsim$100[b])
V838 Her	1	4	…
LZ Mus	4	12	…
V2672 Oph[c]	2.3	4.3	…
CP Pup	4	8	…
V598 Pup[d]	4	…	…
V4160 Sgr	2	3	…
V4643 Sgr	3	6	…
V4739 Sgr	2	3	…
U Sco	1	3	10.3[a]
V745 Sco[e]	2	4	25[a]

Notes. Unless otherwise indicated, all decline data are from Strope et al. (2010).
[†] A recurrence period is quoted only if the system is known, or suspected (in parentheses), to be an RN.
[‡] V2491 Cygni is a suspected RN (Page et al. 2010; Darnley et al. 2011), but only a single eruption has been observed from this system.
References. (a) Schaefer (2010), (b) Page et al. (2010), (c) Munari et al. (2011), (d) Hounsell et al. (2010), (e) Orio et al. (2015).

then the most likely identification of this feature would be as the Si II (6347/6371 Å) doublet. However, despite the greatly improved signal-to-noise of the combined spectrum, there remains no convincing and self-consistent evidence of any other defining lines of the Fe II class (e.g., complete sets of Fe II multiplets themselves or O I lines). Therefore, we instead tentatively identify this pair of lines as N II (6346 Å) and the coronal [Fe X] (6375 Å) line.

The combined spectrum also presents tentative evidence of a full series of [Fe VII] lines, of which there would be nine expected within the observed wavelength range (Nussbaumer et al. 1982). Here we address each of the [Fe VII] line identifications separately.

The [Fe VII] (4698 Å) line would be blended with the He II emission seen at 4686 Å and therefore, due to its low radiative transition probability, would be unobservable.

Any [Fe VII] (4893 Å) line would be blended with the strong Hβ line and hence unobservable.

The [Fe VII] line at 4942 Å may be observed as the small peak just redward of Hβ. However, by virtue of the low transition probability of this line, a more likely identification for this feature would be as the redmost peak of a double-peaked He I (4922 Å) line (such a profile is observed for the other He I lines) or possibly N V (4945 Å). However, we note that the corresponding and similar-probability N V (4604/4620 Å) lines would be mixed with the N III/He II blend (a strong N V [1240 Å] line in early FUV spectra is also reported by M. J. Darnley et al. 2017, in preparation).

There is a possible [Fe VII] line at 4989 Å, but this is within the blue wing of the He I (5015/5048 Å) blend.

There is a tentative detection of [Fe VII] at 5158 Å. The only other possible identifications here would be other, less ionized, but still forbidden, Fe lines.

There is no clear sign of an [Fe VII] line at 5276 Å—a line that could be confused with Fe II (5276 Å) if there were any

other Fe II multiplet 49 lines present—although it could be blended with the line just redward, which may be [Fe XIV] (5303 Å) but could in principle be O VI (5292 Å; see later discussion).

The [Fe VII] line at 5721 Å is tentatively detected in the red wing of the N II (5679 Å) multiplet (#3), which otherwise appears broader than expected based on expected line strength ratios.

The eighth [Fe VII] line is seen at 6086 Å. Another possible identification would be Fe II (6084 Å), but no other multiplet 46 lines are observed. We also note that the [Fe VII] 5721 and 6086 Å lines have the largest transition probabilities within this series (Nussbaumer et al. 1982).

The final [Fe VII] line at 6601 Å has the lowest transition probability, but even so, it would be blended with the Hα emission and would be undetectable in such low-resolution spectra.

After weighing all the above evidence, we believe that it is likely that a series of [Fe VII] lines, the [Fe X] (6375 Å) line, and the [Fe XIV] (5303 Å) line are all visible in the combined spectrum of M31N 2008-12a. The implication of the presence of these highly ionized forbidden lines is discussed in detail in Section 7.1.

Finally, we point to the emission feature at ~6830 Å. As noted by Shore et al. (2014), a possible interpretation of this line is "simply" emission from C I (6830 Å), especially in CNe. However, we also note that other (typically stronger; see Kramida et al. 2015) C I lines (e.g., 6014 and 7115 Å) are not seen in the combined spectrum. Nussbaumer et al. (1989) and Schmid (1989) were the first to propose that an emission band at ~6830 Å could be due to the Raman (1928) scattering of the O VI resonance doublet (1032/1038 Å) by neutral hydrogen. As Shore et al. (2014) also point out, such Raman features are unlikely to be formed in the ejecta of MS- or SG-novae, but such features have been observed in the spectra of RG-novae (most notably, RS Oph; Joy & Swings 1945; Wallerstein & Garnavich 1986; Iijima 2009) and are common features of the wider group of symbiotic stars (Allen 1980). We note that the weaker Raman band at 7088 Å would be blended with the strong He I emission at 7065 Å. Unfortunately, the 6830 Å Raman band is situated adjacent to the telluric B-band (6867–6884 Å, from molecular oxygen), and therefore, the continuum subtraction around the Raman region may be unreliable, and the Raman identification should be treated with some degree of caution. However, we further discuss the potential Raman band emission in Section 7.1, and we stress the importance of targeted follow-up spectroscopy for future eruptions.

6.2. Visible Emission-line Morphology

As was seen following the 2013 eruption (TBW14) and the 2014 eruption (DHS15) and as noted by TBW14, the morphology of the emission lines evolves significantly as the eruption progresses; in particular there is a marked decrease in the width of the line profiles. Figure 11 presents the evolution of the Hα (top) and Hβ (middle) lines during the 2015 eruption; the left-hand plots normalize the flux of the continuum and Hα/Hβ peak to highlight the morphological evolution, and the right-hand plots show the flux-calibrated spectra to illustrate the change in intensity of the lines. As seen in previous eruptions, the Balmer emission lines have a well-defined central double-peaked profile, and the overall width of the profiles decreases with time. At all epochs the redward peak
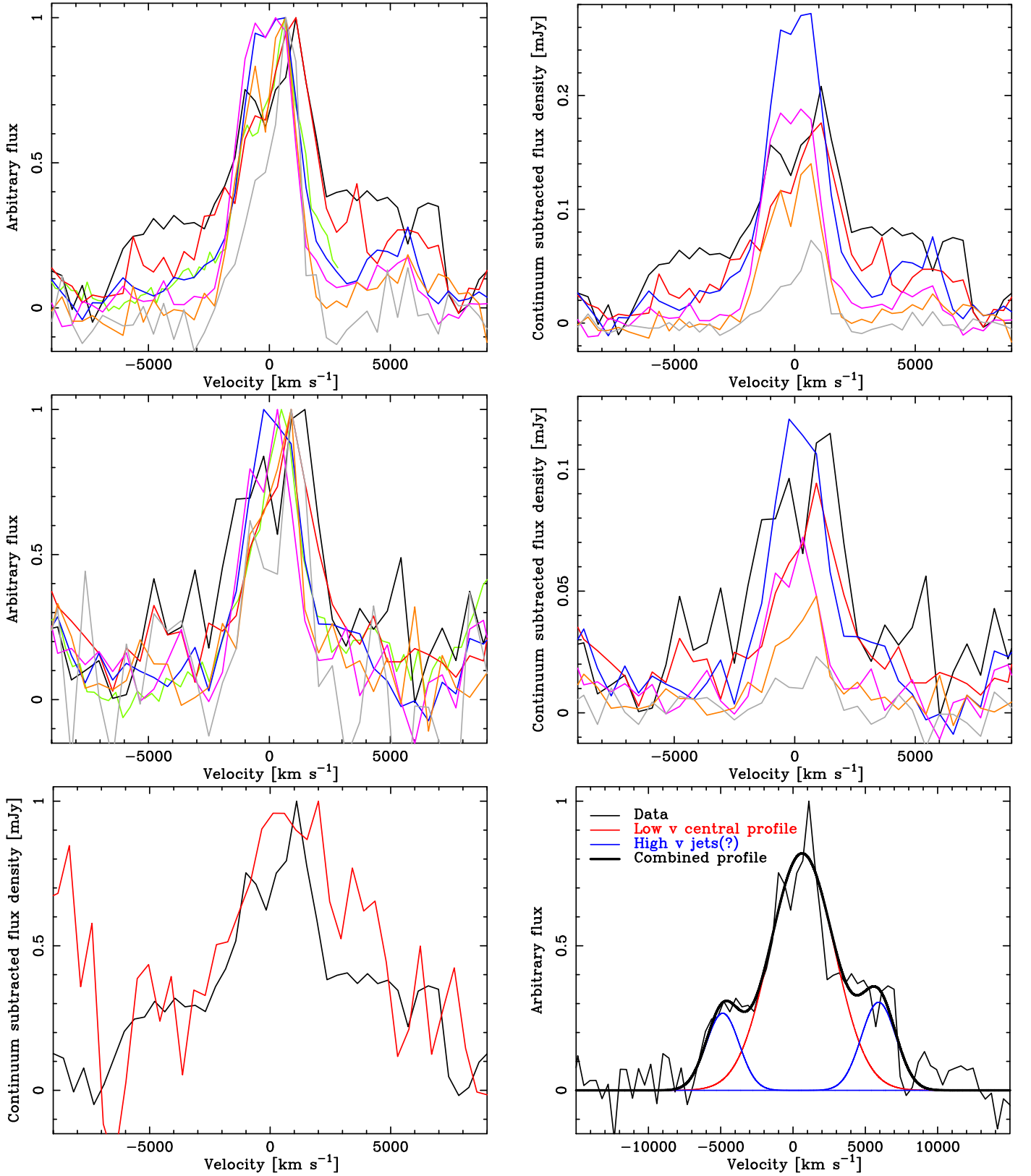
Figure 11. Evolution of the Hα (top) and Hβ (middle) line profiles following the 2015 eruption of M31N 2008-12a. Left: The peak flux of each Hα/Hβ line has been normalized to 1—to indicate the evolution of the line morphology. Right: Flux-calibrated spectra are shown to illustrate the change in flux of the Hα/Hβ emission. Bottom left: Comparison between the Hα and He I (5876 Å) lines at $\Delta t = 0.67$ days; the line blueward of the He I line (~ -8000 km s^{-1}) is N II (5679 Å). Bottom right: Hα line profile at $\Delta t = 0.67$ day; the red and blue lines show a best-fit model of three Gaussian profiles, and the thick black line their combined flux (see Section 7.4). The line colors are the same as in Figure 10 with additional green data $\Delta t = 1.10 \pm 0.01$ days (KPNO; rebinned). The peak redward of Hα ($\sim +5300$ km s^{-1}) is He I (6678 Å). The data in all these plots have been continuum subtracted as described in the text.

Table 6
Evolution of the FWHM of the Hα Profile

Δt (days)	Source	Year	Best-fit Gaussian FWHM (km s^{-1})					
			Hα	Hβ	Hγ	He I (7065 Å)	He I (6678 Å)[a]	He I (5876 Å)
0.67 ± 0.02	LT[b]	2015	4760 ± 520	4140 ± 670	⋯	⋯	⋯	5900 ± 1200
0.96 ± 0.02	LT[b]	2015	3610 ± 310	2520 ± 260	3270 ± 720	4170 ± 860	⋯	2930 ± 610
1.10 ± 0.01	KPNO	2015	2940 ± 50	2440 ± 80	2150 ± 100	⋯	⋯	3570 ± 230
1.14 ± 0.02	LCOGT	2015	3180 ± 110	2470 ± 200	2020 ± 320	⋯	⋯	⋯
1.27 ± 0.01	WHT	2014	2740 ± 70	⋯	⋯	2720 ± 220	2620 ± 240	2300 ± 180
1.33 ± 0.14	LT	2014	2800 ± 110	2370 ± 100	2080 ± 290	2160 ± 330	1540 ± 320	3420 ± 420
1.63 ± 0.10	HET	2012	2520 ± 40	2250 ± 90	2510 ± 110	3220 ± 130	1920 ± 160	2450 ± 110
1.79 ± 0.11	LT	2015	2440 ± 110	2320 ± 170	4960 ± 660	5570 ± 760	1940 ± 460	2490 ± 260
1.8 ± 0.2	Keck	2013	2600 ± 200	⋯	⋯	⋯	⋯	⋯
2.03 ± 0.02	LCOGT	2015	2740 ± 100	1850 ± 220	⋯	⋯	⋯	⋯
2.45 ± 0.18	LT	2014	2340 ± 100	2230 ± 160	2190 ± 360	2040 ± 280	1960 ± 490	2670 ± 250
2.84 ± 0.11	LT	2015	2430 ± 160	2140 ± 230	⋯	2620 ± 570	⋯	2300 ± 310
3.18 ± 0.01	LT	2014	2300 ± 230	⋯	⋯	⋯	⋯	⋯
3.84 ± 0.02	LT	2015	2540 ± 290	2070 ± 300	⋯	⋯	⋯	1860 ± 330
4.6 ± 0.2	Keck	2013	1900 ± 200	⋯	⋯	⋯	⋯	⋯
4.91 ± 0.02	LT	2015	2020 ± 290	⋯	⋯	⋯	⋯	⋯

Notes.
[a] The He I (6678 Å) line flux was computed by first subtracting the best fitting and nearby Hα line profile. Therefore, the values reported here are dependent upon the Hα modeling.
[b] The high-velocity material beyond the central profile, seen predominantly in the two early spectra, is not included in the computed line widths.

of the double-peak is of a flux similar to or higher than the blueward peak's (see Figure 11 top left) in the Hα line. Both Hα peaks are at approximately equal flux when the Hα line has its maximum integrated flux ($t = 1.79$ days; blue line). The blueward peak appears to wane significantly in later spectra ($t = 4.91$ days; gray line). At lower signal-to-noise, however, similar behavior appears to exist for the Hβ line.

In 2014, there was some evidence for higher-velocity material beyond the central peak at early times. In the two earlier 2015 spectra (the earliest spectra yet obtained; see the black and red spectra in Figure 11) we witness evidence of significant emission from very high radial velocity material.

The high velocity material seen in the $t = 0.67$ day spectrum has an approximately "rectangular" profile about the Hα central wavelength, with an FWHM of $\simeq 13,000$ km s^{-1} and FWZI $\simeq 14,500$ km s^{-1} (see Figure 11, particularly the bottom plots). The Hβ equivalent is fainter and therefore noisier, but still shows an FWZI of $\simeq 12,000$ km s^{-1}. By $t = 0.96$ day the emission from this high-velocity material has begun to fade (note that the emission from the central Hα/Hβ component remains approximately constant during this period), and the measured width of the high-velocity profile has reduced by ~ 1000 km s^{-1}. On day 1.1, the high-velocity profile has diminished further, becoming indistinguishable from the continuum around Hβ, but around Hα, the appearance of the He I (6678 Å; $\sim +5300$ km s^{-1}) emission line additionally complicates the profile. In all later spectra (including all spectra obtained prior to the 2015 eruption) any emission from such high-velocity material is absent or at least indistinguishable from the continuum.

There is also evidence for such high-velocity material around the profiles of other (non-H I) lines in the early spectrum. For example, the He I (5876 Å; see Figure 11, bottom left) and He I (7065 Å) lines both appear to have a profile similar to that of the Balmer lines, a double-peaked central profile that is bracketed by a high-velocity "rectangular" profile in early spectra. The similar line profile morphologies and evolution

imply that the H I and He I emission arises from the same part of the ejecta.

6.3. Ejecta Expansion Velocity

To determine the total flux and FWHM of the spectral lines, a fit to the continuum of each spectrum was made using a third-order polynomial. Each spectral line was then separately fit using a single Gaussian profile and a background level; all lines were fit in a consistent manner using data within ± 4000 km s^{-1} of the line center.[54] The line velocities for the Balmer and He I lines are shown in Table 6, and the corresponding line fluxes in Table 7. Generally, a Gaussian profile produced a good fit to the spectral lines; however, the early-epoch Balmer lines with their high-velocity components were not well reproduced with just a single Gaussian (see Figure 11), leading to the larger velocity uncertainties seen in Table 6. For these two early epochs, only the velocity (and line flux) of the central component was calculated using a Gaussian fit. To fit the He I (6678 Å) line, the best-fitting Hα profile was first subtracted from the spectrum to aid the de-blending of the lines. The Hδ, He I (5015/5048 Å), He II, and N lines were not modeled due to a combination of complex profiles, significant blending, or low signal-to-noise. No data were recorded in Tables 6 or 7 if the fitted flux of a line reported a signal-to-noise ratio <3. The available spectra from 2012 and 2014 were also re-analyzed in a manner consistent with the 2015 spectra, and these data, along with those from 2013 (TBW14), are also included in Tables 6 and 7. There was no significant evolution observed in the line flux ratios among the H I or He I lines or in the overall H I/He I ratio.

In Figure 12 we present a plot showing the evolution of the H I (left) and He I (right) integrated line fluxes with time. It should be noted that only the flux of the central part of the

---
[54] The two early-epoch Hα lines were fit over the interval $-7000 \leqslant v \leqslant 4000$ km s^{-1} to permit a better fit to the background level and to avoid contamination from He I (6678 Å; $+5260$ km s^{-1}).

Table 7
Selected Observed Emission Lines and Fluxes from the Nine Epochs of Liverpool Telescope SPRAT Spectra of the 2014 and 2015 Eruptions of M31N 2008-12a

Δt (days)	Source	Year	Flux ($\times 10^{-15}$ erg cm^{-2} s^{-1})[a]					
			Hα	Hβ	Hγ	He I (7065 Å)	He I (6678 Å)[b]	He I (5876 Å)
0.67 ± 0.02	LT[c]	2015	10.5 ± 1.4	7.4 ± 1.5	$\cdots$	$\cdots$	$\cdots$	5.0 ± 1.3
0.96 ± 0.02	LT[c]	2015	7.7 ± 0.8	3.6 ± 0.3	3.8 ± 1.1	2.4 ± 0.7	$\cdots$	2.1 ± 0.5
1.33 ± 0.14	LT	2014	6.8 ± 0.4	4.2 ± 0.2	3.1 ± 0.5	1.8 ± 0.4	1.0 ± 0.3	2.4 ± 0.4
1.79 ± 0.11	LT	2015	10.4 ± 0.6	5.5 ± 0.5	3.6 ± 0.3	3.6 ± 0.6	1.4 ± 0.4	2.7 ± 0.4
2.45 ± 0.18	LT	2014	5.5 ± 0.3	2.7 ± 0.2	2.0 ± 0.4	1.2 ± 0.2	0.8 ± 0.3	1.6 ± 0.2
2.84 ± 0.11	LT	2015	7.8 ± 0.6	2.8 ± 0.4	$\cdots$	1.3 ± 0.4	$\cdots$	1.7 ± 0.3
3.18 ± 0.01	LT	2014	5.1 ± 0.6	$\cdots$	$\cdots$	$\cdots$	$\cdots$	$\cdots$
3.84 ± 0.02	LT	2015	5.5 ± 0.8	1.7 ± 0.3	$\cdots$	$\cdots$	$\cdots$	0.9 ± 0.2
4.91 ± 0.02	LT	2015	2.1 ± 0.4	$\cdots$	$\cdots$	$\cdots$	$\cdots$	$\cdots$

Notes. Line flux is derived from the best-fit Gaussian profile for each emission line and is strongly dependent upon the adopted continuum level.
[a] Here we note that the flux units reported in DHS15 (see their Table 3) were incorrect (see Darnley et al. 2016a).
[b] The He I (6678 Å) line flux was computed by first subtracting the best fitting and nearby Hα line profile. Therefore, the values reported here are dependent upon the Hα modeling.
[c] The high-velocity material beyond the central profile, seen predominantly in the two early spectra, is not included in the computed line fluxes.

emission lines was computed, not the contribution from the early higher-velocity material. As was reported by DHS15, the general trend shows a decreasing of line flux with time for the H I and He I lines. All the H I and He I lines show a decrease in flux during the final rise phase ($0 \leqslant t \leqslant 1$ day), followed by a brief "recovery" at $t \simeq 1.8$ day, before entering a consistent decline.

Throughout we use the FWHM of the best-fit Gaussian profile to the emission lines as a proxy for the line-of-sight ejection velocity; the velocities of the Balmer and He I emission lines for the 2012–2015 eruptions are recorded in Table 6. As previously discussed, the Gaussian profile generally provided a good fit to the lines, at least down to the half-maximum flux, notable exceptions being the Balmer emission in the two earliest spectra. The weighted mean expansion velocity from the Hα line from the 2012–2015 eruptions is 2670 ± 70 km s^{-1}, consistent with the average found following the 2014 eruption (DHS15). However, the measured expansion velocities from the two earliest epochs, $t = 0.67$ and 0.96 days, are significantly higher than the mean and represent velocities not previously seen or predicted (see, for example, Yaron et al. 2005) from this system.

In Figure 13 we show the evolution with time of the Hα profile FWHM velocity from the 2012–2015 eruptions. As a similar analysis following the 2014 eruption indicated (DHS15), there is a clear measurement of decreasing velocity with time. A linear least-squares fit to these data reveals a declining gradient of -300 ± 70 km s^{-1} day^{-1} ($\chi^2_{/\mathrm{dof}} = 3.9$). If the first two, high-velocity data points are excluded, the linear fit is essentially unchanged ($\chi^2_{/\mathrm{dof}} = 3.1$). Again note that the additional high-velocity components seen in the early spectra are not included in these data.

The right-hand plot in Figure 13 shows a log–log plot of expansion velocity against time; by simple inspection these data appear to be well represented by a power law. The best-fitting power law to these data (of the form $v_{\mathrm{exp}} \propto t^n$) has an index $n = -0.28 \pm 0.05$ ($\chi^2_{/\mathrm{dof}} = 2.7$). If we choose to fix the power law index at $1/3$ and $1/2$ (see Section 7.1), then the best fits have $\chi^2_{/\mathrm{dof}} = 2.7$ and $\chi^2_{/\mathrm{dof}} = 5.8$, respectively.

6.4. The X-Ray Temperature and Spectral Variability

The temperature evolution of the SSS phase is shown in Figure 14. This plot is based on simple blackbody fits to all 2013/14/15 X-ray spectra. As in Figure 4(b) the blackbody parametrization assumes a fixed $N_{\mathrm{H}} = 1.4 \times 10^{21}$ cm^{-2}. The spectra have been parametrized individually (see the gray smoothed fit in Figure 14(a)) and also simultaneously in nine groups similar to those in Figure 4(b). Compared to Figure 4(b), the combined group fits have significantly reduced temperature uncertainties as well as a higher time resolution (9 bins in Figure 14 versus 7 bins in Figure 4(b)).

The individual spectral fits in Figure 14 (gray band) tentatively suggest that the observed dip in X-ray flux (cf. Figures 8 and 9) is associated with a dip in temperature. While the substructure of the effective temperature evolution is otherwise well represented by the grouped fits, the temperature dip is not visible there. The reasons for this are most likely that the actual SSS spectrum (a) differs strongly from a simple blackbody continuum and (b) is highly variable. The effective temperature parametrization in Figure 14 represents only a first-order approximation that does not fully capture the actual spectral variations.

The shortcomings of the blackbody model become evident when one looks at the merged and binned spectra of the nine spectral groups which are shown in Figure 15 together with the corresponding blackbody fits. The early and late low-temperature spectra (groups 1, 2, and 9) can still be reasonably well approximated by a blackbody continuum based on the residuals in Figure 15 and the consistent absorption estimates (see Table 14). However, there is little doubt that around the flux maximum (groups 3–8) the spectra show strong additional features and deviate considerably from a simple blackbody continuum. Any further study of the spectral (and flux) variability during the SSS phase has to take these features into account.

For the three groups (1, 2, and 9) that can still be described by blackbody fits, we derive a N_{H} of $0.7^{+0.5}_{-0.5} \times 10^{21}$ cm^{-2} from a simultaneous fit. This estimate should be considered as more accurate than the previous value of 1.4×10^{21} cm^{-2}, which was based on a total spectrum including possible additional features (HND14, HND15). It does, however, still assume a blackbody continuum. The new value is in excellent agreement with the $E_{B-V} \sim 0.1$ (corresponding to $N_{\mathrm{H}} = 0.69 \times 10^{21}$ cm^{-2} via the relation between optical extinction and hydrogen column
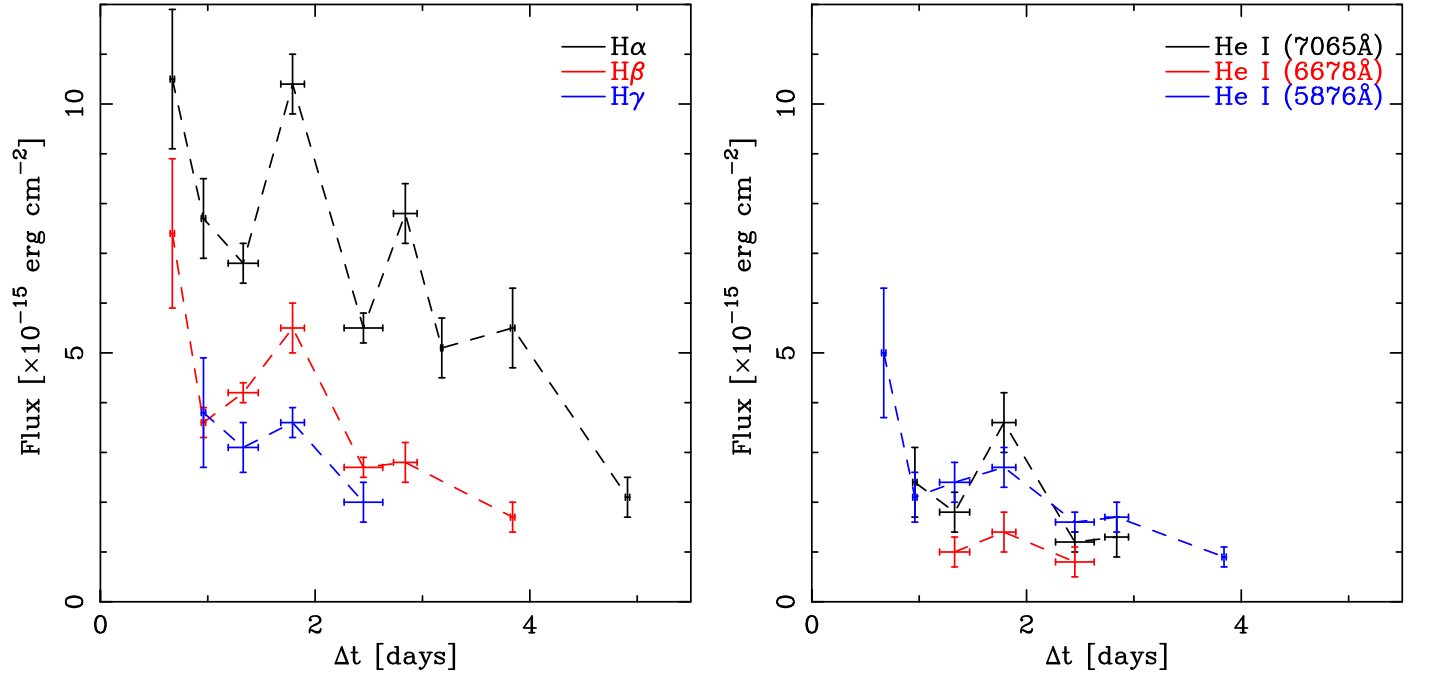
Figure 12. Evolution of the integrated line fluxes of the Balmer (left) and He I (right) lines since the onset of the eruption. The data are from spectra of the 2014 and 2015 eruptions. The dashed lines connecting the points are drawn merely to aid the reader. These fluxes were derived by fitting only the central cores of the emission lines and do not include the higher-velocity material seen during the early spectral epochs.
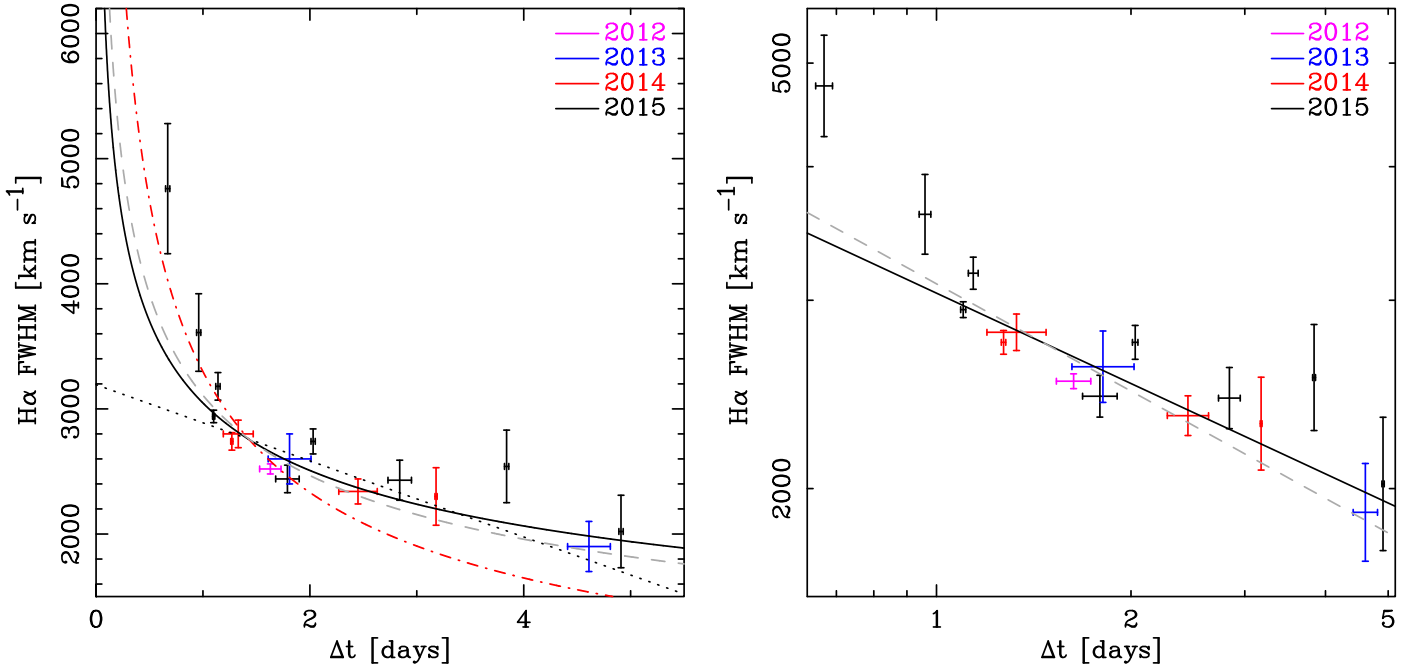

Figure 13. Evolution of the FWHM of the Hα emission line following the eruption of M31N 2008-12a (left: linear axes; right: logarithmic axes). See the key for data point identification. These velocities were derived only from the central cores of the emission lines and do not include the higher-velocity material seen in the first two spectral epochs. The dotted black line shows a simple linear least-squares fit to the 2012–2015 data (gradient = -300 ± 70 km s^{-1} day^{-1}, $\chi^2_{/\mathrm{dof}} = 3.9$; if the first two data points are ignored, $\chi^2_{/\mathrm{dof}}$ reduces to 3.1), the gray dashed line is a power law of an index of $-1/3$ ($\chi^2_{/\mathrm{dof}} = 2.7$; Phase II of shocked remnant development), the red dotted–dashed line is a power law of an index of $-1/2$ ($\chi^2_{/\mathrm{dof}} = 5.8$; Phase III), and the solid black line is the best-fit power law with an index of -0.28 ± 0.05 ($\chi^2_{/\mathrm{dof}} = 2.7$)—see text for details. These observations indicate that the ejecta shock pre-existing circumbinary material close to the central system. The most likely conclusion is that the donor is seeding the local environment via a stellar (red giant) wind.

density from Güver & Özel 2009) found by M. J. Darnley et al. (2017, in preparation).

For the remaining groups (3–8), we attempted to model the X-ray spectra using additional emission components. Here, we

first created an approximate model for each merged spectrum shown in Figure 15 by adding one to three Gaussian emission lines to the blackbody continuum by eye in XSPEC. We then fitted the line parameters using χ^2 minimization until the

residuals showed no strong deviations. In a second step, these models were fitted simultaneously to the (effectively) unbinned individual spectra of each group using Poisson statistics according to Cash (1979). The model parameters were linked, with only the normalizations free to vary for the single spectra. Not all lines for a given group are detected in all the individual spectra, but almost every line has a flux that is significant at the 95% confidence level for at least two different spectra. The only exceptions are the line at 0.76 keV in group 6 and the 0.92 keV line in group 7, each of which is significant only in a single spectrum.

The results of the spectral exploration are summarized in Table 14, where we compare the emission line-enhanced models to pure blackbody fits. We found that likelihood ratio tests (lrt in XSPEC) preferred the models with emission lines over the pure continuum models, with >85 % better likelihood ratios for all groups and >95 % for most. The table also shows that the addition of line components not only improved the fit statistics but led to considerably more consistent (and realistic) values for the absorption column and the blackbody temperature throughout. The N_H values are now consistent with the blackbody fits for groups 1, 2, and 9 as well as with the extinction determination by M. J. Darnley et al. (2017, in preparation). Also, the effective temperatures, although with large uncertainties, are in general consistent with the overall trend in Figure 14.

In Figure 15 we also show the location of known emission lines from H-like and He-like carbon, nitrogen, oxygen, and neon. Table 14 names those lines that are close to the energies of the suggested emission lines. This is not a clear identification of those lines but a first tentative suggestion of those elements that might contribute the additional emission features.

Note that the spectral FWHM of the *Swift* XRT, which is illustrated at the bottom of Figure 15, is broader than some of the excess features that only consist of one or two spectral bins and are therefore unlikely to correspond to individual emission lines. For this reason, we fitted the spectral lines first before overlaying the known transitions so that our analysis would not be biased by associating narrow features with certain laboratory lines.

In terms of Galactic nova low-resolution X-ray spectroscopy, the RNe RS Oph (Osborne et al. 2011) and V745 Sco (Page et al. 2015; see also Section 7.6) showed significant spectral excesses in high statistical quality XRT spectra.

For practical purposes the M 31 blueshift is negligible ($z \sim -0.001$), well below the binning resolution in Figure 15. While additional velocity shifts have been reported for *absorption* lines of Galactic novae (e.g., Ness 2010; van Rossum & Ness 2010), the *emission* features normally show no such effects.

Hot WD atmosphere models (e.g., Rauch et al. 2010; van Rossum 2012) resemble blackbody-like continua cut by sharp absorption features. These features have been observed in X-ray grating spectra of several Galactic novae (e.g., Ness et al. 2013). Therefore, we tested fitting the absorption edge of neutral oxygen at 0.54 keV (prominently seen in RS Oph; e.g., Ness et al. 2007) as well as the N VII ionization edge at 0.67 keV and the O VIII edge at 0.87 keV. In no case did the inclusion of these features result in a statistically better fit or more consistent values of N_H or kT compared to the pure blackbody. Therefore, more complex model atmosphere fits were not attempted. Significantly more exposure time or high-
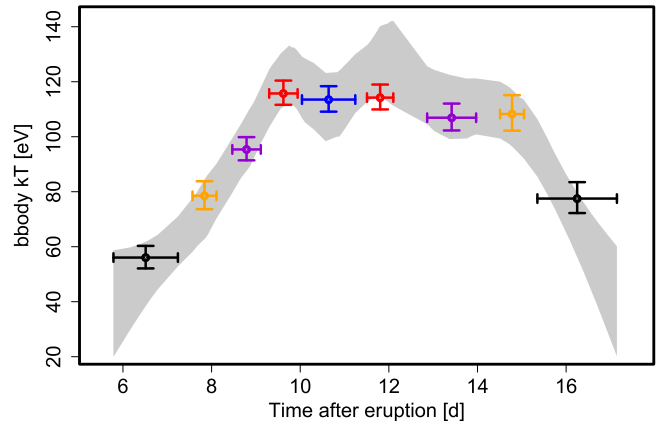

Figure 14. The effective blackbody temperature of M31N 2008-12a depending on the time after eruption. Based on X-ray spectra from the 2015/14/13 eruptions. Sets of spectra with similar temperature (cf. Figure 4(b)) have been fitted simultaneously. Colored data points show the best-fit kT and corresponding uncertainty. The colors are only used for quick identification of the eruption stages in Figure 15 and Table 14 and carry no specific physical meaning. The error bars in time after eruption extend from the first to the last observation of each group. The gray region shows the 95% confidence prediction interval derived from smoothing temperature fits based on individual snapshots. For clarity, these individual fits are not shown. A temperature plateau is suggested between days 9 and 15, with small-scale variations possible due to more complex spectral changes (see Figure 15).

resolution *XMM-Newton* RGS data are required for a solid test of our tentative results.

7. DISCUSSION

7.1. Ejecta Deceleration and Eruption Environment

In DHS15 we presented evidence showing a marked decrease of the inferred velocity of the ejecta based on the line width of the Hα emission from the 2012, 2013, and 2014 eruptions. Similar "decelerations" have been seen in a number of RNe—most notably, in RS Oph (Dufay et al. 1964; Iijima 2009)—and have been linked to the physical deceleration of the ejecta as they interact with significant circumbinary material (in the case of RS Oph, the red giant wind; Pottasch 1967; Bode et al. 2006; Evans et al. 2007).

Bode & Kahn (1985) described the standard three-phase model of the interaction of the ejecta with a shocked $1/r^2$ density profile stellar wind. Phase I is the early stage of the interaction, and the ejecta are still imparting energy to the shocked wind, and the reverse shock, running into the ejecta, remains important. In Phase II there is a period of adiabatic forward shock expansion until the shock temperature decreases and the shocked gas becomes well cooled with the momentum-conserving Phase III of development established. The expected behavior of the observed shock velocities during Phase II and III is well represented by the power laws $v \propto t^{-1/3}$ and $v \propto t^{-1/2}$, respectively.

However, for the 2006 eruption of RS Oph, X-ray emission has revealed that after an ejecta-dominated, free expansion stage (Phase I) lasting ~6 days (Bode et al. 2006), the remnant rapidly evolved to display behavior characteristic of a shock experiencing significant radiative cooling (Phase III). The duration of an adiabatic Sedov–Taylor phase (Phase II) was rather shorter than predicted by the remnant evolution model developed by Bode & Kahn (1985), O'Brien & Kahn (1987), and O'Brien et al. (1992) after the 1985 eruption of RS Oph.
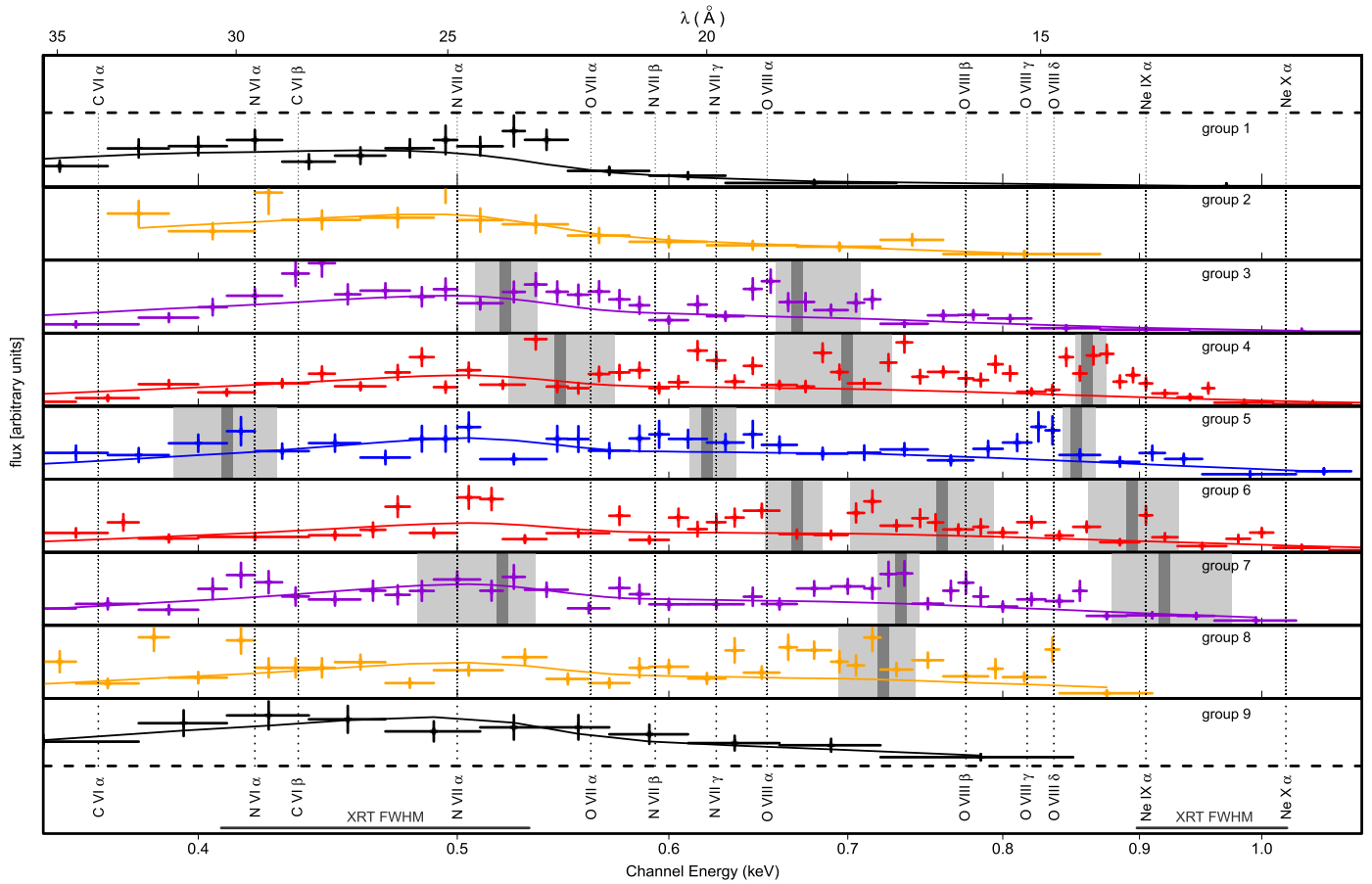
Figure 15. Binned combined XRT spectra in arbitrary flux units with blackbody fits (solid lines). The colors correspond to the eruption stages in Figure 14 with time progressing from top to bottom. For groups 3–8 we show the energies (dark gray) and corresponding uncertainties (light gray) of possible emission lines (see Table 14). Additionally, the energies of known prominent emission lines of H-like and He-like C, N, O, and Ne transitions are indicated by dashed lines (for the He-like triplets, only the forbidden line locations are marked). The relevant line identifications are given at the top and bottom of the figure. The horizontal gray lines at the bottom of the plot show the *Swift* XRT FWHM of ~125 eV in this energy range as determined in XSPEC based on the current XRT calibration files (CALDB version 20160121).

This was due in part to not appreciating at that time the nature of the SSS phase in RS Oph and in part to particle acceleration in the shock (Tatischeff & Hernanz 2007).

Line narrowing has also been witnessed in a number of CNe and RNe that are not expected to have erupted into dense circumbinary environments. Shore et al. (1996) present an alternative interpretation, that simply, higher-velocity material has always traveled the furthest distance, so its emissivity decreases at a greater rate than that of slower-moving material, causing the emission lines to narrow. In systems where the ejecta interact with significant circumbinary material, one would expect a combination of both effects.

The Hα velocity evolution, as presented in DHS15, was best described by a power law of the form $v \propto t^{-0.12\pm0.05}$, clearly incompatible with expectations regarding Phase II or III. Therefore, DHS15 interpreted a velocity evolution over the interval $1.27 \leqslant t \leqslant 4.6$ as Phase I of the shock evolution and based their conclusions upon this interpretation. By direct comparison to the RS Oph system and using the observed velocities from the 2014 eruption, DHS15 determined that Phase I following an eruption of M31N 2008-12a should therefore last for $\gtrsim 3.6$ days after maximum visible light (or $\gtrsim 4.6$ days after the onset of the eruption). The comparison led to an inferred ejected mass from M31N 2008-12a of $\gtrsim 3 \times 10^{-8} M_\odot$.

However, the addition of the 2015 eruption data significantly alters the picture and subsequent interpretation. The DHS15 investigation tied the velocities to the time of maximum visible light, which would make any power-law relation appear too shallow; here we relate the velocities to the estimated time of the eruption (i.e., the start of mass ejection, around one day prior to maximum visible light; see Table 4). The early-epoch spectral observations of the 2015 eruption contain complex line morphologies showing evidence of very high velocity material. The addition of the early- and late-time 2015 data and the shifting of the time-axis (see Table 6 and Figure 13) have the effect of steepening the best-fit power law to $v \propto t^{-0.28\pm0.05}$. These updated data are now entirely consistent with the expected deceleration from Phase II shock behavior as the M31N 2008-12a ejecta interact with surrounding pre-existing material. We also note that the timescale of Phase II would therefore run from $t \simeq 1$ day until $\gtrsim 4.9$ days post-eruption—the time of the final spectrum. The end of Phase II is poorly constrained by the lack of later-time spectra, but it appears that Phase II is consistent with the linear early decline of the NIR–UV light curve (see Section 5).

With knowledge of high, early-time ejecta velocities (FWHM ~13,000 km s^{-1}) we can update the Phase I timescale estimate as presented in DHS15. Bode & Kahn (1985) show that the timescale of Phase I is given by $t \propto M_e u / \dot{M} v_e$, where

M_e and v_e are the ejecta mass and initial velocity, respectively, and $\dot{M}$ and u are the donor mass loss rate and wind velocity, respectively; we will again assume these to be similar to those seen in RS Oph ($v_e = 5100\,\mathrm{km\,s^{-1}}$; Ribeiro et al. 2009; and $M_e = 2 \times 10^{-7}\,M_\odot$; O'Brien et al. 2006; Orlando et al. 2009). For RS Oph, Bode et al. (2006) derived a Phase I timescale of ~6 days, whereas the updated early high velocities for M31N 2008-12a ($v_e = 6500\,\mathrm{km\,s^{-1}}$; taken as the HWHM of the "rectangular" emission line profile) give a timescale of 0.9 ± 0.2 days (post-eruption) for an ejected hydrogen mass of $M_{e,H} = (2.6 \pm 0.4) \times 10^{-8}\,M_\odot$[55] (HND15), consistent with the earliest ($t < 1$ day) spectra of the 2015 eruption, where very high velocity material is seen. Based on Figure 13, it appears that Phase II begins at around $t \simeq 1$ day, consistent with this timescale estimate for Phase I.

These observations, now spanning four consecutively detected eruptions, clearly indicate that the ejecta interact with, and shock, significant pre-existing circumbinary material close to the central system. With eruptions occurring perhaps as frequently as every six months, the local environment will need to be regularly replenished as we expect RNe to be long-lasting phenomena. Therefore, it seems likely that the donor star is seeding the circumbinary environment, not just the WD, via a high mass loss rate—a stellar wind.

If we assume that material is lost from the donor with a velocity of $33\,\mathrm{km\,s^{-1}}$ (akin to the red giant wind velocity of RS Oph; Iijima 2009), then the maximum extent of such material at the time of eruption would be 6.6 au (or 3.3 au for $P_{rec} = 174$ day; see Section 7.5). Assuming the ejecta initially expand with a (HWHM) velocity of $6500\,\mathrm{km\,s^{-1}}$, this wind could *begin* to be cleared from as early as 1.8 days (or 0.9 days for a six-month recurrence period). With the bulk of the ejected material presumably traveling with the mean (but decelerating) velocity of $2670 \pm 70\,\mathrm{km\,s^{-1}}$ the ejecta would *begin* to run off the wind at around 4.3 days (or 2.2 days for $P_{rec} \simeq 6$ months). As the spectra imply that Phase II continues until at least day 4, this suggests that the recurrence period may indeed be ~1 year, although we note that the donor wind velocity may be different from that of RS Oph.

In such a scenario, the high temperatures developed as the ejecta shock any surrounding material is expected to give rise to the so-called "coronal" lines of, for example, [Fe VII], [Fe X], and [Fe XIV], as are observed around 30 days after the eruptions of RS Oph (Rosino & Iijima 1987; Iijima 2009). DHS15 reported that they had observed no evidence of such lines in the *individual* spectra from the 2012 and 2014 eruptions. Such a non-detection was not inconsistent with the shock timescales derived in DHS15. However, with a much accelerated timescale, as derived above, one might expect to see such high-ionization coronal lines in the early-time spectra. By rough extrapolation, day 30 in RS Oph is approximately equivalent to day 4–5 in M31N 2008-12a.[56] As described in Section 6, there are tentative detections of [Fe VII], [Fe X], and [Fe XIV] emission lines in the combined 2012, 2014, and 2015 spectrum. Iijima (2009) reported the appearance of such coronal lines between day 29 and 35 after the 2006 eruption of RS Oph; these lines then strengthened significantly in later spectra.

Therefore, the weak coronal lines detected before day 4 in M31N 2008-12a are roughly consistent with this timescale, and we may expect them to strengthen in later-time spectra. As discussed in DHS15, any hard X-ray emission from such shocks, as was seen by *Swift* from RS Oph (Bode et al. 2006), would be undetectable at the distance of M 31. The same conclusion is found when scaling from the more similar nova V745 Sco (see Section 7.6). Building an argument based on each of these coronal lines individually would be folly, but with five of such lines possibly detected and the "missing" lines easily accounted for, the evidence is quite compelling.

The tentative identification of Raman-scattered O VI emission at ~6830 Å in the combined spectrum (as described in Section 6) potentially provides another independent line of evidence pointing directly at the donor star in the system. Although we cannot completely rule out a C I origin for this line, the lack of other C I lines in the spectrum is somewhat telling. Here we again point to the additional caveats discussed in Section 6.1. Such Raman emission is not seen in classical novae (MS- or SG-novae) but is readily observed in symbiotic stars and RG-novae (nova eruptions within symbiotic systems, e.g., RS Oph).

Taken together, the color–magnitude evolution (see Section 5.6), the $v \propto t^{-1/3}$ power-law ejecta deceleration, the coronal lines, and the possible Raman emission band provide strong evidence describing the environment of the nova. The simplest coherent picture is a WD accreting from the extensive stellar wind of a red giant, with the subsequent nova eruptions then interacting with, and shocking, the extended wind. By virtue of the low ejected mass and high ejection velocity of M31N 2008-12a (both at the extremes of the ranges observed in novae), the early ejecta evolution occurs on timescales significantly shorter than seen in any other novae—days rather than weeks.

Therefore, we conclude that the mass donor in M31N 2008-12a is a red giant. As such, the companion itself will be accessible to NIR photometric (see M. J. Darnley et al. 2017, in preparation, for a detailed discussion of the existing photometry) and possibly even spectroscopic observations. As a natural consequence, the orbital period of the system must be long (of the order of hundreds of days) and will therefore—again uniquely—be similar to the recurrence period. With no strict requirement for the orbits in a long-orbital-period nova to be completely circularized, the inter-eruption periods for M31N 2008-12a may be, intriguingly, sensitive to the orbital phase of the system.

7.2. Spectral Energy Distribution

In Figure 16 we illustrate the spectral evolution of the 2015 eruption of M31N 2008-12a from $\Delta t \simeq 0.7$ days after the eruption (gray points), from $\Delta t \simeq 1$ day at one day intervals up to and including $\Delta t \simeq 6$ days, at $\Delta t \simeq 10$ days, and at quiescence (red data points). In this plot the black data points indicate epochs before the SSS turn-on (all during the linear early decline of the NIR–UV light curve; see Section 5), with the blue data points showing the evolution during the SSS phase. The quiescent data are taken from archival *HST* observations (see DWB14). We have utilized visible and *Swift* UV absolute calibrations from Bessell (1979) and Breeveld (2010), respectively. Here we assume a distance to M 31 of 770 ± 19 kpc (Freedman & Madore 1990) and a line-of-sight reddening of $E_{B-V} = 0.096 \pm 0.026$ (all of a

---

[55] Here, we assume Solar abundances in the ejecta. We note that Kato et al. (2016) assume $X = 0.53$ for the ejecta; if we therefore assume such higher-mass ejecta, the Phase I timescale increases slightly to 1.2 ± 0.2 days.

[56] But also see Kato et al. (2016), who predict an even earlier onset of the eruption in M31N 2008-12a.
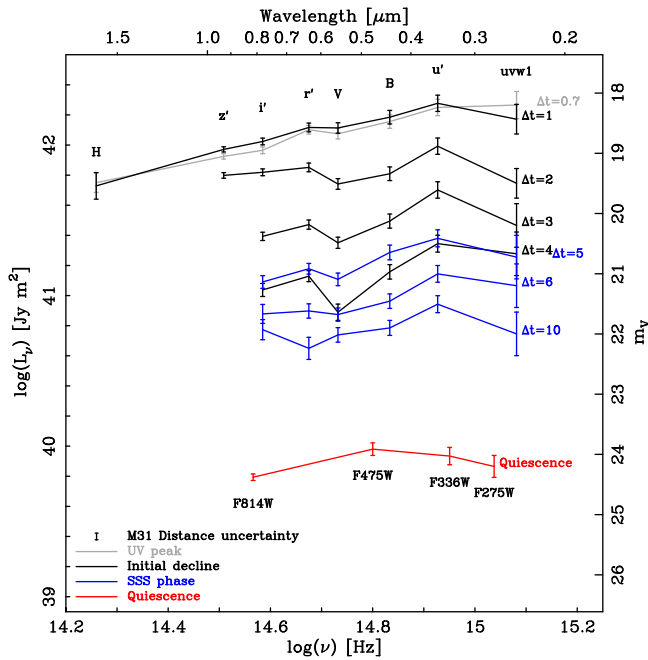
Figure 16. Distance- and extinction-corrected SED plots showing the evolution of the SED of the 2015 eruption ($t = 0.7$ day corresponds to the UV peak, 1–4 day the initial decline, and 5–6 and 10 day the SSS phase). Units are chosen for consistency with similar plots in Schaefer (2010; see their Figure 71) and DWB14 (see their Figure 4). The central wavelength locations of the Johnson–Cousins, Sloan, *HST*, and *Swift* filters are shown to assist the reader. Here the extinction is treated as just the line of sight (Galactic) extinction toward M 31 ($E_{B-V}^{\rm Galactic} = 0.1$; Stark et al. 1992); see the detailed discussion in M. J. Darnley et al. (2017, in preparation). The error bars include contributions from the photometric and extinction uncertainties, and the single black point above the key indicates the systematic uncertainty based on the distance of M 31. A *V*-band apparent magnitude scale (not corrected for extinction) is shown on the right-hand *y*-axis to aid the reader.

Table 8
Indices of Power Laws Fit to the Evolving SED of M31N 2008-12a

Δt (days)	SED Power-law Index[a]
0.7	0.67 ± 0.13
1	0.66 ± 0.07
2	0.27 ± 0.23
3	0.92 ± 0.29
4	0.91 ± 0.33
5	0.86 ± 0.20
6	1.06 ± 0.25
10	0.82 ± 0.29

Note.
[a] Quoted uncertainties are based on random photometric errors; an additional systematic error of 0.09 due to the extinction uncertainty should also be applied to all indices.

foreground Galactic origin; see M. J. Darnley et al. 2017, in preparation, for a complete reddening analysis and discussion). We have utilized the analytical Galactic extinction law of Cardelli et al. (1989; assuming $R_V = 3.1$) to determine the extinction values suitable for the *Swift* UV filters (calculated at the central wavelength of each filter).

Compared to the SED of the 2014 eruption presented in DHS15 (see their Figure 11), the SED coverage from the 2015 eruption is more extensive, following the evolution for over three times as long and over a much broader wavelength regime. In 2014 there was a relatively large time offset between the ground-based (LT) data and the *Swift* UV data, which, given the rapid nature of the evolution, was not ideal. The temporal matching between the ground and *Swift* data for the 2015 eruption is much improved.

When nova ejecta are still optically thick, the continuum emission can be well described by a blackbody with the wavelength of peak emission closely related to the radius of the pseudo-photosphere (see, for example, Gallagher & Ney 1976). As initially discussed in DHS15, these SEDs, even at $\Delta t = 0.7$ day, are not consistent with blackbody emission, not even with the Rayleigh–Jeans tail of "hot," low-photospheric-radius ejecta, as expected from systems with very low ejected mass.

Based on the visible spectra, we know that the emission up to at least $t \simeq 5$ days is a combination of continuum and emission line flux, and we have no reason to expect that this will change significantly at later epochs. As the line flux

contribution from later times is unknown, we chose not to correct any of the SEDs for lines. With this caveat in mind, we fit the SEDs with simple power laws. The spectra up to $t \simeq 1$ day are continuum dominated (see Figure 10), and, as indicated by Figure 12, the integrated line fluxes decrease until after day 1 as the high-velocity component wanes. Fits to the $t = 0.7$ and $t = 1$ day SEDs show power laws with indices of $0.67 \pm 0.13_{\rm random} \pm 0.09_{\rm systematic}$ and $0.66 \pm 0.07_{\rm random} \pm 0.09_{\rm systematic}$, respectively (where the systematic error arises from the reddening determination and persists for all power laws fit to these data). Therefore, at this time, the SED is completely consistent with optically thick free–free emission ($f_\nu \propto \nu^{2/3}$; Wright & Barlow 1975).

From $t \simeq 1.5$ days, the line fluxes initially increase (see Figure 12) against a continuum which decays until $t \simeq 4$ day (the end of linear early-decline phase)—any power-law fits to the SEDs therefore may be increasingly confused by the emission line flux. At $t = 2$ days the slope of the SED has decreased to 0.27 ± 0.23, which could indicate a move toward optically thin free–free emission ($f_\nu \propto \nu^{-0.1}$; Wright & Barlow 1975). However, from $t = 3$ days onward (see Table 8) the general form of the SED is relatively stable and is again consistent with optically *thick* free–free emission. During that period, we just see an overall decrease in flux, although between $t = 4$ days and $t = 5$ days the SEDs are essentially unchanged in flux (see below) as the nova enters the quasi-plateau phase. The mean SED slope across all epochs is 0.69 ± 0.06, consistent with optically thick free–free emission. Without spectra to further constrain the emission, it is difficult to speculate whether the slope change at $t = 2$ days is a genuine transition to optically thin free–free emission, with the later SEDs becoming increasingly line dominated, or it is simply a statistical outlier.

It is interesting to note the behavior of the r'- and *V*-band relative flux as the SED evolves. At $t = 1$ day, when the SED is continuum dominated, these points follow the general optically thick free–free trend, with a hint of an r'-band excess due to the strong Hα emission. As the evolution continues, the r'-band excess strengthens against *V* as the continuum drops and the Hα flux strengthens (as mentioned broadly above), continuing throughout the linear early decline (up to $t \simeq 4$ day). Then as the nova enters the quasi-plateau phase and the SSS turns on ($t \simeq 5$ days), this trend starts to reverse. Between day 4 and 5, the only significant change in the SEDs is an increase in *V*-band flux. By $t \simeq 10$ days, the *V*-band flux

is stronger than the r'-band flux. While late-time spectra are required to confirm what is causing such a trend, it is likely to be line driven. Nebular lines typically begin to appear in nova spectra once the UV becomes optically thin (see, for example, Moro-Martín et al. 2001; Della Valle et al. 2002, which is also related to the unveiling of the SSS). The strongest nebular lines in novae are usually the [O III] (particularly 4959/5007 Å) lines, located within the V-band. Therefore, we predict that M31N 2008-12a enters the nebular phase during its quasi-plateau phase, probably between days 4 and 5.

As described by DWB14 and TBW14, the quiescent SED (indicated by the red data in Figure 16) is consistent with being dominated by a luminous accretion disk; the SED during the late decline phase and the nature of the quiescent system are discussed in detail in the companion paper by M. J. Darnley et al. (2017, in preparation).

We note that the visible peak (for M31N 2008-12a at $t \simeq 1$ day) for a "typical" nova corresponds to the maximum extent of the pseudo-photosphere and the minimal effective temperature ($T_{eff} \simeq 8000$ K). Therefore, such a nova is expected to have a blackbody-like spectrum, which peaks in the visible, at the time of the peak in the visible light curve. As stated in DHS15, we again find that the SED at the visible peak does not correspond to a blackbody peaking in the visible. But now that the extinction is constrained (M. J. Darnley et al. 2017, in preparation), we have also confirmed that the SED at the visible peak is *not* the Rayleigh–Jeans tail ($f_\nu \propto \nu^2$) of blackbody emission from a "hotter" source. Even at such an early stage ($t = 1$ day), the visible emission has already evolved to an (optically thick) free–free form. During the linear initial-decline phase, the NUV *Swift* uvw1 data points are systematically lower than the u'-band data; once the SSS turns on, this "discrepancy" may disappear. Although a single data point alone cannot confirm this, it may be evidence of a transition to an optically thick regime at bluer wavelengths. Together, these SEDs confirm that the emission peak from M31N 2008-12a never moves as redward as the visible and probably not even into the NUV or FUV and that it may always be constrained to the EUV (before shifting back into the X-ray as the SSS is unveiled). Therefore, as the optical depth of the ejecta is so low, we can conclude that the ejected mass in an eruption of M31N 2008-12a must be significantly lower than that in a "typical" CN or even in all other observed RNe. This is in agreement with the theoretical estimates obtained through hydrodynamic simulations when very high values of the WD mass and accretion rate are adopted (see, for example, Hernanz & José 2008).

7.3. X-Ray Spectral Variability

The spectral models summarized in Table 14 suggest that the SSS phase emission of M31N 2008-12a can be consistently described using emission lines superimposed on an absorbed blackbody continuum. The statistical significance of these detections is modest and has not been subjected to the rigorous examination described by Hurkett et al. (2008), which is beyond the scope of this work. Nevertheless, we consider the discussion of the potential origin of these features to be of interest.

Even though no fitted line appears in all groups (cf. Figure 15), there are certain features that several groups have in common. Many of the putative X-ray emission lines fall near known transitions of N VII (0.50 keV), O VII (0.56 keV), or

O VIII (0.65 keV). In the highest-temperature spectra (i.e., groups 4–7) there is weak evidence for Ne emission features (Ne IX α and Ne X α) around 0.9 or 1 keV (group 6 only). However, not all fitted features have obvious laboratory counterparts (see Figure 15), and one must keep in mind that due to the broad XRT spectral response width, narrow observed features in the count spectrum are likely to be a noisy representation of the underlying spectrum at best.

The identification and classification of possible emission lines is complicated further by the strong SSS variability of M31N 2008-12a up to day 13 (see Figure 8). All emission components are potentially variable, and some lines will not necessarily be present in all snapshot spectra of a certain group. The visible differences between the group spectra in Figure 15 already suggest a more complex spectral variability. Incidentally, the group spectra after the end of the early variability phase (i.e., those of groups 7, 8, and 9; see Table 14) appeared to be somewhat more homogeneous and easier to fit than the earlier spectra. These tentative first results need to be tested robustly with high-resolution (*XMM-Newton* RGS) X-ray spectra to enable a confident interpretation of the underlying physics.

For now, the X-ray spectral models suggested for M31N 2008-12a, i.e., a hot photospheric continuum with superimposed emission lines of highly ionized nitrogen, oxygen, and possibly neon, are reminiscent of the high-resolution spectra of the Galactic RN U Sco as discussed by Ness et al. (2012). Their Figure 8 shows strong oxygen features (and weak Ne lines) that appeared as the continuum temperature increased. Ness et al. (2012) suggest that because the strongest emission lines appeared at the peak of the continuum flux, those lines were photoexcitated, and therefore, the plasma that produced them should have been close to the central SSS. Note, however, that Ness et al. (2012) suggest that the Ne lines, together with potential Mg lines, originated more likely in a collisional plasma. In our case, there seem to be no detectable lines beyond the Wien tail of the blackbody model.

Recently, Ness et al. (2013) introduced a phenomenological classification of SSSs, according to their high-resolution spectra, into those exhibiting clear emission lines (SSe) and those exhibiting clear absorption lines (SSa) in addition to a continuum component. They note that SSe objects have on average greater inclination angles. Ness et al. (2013) suggest that SSe spectra indicate an obscuration of the central WD, with observable residual continuum emission due to Thomson scattering. In this picture, emission lines are photoexcited and arise from resonant line scattering. In this model interpretation, M31N 2008-12a would be classified as an SSe, and we discuss the possible implications for its inclination angle in Section 7.4.

We also tried to model the separate high- and low-flux spectra in Figure 8(c) using the same approach as that for the group spectra. The results are included in Table 14. We found that a blackbody continuum plus emission lines again leads to statistically improved and physically more consistent values than the pure blackbody. The estimated column densities have relatively large uncertainties but are consistent with the best group fit of $N_H = 0.7^{+0.5}_{-0.5} \times 10^{21}$ cm^{-2}. The continuum temperatures are not well constrained either. However, they suggest that the high-flux spectra might have a higher blackbody temperature ($\sim$120 eV) than the low-flux spectra ($\sim$90 eV). Taken at face value, this difference would translate (via the Stefan–Boltzmann law) to a factor of $\sim$3 larger flux for
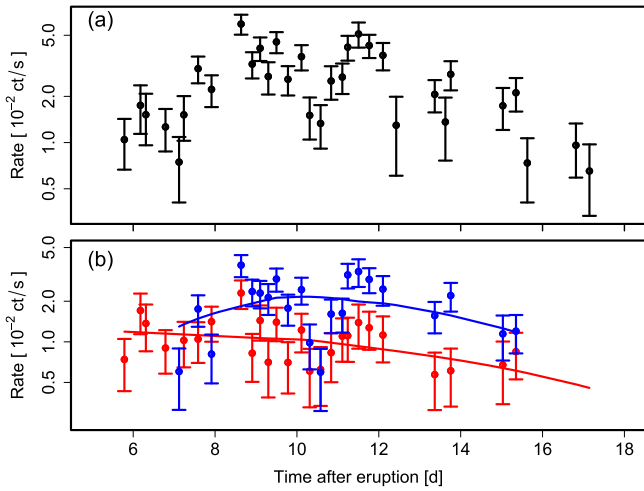
Figure 17. Panel (a): Same as Figure 4(a), but for the 2015 detections only. Panel (b): Light curves for the energy bands of 0.3–0.5 keV (red) and 0.5–1.5 keV (blue) with corresponding smoothed fits based on local regression (solid lines).

the high-state bins, which is consistent with an average factor of 2.6 flux difference between high and low-flux snapshots (see Section 5.7) without the need for a change in radius.

For the identified emission lines, we found no obvious overlap in energies between the high- and low-flux spectra. The two higher-energy lines in Table 14 overlap within their 2σ uncertainties. However, given the current spectral resolution and relatively low number of counts, it is not possible to study the emission line variability with any confidence.

Additionally, based on the group spectra shown in Figure 15 we examined the SSS variability in two different energy bands: 0.3–0.5 keV (soft) and 0.5–1.5 keV (hard). Almost all of the potential emission features were found in the hard band. The resulting light curves for the 2015 eruption are shown in Figure 17. The apparent dip around day 11 appears to be confined to the hard band. Statistical tests confirm that there is significantly (F-test: beyond the 3σ level; p-value = 4.154×10^{-6}) less variability in the soft band (standard deviation = 0.36) than in the hard band ($\sigma = 0.88$). This is further evidence that the early SSS variability is connected to spectral variations.

High-resolution X-ray spectroscopy data will be obtained for a future eruption, using a dedicated *XMM-Newton* RGS observation, in order to study the putative spectral features and their possible variability with much more confidence.

7.4. Geometry, Inclination, and Jets?

The inclination of the M31N 2008-12a system to the line of sight is unknown, but it is one of the key missing ingredients to fully understanding the observations of the eruptions.

Working under the assumption that the surrounding nebulosity was related to past eruptions of M31N 2008-12a and with the morphology of the Hα emission line during the linear early-decline phase, DHS15 employed morpho-kinematical modeling (see, for example, Ribeiro et al. 2009, 2011, 2013) to derive an inclination estimate of $i = 46^{+8}_{-38}$ degrees (where $i = 90$ corresponds to an edge-on, eclipsing system). Here, again, we strongly reinforce the caveats placed on this result by DHS15. For example, this result is likely not unique and is strongly dependent on the assumed connection between

the nova and the nebula, and the nebula has not been significantly re-shaped post-eruption.

Here though, the high-velocity material present in the early spectra may provide some useful constraints on the system inclination. For simplification, in Section 7.1, we work under the assumption that the ejecta and wind are spherically symmetric. The fleeting nature of this high-velocity emission (up to approximately 1 day post-eruption) surrounding the longer-lived and slower central emission component (see Figure 11) is strongly suggestive, as proposed in many novae, of highly asymmetrical ejecta. For example, the observed line profiles are inconsistent with those expected from either a filled or a shell-like spherical system. Given the high velocities initially observed, higher than any velocities previously recorded in novae, we must assume that this material is essentially traveling along, or close to, the line of sight. With the expected geometry of the pre-eruption system, the WD, the donor, the accretion disk, and the bulk of any circumbinary material or stellar wind all lying in the orbital plane, it seems likely that this high-velocity material must have been ejected in the polar direction, where it can expand relatively unimpeded (see, for example, the ejecta geometry of V959 Monocerotis, as described by Chomiuk et al. 2014). With the emissivity of this essentially free-expanding material diminishing rapidly, the spectral evidence is similarly short-lived. With the high velocities seen here already approaching those seen in SNe, we must then infer that the orbital plane of M31N 2008-12a has to be close to being face-on and that the central emission component is due to the equatorial expansion of the ejecta (aligned closely to the plane of the sky). Finally, we note that the inclination derived in DHS15 is not inconsistent with such a geometry.

From the X-ray point of view, there appears to be evidence for additional spectral components beyond a simple (blackbody) continuum model (see Section 6.4). The combined spectra in Figure 15 seem to be consistent with the presence of emission lines. The Galactic study of Ness et al. (2013) discussed a possible link between the presence of strong emission lines in SSS high-resolution X-ray spectra (their SSe class) and the inclination angle of the system. The SSe were interpreted as obscured WDs, and the majority of them had high inclinations. If M31N 2008-12a were an SSe with a high inclination, then this would be somewhat at odds with our conclusions drawn from the visible spectra.

However, the sample of Ness et al. (2013) was still small, and these authors argued for a careful interpretation of the apparent correlation. With only tentative hints at X-ray emission lines in M31N 2008-12a and insufficient evidence on the impact of the inclination angle, more data and a larger Galactic sample are needed to explore and harness the predictive power of X-ray spectral classifications on the binary geometry.

Following radio observations of the 1985 and 2006 eruptions of RS Oph, the presence of a jet or jet-like structure was reported (Taylor et al. 1989; Rupen et al. 2008, respectively). Sokoloski et al. (2008) proposed that the jets in RS Oph are driven by highly collimated outflows, rather than, for example, inherently asymmetric explosions or interaction with the circumbinary medium. The Hα profiles in the new early M31N 2008-12a spectra (see the bottom right plot within Figure 11) are not dissimilar to the Hα lines of RS Oph at day 12 and 15 after the 2006 eruption (see Skopal et al. 2008 and
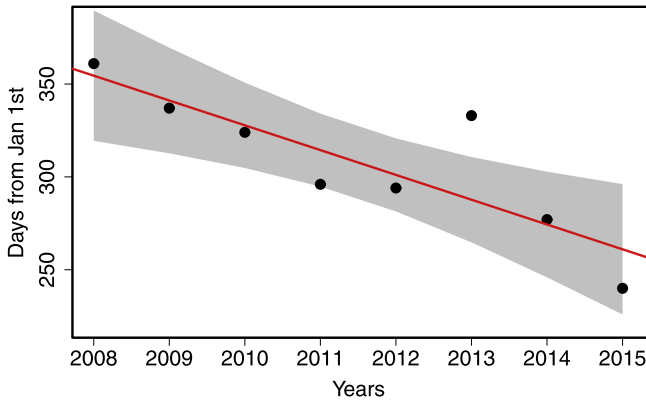
Figure 18. Distribution of eruption dates (in days of the year) over time since 2008. Based on Table 1. The red line is the best fit. The gray area is the corresponding 95% confidence region. The uncertainties of the estimated eruption dates are smaller than the symbol size. Here we show the updated recurrence time fit and scatter, which are the basis for the eruption date predictions in Table 9.

Table 9
Predicted Future Eruption Dates and 1σ Prediction Uncertainty Ranges of M31N 2008-12a Assuming a ~6 Month Recurrence Period; The "a" and "b" Labels Refer to the First and Second Eruptions in a Given Year, Respectively

ID	MJD	Date	Lower limit	Upper limit
2016-b	57647	2016 Sep 16	2016 Aug 21	2016 Oct 13
2017-a	57826	2017 Mar 14	2017 Feb 15	2017 Apr 10
2017-b	58003	2017 Sep 07	2017 Aug 11	2017 Oct 04
2018-a	58179	2018 Mar 02	2018 Feb 03	2018 Mar 29
2018-b	58356	2018 Aug 26	2018 Jul 30	2018 Sep 22
2019-a	58533	2019 Feb 19	2019 Jan 23	2019 Mar 18
2019-b	58710	2019 Aug 15	2019 Jul 19	2019 Sep 11
2020-a	58886	2020 Feb 07	2020 Jan 11	2020 Mar 06
2020-b	59063	2020 Aug 02	2020 Jul 06	2020 Aug 30

their Figure 2; although the velocities in M31N 2008-12a are significantly greater). Figure 11 (bottom right) shows the Hα line profile 0.67 day after the 2015 eruption of M31N 2008-12a; here the high-velocity emission has been isolated as a pair of Gaussian profiles (blue lines) around the central profile (red line). These high-velocity Gaussians have consistent fluxes and widths (mean FWHM = 2800 ± 100 km s^{-1}). The blue and redshifted Gaussians are offset from the rest wavelength by -4860 ± 200 km s^{-1} and 5920 ± 200 km s^{-1}.

With such a high mass accretion rate and accretion disk luminosity (see DWB14) and a proposed red giant donor (hence, a large orbital separation) it seems a reasonable assumption that the M31N 2008-12a accretion disk is particularly massive. Thus, it is a reasonable step to further propose that the accretion disk may survive each eruption. Such a short recurrence period will therefore require accretion to begin soon after each eruption. With disk formation timescales related to the orbital period (see the detailed discussion in Schaefer et al. 2011 and references therein), the long orbital period required by a giant donor would not permit a destroyed or heavily disrupted disk to reform in such a short timescale. Therefore, the proposal of a long-orbital-period, short-recurrence-period system with a giant donor seems to require that the accretion disk persists post-eruption. A surviving accretion disk may be able to provide the collimation mechanism required to drive any jets. This proposal of a surviving accretion disk is further explored in M. J. Darnley et al. (2017, in preparation).

7.5. Recurrence Period

In Figure 18 we show the eruption dates, in days of the year, of every visible detection of an eruption during 2008–2015. The plot and corresponding linear fit show that successive eruptions tend to occur slightly earlier in the year. This trend is significant. Therefore, the observed recurrence period appears to be slightly shorter than one year. Figure 18 is based on HDK15, where an apparent period of 351 ± 11 day was estimated. Including the 2015 eruption, here we find a value of 347 ± 10 day (0.950 ± 0.027 year).

The first long-term analysis of the recurrence period of M31N 2008-12a was also presented by HDK15, who proposed a ~6 month eruption cycle, rather than the approximately yearly one currently observed. This scenario is based on the

historical eruption dates inferred from archival X-ray detections in 1992, 1993 (with *ROSAT*), and 2001 (with *Chandra*). The dates of these eruptions are only consistent with the trend shown in Figure 18 if a shift of ~0.5 year is applied. The simplest explanation for this behavior is that M31N 2008-12a has two eruptions per year. Hereafter we define the "a" and "b" eruptions as the first and second eruption in a given calendar year, respectively.[57] In this picture, the missing "a" eruptions during 2008–15 occurred during the time of March–May while M 31 was in Solar conjunction.

The corresponding recurrence period is 174 ± 10 day or 0.476 ± 0.027 year. As for the above estimate of the apparent recurrence period, the given uncertainty is the standard error of the mean. Individual eruptions appear to deviate from the mean by about ±1 month (1σ; cf. Figure 18). We note that this 1σ prediction window is ~12 times as short as that for the Galactic RN U Sco (Schaefer 2005; Schaefer et al. 2010).

So far, only one eruption per year has been detected. However, as the eruptions of the established "b" sequence tend to occur earlier each year, the predicted "a" eruptions (in the first half of the year) are expected slowly to leave the Sun constraint. In Table 9 we list the predicted future eruption dates, together with their 1σ prediction uncertainties, based on all known eruptions from Table 1. These estimates assume a 6 month period, which we expect to confirm in the coming years.

The data shown in Table 9 and Figure 18 will be updated after each future eruption, which may also allow us to improve the prediction accuracy. A comprehensive search in various archives for historical eruptions is in progress, and the results will be published in the near future.

7.6. Comparison to V745 Scorpii

The Galactic RN V745 Sco can be considered as the closest cousin of M31N 2008-12a. Assumed to be hosting the most massive WD in the Galaxy and to be fueled by wind accretion from an RG companion, this nova shares many of the extreme observational characteristics of our object. Here we discuss the main similarities and differences between these two promising SN Ia progenitor candidates.

V745 Sco belongs to the RG-nova class (Darnley et al. 2012) and has undergone detected eruptions in 1937, 1989, and, most recently, 2014, from which a period of $P_{\rm rec} \sim 25$ years is inferred. However, it should be noted that

---

[57] Assuming the shorter recurrence period, there will be a short period repeating every ~21 years in which a third "c" eruption may occur each year.

with the peak luminosity reaching (only) the 10th magnitude, some eruptions may have been missed, rendering the inferred recurrence period an upper limit (see Shafter 2016 and references therein for a general Galactic nova completeness discussion).

Page et al. (2015) presented a comprehensive X-ray and UV analysis of the 2014 eruption of V745 Sco. Taking into account the uncertainty of the eruption date, they found that photospheric X-ray emission was detected only 4–5 day after eruption, thereby narrowly surpassing the turn-on timescale of M31N 2008-12a. However, in contrast to that of M31N 2008-12a, the SSS phase only lasted until about day 10 (see their Figure 11), instead of day 18, giving V745 Sco the fastest SSS turn-off and the shortest SSS phase observed in any nova so far.

The fact that these timescales are even faster than those in M31N 2008-12a suggests that less matter was ejected and burned during the SSS phase. This would indicate that a smaller amount of hydrogen was necessary to trigger the eruption and that therefore, the WD in V745 Sco would be more massive than that in our case (see the models of Hachisu & Kato 2006). A lower hydrogen content of the accreted material would also lead to a shortening of these timescales, but they react more sensitively to changes in the WD mass (cf. Hachisu & Kato 2006). In either case, the much longer recurrence time of V745 Sco (25 yr versus 0.5 / 1 yr for M31N 2008-12a) suggests that its accretion rate is lower than the $1.6 \times 10^{-7} M_\odot \, \mathrm{yr}^{-1}$ estimated for M31N 2008-12a based on the theoretical models of Kato et al. (2015, who assume a 1 year recurrence period). Additionally, while for M31N 2008-12a we speculate, in Section 7.4, that the short recurrence time may require the accretion disk to stay intact, it may not survive the eruption in V745 Sco, thus delaying the next eruption by at least the time it takes for accretion to resume again.

Page et al. (2015) reported that V745 Sco showed no variability during the early SSS phase. However, the observed smooth rise to peak flux was exceptionally rapid and was essentially covered by only six observations, which might not have been sufficient to capture variability. Interestingly, there appeared to be a dip in effective temperature at the maximum (their Figure 5), which looks similar to our Figure 14.

V745 Sco is a symbiotic system with the WD accreting from an RG companion with a possible orbital period of ~500 days (see Page et al. 2015 and references therein for the controversy on this period). Drake et al. (2016) reported on Chandra spectra of the post-SSS phase (day 16) that showed a shock-heated circumstellar medium. They suggest an orbital inclination close to face-on, similar to the visible evidence for M31N 2008-12a. For both novae, the potential presence of strong emission lines on top of the SSS continuum appears to be somewhat at odds with a low inclination angle (see Section 7.4).

In agreement with NIR studies by Banerjee et al. (2014), Drake et al. (2016) interpreted the observational characteristics of the V745 Sco eruption as a high-velocity blast wave interacting with an RG wind. This is consistent with early Fermi-LAT γ-ray detections (Cheung et al. 2014). Banerjee et al. (2014) showed the narrowing of the Pa β FWHM, suggesting that the shock was propagating into a wind that was not spherically symmetric. Drake et al. (2016) inferred a collimation of the blast wave by an equatorial density enhancement. They also concluded that the WD in V745 Sco is likely gaining mass and is another good SN Ia progenitor candidate.

The early hard X-ray emission in V745 Sco, indicative of shock-heated plasma, was observed with Swift/XRT at count rates which were a factor of ~100 fainter than the maximum during the SSS phase (see Figure 1 in Page et al. 2015). Below we discuss that M31N 2008-12a had a hotter SSS maximum than V745 Sco, which would increase the contrast between the maximum count rate and the early hard emission for our nova by a factor of ~3 based on temperature only. Additionally, the ejected mass of V745 Sco was consistently estimated by Banerjee et al. (2014), Page et al. (2015), and Drake et al. (2016) as $\sim 10^{-7} M_\odot$, which is more than a factor of two higher than that for our object (HND15, DHS15).

Scaling from V745 Sco, this suggests that the luminosity of the early hard X-ray emission in M31N 2008-12a would be significantly more than two orders of magnitude below its SSS maximum. Combining all Swift observations between the visible detection and the SSS turn-on from this year and 2014 (HND15) results in an upper limit of $6.5 \times 10^{-4} \, \mathrm{ct \, s^{-1}}$ (for 47.4 ks of total exposure). This is nearly a factor of 100 below the detected SSS peak ($5–6 \times 10^{-2} \, \mathrm{ct \, s^{-1}}$; see Figure 4 and Table 13). Therefore, the non-detection of hard X-rays is expected, and significantly more exposure would be needed to observe them.

The X-ray spectral evolution of the SSS phase in V745 Sco reached blackbody temperatures of about 90 eV, significantly cooler than M31N 2008-12a (see Figure 11 in Page et al. 2015 and note the artificial shift in temperature for V745 Sco). This is slightly at odds with the (M 31) nova population correlation models of Henze et al. (2014b), which suggest that shorter SSS timescales are linked to higher blackbody temperatures, possibly via the WD mass. However, Page et al. (2015) discuss the possibility that the hydrogen burning in V745 Sco had ceased before the SSS could reach its potential maximum temperature, as evidenced by an almost negligible temperature plateau of only about 2 days (see their Figure 11). In any case, the effective temperature of V745 Sco is very high and qualitatively consistent with its fast SSS evolution.

By virtue of the higher count rates for their Galactic object, Page et al. (2015) could analyze their Swift XRT spectra in much more detail. They fitted the SSS emission with a blackbody continuum plus 5 emission lines and two absorption edges (neutral and H-like oxygen at 0.54 and 0.87 keV). Fixing the line energies to the H-like and He-like transitions of oxygen and neon and He-like magnesium (1.35 keV), they reported significantly improved fit statistics. The neon lines were strongest at the SSS peak, while H-like oxygen and He-like magnesium were significant throughout; however, the He-like oxygen line only occasionally reached significance.

Apart from the Mg line, which is not evident in our XRT spectra, these emission features are similar to those tentatively suggested in M31N 2008-12a (cf. Figure 15 and Table 14). The suggested strengthening of the Ne lines with increasing continuum temperature, here and in V745 Sco, indicates photoexcitation. In contrast to Page et al. (2015), we did not find absorption edges to have a significant impact at any stage of the spectral evolution. Our spectra did not have sufficient counts to model both emission and absorption features at the same time.

In essence, V745 Sco and M31N 2008-12a are two extreme RNe that share several observational characteristics. In both objects, low-mass ejecta appear to interact strongly with the stellar wind from a companion, slowing significantly in the

process and producing high-temperature shocks. Their SSS spectra extend to high temperatures and appear to feature strong, variable emission lines. While the WD in V745 Sco may be more massive, M31N 2008-12a appears to have a higher accretion rate, providing the unique opportunity to observe at least one eruption per year. Assuming an ∼25 year cycle, the next eruption of V745 Sco is expected around 2039, by which time we will have studied M31N 2008-12a to a sufficient extent to provide detailed predictions on the variations in the eruption properties of V745 Sco.

8. SUMMARY AND CONCLUSIONS

The 2015 eruption of M31N 2008-12a was discovered independently by dedicated monitoring programs utilizing the *Swift* orbiting observatory and the LCOGT 2 m (Hawaii) on 2015 August 28.41 UT and 28.425, respectively, with pre-eruption non-detections constraining the time of the eruption to 2015 August 28.28 ± 0.12 UT. Following detection, a pre-planned panchromatic follow-up campaign was initiated which involved ten ground-based telescopes around the globe, but was spearheaded by *Swift*, the LT, and the LCOGT.

The eruption light curves spanning the electromagnetic spectrum from the supersoft X-rays to the I/i'-band show remarkable similarity between the 2013, 2014, and 2015 eruptions. The combined visible spectrum from the 2012, 2014, and 2015 eruptions shows tentative evidence for high-excitation coronal lines of [Fe VII], [Fe X], and [Fe XIV], often observed during high-temperature shocks, and also hints at the presence of Raman-scattered O VI emission, as seen in spectra of symbiotic stars and novae with red giant companions. The visible spectra from the 2012–2015 eruptions show a consistent decrease in line width. Between days 1 and 4 post-eruption, this deceleration is consistent with a power-law decline of the ejection velocity ($v \propto t^{-1/3}$). This deceleration is consistent with adiabatic Phase II shock development as the ejecta interact with significant pre-existing circumbinary material. These observations, backed up by the color–magnitude behavior, point to the donor being a red giant in a long-orbital-period system.

Below we summarize a number of our conclusions.

1. The color–magnitude evolution in the visible appears more consistent with the behavior of RS Oph and V745 Sco (both harboring red giant donors) than that of sub-giant (e.g., U Sco) or main-sequence (T Pyx) donor RNe.
2. There is no evidence at visible wavelengths for optically thick photospheric emission during the early evolution of the eruption. This points to a high *minimum* temperature of the expanding photosphere, with photospheric emission therefore peaking in the FUV or EUV.
3. The evolving SED of the eruption points to optically thick free–free emission being the dominant process (in the NIR–NUV) throughout the evolution from $t = 0.7$ day to $t = 10$ day, although significant contribution to the SED from emission lines cannot be ruled out beyond day four.
4. The V- and r'-band trends in the SED lead to a prediction of the nebular phase beginning as early as day 5 post-eruption.
5. Emission from extremely high velocity (FWHM $\simeq$ 13,000 km s^{-1}) material seen only in the early spectra ($t \lesssim 1$ day) is indicative of outflows along the polar direction—possibly highly collimated outflows or jets.
6. We obtained an unprecedentedly detailed UV light curve with *Swift* UVOT, observing for the first time the rise to the maximum and fast decline with subsequent plateaus. The UV peak clearly precedes the visible peak.
7. The X-ray light curve of the 2015 eruption was consistent with the last two years in its timescales, $t_{\mathrm{on}} = 5.6 \pm 0.7$ day and $t_{\mathrm{off}} = 18.6 \pm 0.7$ days, as well as in the properties of the early SSS variability and its cessation around day 13.
8. The 2015 X-ray light curve also showed evidence of a peculiar dip around day 11, which might have been present in the 2013 light curve as well.
9. Merged X-ray spectra tentatively suggest the presence of high-ionization emission lines superimposed on a photospheric continuum that reaches blackbody temperatures of around 120 eV.

The next eruption of M31N 2008-12a is predicted for 2016 mid-September with a 1σ uncertainty of about 1 month. This prediction holds for both the 1 year and the 6 month recurrence scenarios. In the case of the 6 month period, we expect the subsequent eruption in 2017 February–April.

Facilities: Liverpool:2 m, FTN, OO:0.65, MLO:1 m, BAT, OAO:0.5 m, *Swift*, Mayall.

Software: IRAF (v2.16.1; Tody 1993), Starlink (v2015B; Disney & Wallace 1982), APHOT (Pravec et al. 1994), HEASOFT (v6.16), XIMAGE (v4.5.1), XSPEC (v12.8.2; Arnaud 1996), XSELECT (v2.4c), R (R Development Core Team 2011).

APPENDIX A
VISIBLE AND NEAR-INFRARED PHOTOMETRY

A.1. LT Photometry

Significant maintenance work was carried out on the LT between the 2014 and 2015 eruptions, including re-aluminization of both the primary and secondary mirrors. This work, coupled with additional improvements, achieved approximately a doubling of the throughput of the telescope (averaged across all wavelengths). The improvements were significantly greater in the blue, with a $\sim$225% increase in u'-band throughput. These improvements, along with the realization of the extreme blue nature of the eruptions of M31N 2008-12a (DHS15), motivated us to amend our LT strategy from 2014 and include the u' filter for monitoring the 2015 eruption. To achieve a more complete coverage of the SED of the eruption, we also included the z'- and H-band filters in our follow-up program. Hα observations were not employed this year (unlike the previous year) as M31N 2008-12a faded beyond detectability in Hα before it did in the broadband R/r' filters (see DHS15), behavior that is unusual for novae.

A pre-planned broadband (u'-, B-, V-, r'-, i'-, and z'-band) photometry program employing the IO:O detector was initiated on the LT immediately following the LCOGT detection of the 2015 eruption of M31N 2008-12a.

The LT observing strategy again involved taking 3×120 s exposures through each of the six filters for every epoch. The LT robotic scheduler was initially requested to repeat these observations with a minimum interval (between repeat observations) of 1 hr. This minimum interval was increased to 1 day from the night beginning 2015 September 3 UT. To counter the signal-to-noise losses as the nova faded, the exposure time was increased to 3×300 s in the u'-band and 3×180 s in all other filters from August 30.5 UT onward. The exposure times were subsequently increased to 3×300 s in all filters from September 2.5 UT onward and then to 3×450 s in u', B, V, and r' from September 3.5 onward as the nova faded. From September 11.5 UT onward, the r'-, i'-, and z'-band eruption monitoring ceased due to consecutive non-detections on previous nights. There were no V-band observations after September 15 UT and no B observations after September 17. LT observations following the 2015 eruption formally ended on September 22 UT; the r'-band monitoring campaign for the

next eruption (following the strategy described in Section 3) had begun on 2015 September 11.

The LT data were pre-processed at the telescope and then further processed using standard routines within Starlink (Disney & Wallace 1982) and IRAF (Tody 1993). PSF fitting was performed using the Starlink `photom` (v1.12-2) package. Photometric calibration was achieved using 17 stars from Massey et al. (2006) within the IO:O field (see Table 10; expanded from the original version in DHS15). Transformations from Jester et al. (2005) were used to convert these calibration stars from *UBVRI* to $u'g'r'i'z'$. In all cases, uncertainties from the photometric calibration were not the dominant source of error.

For the 2015 eruption, we also employed the newly commissioned IO:I NIR imager (Barnsley et al. 2016), a Teledyne 2,048 $\times$ 2,048 Hawaii-2RG HgCdTe array providing a $6'.27 \times 6'.27$ field of view. The IO:I instrument provides a fixed H-band filter, and each observation comprised of 9×60 s exposures using a 9 pointing (3×3) dither pattern with a $14''$ spacing between each pointing. The IO:I data were reduced by a pipeline running at the telescope; this included bias subtraction, correlated double sampling, non-linearity correction, flat fielding, sky subtraction, registration, and alignment (see Barnsley et al. 2016 for details). Photometry was performed on the reduced data as described above for IO:O. Photometric calibration was carried out using sources in 2MASS (Skrutskie et al. 2006; see Table 10).

A.2. LCOGT 2 m Photometry

The LCOGT 2 m observing strategy was identical to that of the LT. Here we made observations through the u'-, B-, V-, r'-, and i'-band filters using the Spectral CCD camera. Due to weather and scheduling constraints, LCOGT observations of the 2015 eruption were only obtained on the night of 2015 August 28 UT. The LCOGT data were pre-processed at the telescope and then reduced in an identical fashion to the LT IO:O data.

A.3. Ondřejov Observatory 0.65 m Photometry

Photometric observations at Ondřejov started shortly after the maximum brightness of the 2015 eruption of the nova on 2015 August 29.814 UT. We used the 0.65 m telescope at the Ondřejov Observatory (operated partly by Charles University, Prague) equipped with a Moravian Instruments G2-3200 CCD camera (using a Kodak KAF-3200ME sensor and standard *BVRI* photometric filters) mounted at the prime focus. For each epoch, a series of numerous 90 s exposures was taken (see Table 11 for total exposure times for each epoch). Standard reduction procedures for raw CCD images were applied (bias and dark-frame subtraction and flat field correction) using APHOT[58] (Pravec et al. 1994). Reduced images within the same series were co-added to improve the signal-to-noise ratio, and the gradient of the galaxy background was flattened using a spatial median filter via the SIPS[59] program. Photometric measurements of the nova were then performed using aperture photometry in APHOT. Five nearby secondary standard stars (including #9 and #11 listed in Table 10) from Massey et al. (2006) were used to photometrically calibrate the magnitudes.

---

[58] A synthetic aperture photometry and astrometry software package developed by M. Velen and P. Pravec at the Ondřejov Observatory.
[59] http://ccd.mii.cz

Table 10
Photometry Calibration Stars in the Field of M31N 2008-12a Employed with the LT, LCOGT, and MLO Observations

#	R.A. (J2000)[a]	Decl. (J2000)[a]	U	B	V	R	I	J	H	u'	g'	r'	i'	z'
1	0^{h}45^{m}11^{s}73	+41°53′52″2	19.098	18.635	17.759	17.270	16.782	16.001	15.789	19.887	18.165	17.501	17.257	17.072
2	0^{h}45^{m}12^{s}71	+41°54′48″5	18.166	17.711	16.873	16.423	16.010	15.495	14.979	18.968	17.256	16.631	16.455	16.331
3	0^{h}45^{m}14^{s}35	+41°55′5″4	20.765	19.600	18.239	17.412	16.635	15.708	15.185	21.557	18.936	17.777	17.270	16.851
4	0^{h}45^{m}15^{s}43	+41°54′6″9	18.953	18.963	18.319	17.953	17.566	⋯	⋯	19.703	18.585	18.159	18.006	17.903
5	0^{h}45^{m}18^{s}25	+41°54′38″3	19.047	18.933	18.200	17.778	17.353	⋯	⋯	19.796	18.520	18.002	17.815	17.681
6	0^{h}45^{m}19^{s}69	+41°56′5″9	17.808	17.740	17.068	16.680	16.290	15.783	15.625	18.568	17.351	16.896	16.741	16.635
7	0^{h}45^{m}22^{s}59	+41°53′37″5	17.097	16.352	15.607	15.197	⋯	14.351	14.018	18.018	15.934	15.404	⋯	⋯
8	0^{h}45^{m}22^{s}75	+41°55′6″6	21.744	20.532	19.087	18.183	17.233	16.582	15.783	22.515	19.834	18.590	17.926	17.366
9	0^{h}45^{m}25^{s}24	+41°55′32″6	19.634	19.121	18.233	17.742	17.278	16.721	16.116	20.432	18.646	17.970	17.748	17.582
10	0^{h}45^{m}27^{s}48	+41°55′30″4	17.998	17.606	16.785	16.331	15.911	15.307	14.849	18.789	17.158	16.550	16.368	16.238
11	0^{h}45^{m}28^{s}55	+41°54′51″7	19.527	19.162	18.349	17.876	17.358	⋯	⋯	20.314	18.717	18.118	17.846	17.637
12	0^{h}45^{m}30^{s}01	+41°53′20″9	18.772	17.991	16.945	16.318	⋯	14.938	14.445	19.582	17.453	16.616	⋯	⋯
13	0^{h}45^{m}30^{s}20	+41°56′4″8	18.535	18.362	17.640	17.230	16.833	16.299	15.148	19.305	17.953	17.447	17.285	17.174
14	0^{h}45^{m}30^{s}50	+41°55′11″9	15.588	15.410	14.738	14.367	⋯	13.574	13.270	16.379	15.021	14.566	⋯	⋯
15	0^{h}45^{m}34^{s}14	+41°55′4″1	18.490	18.002	17.030	16.496	15.964	15.288	14.742	19.248	17.493	16.732	16.448	16.227
16	0^{h}45^{m}39^{s}98	+41°55′32″0	18.341	17.452	16.416	15.810	15.300	14.549	14.068	19.186	16.918	16.091	15.827	15.624
17	0^{h}45^{m}46^{s}80	+41°54′0″0	18.139	18.074	17.375	16.949	16.546	15.881	15.580	18.888	17.674	17.191	17.025	16.908
	0^{h}45^{m}32^{s}50	+41°54′43″3	PSF Star											

Note. Updated calibration photometry from that presented in Darnley et al. (2015e). Astrometry and *UBVRI* photometry from Massey et al. (2006, 2011), *JH* photometry from 2MASS (Skrutskie et al. 2006), and Sloan *u'g'r'i'z'* photometry were computed via the transformations in Jester et al. (2005; see their Table 1). A finding chart showing the position of M31N 2008-12a and the position of these 17 calibration stars is shown in Figure 19.
[a] Astrometry based on that published by Massey et al. (2006); does not take into account any of the corrections reported in Massey et al. (2016).

Table 11
Visible and Near-infrared Photometric Observations of the 2015 Eruption of M31N 2008-12a

Date (UT)	Δt (days)	MJD 57 000+ Start	MJD 57 000+ End	Telescope and Instrument	Exposure (s)	Filter	SNR	Photometry
2015 Aug 28.971	0.691	262.969	262.973	LT IO:O	3×120	B	114.3	18.726 ± 0.011[a]
2015 Aug 29.192	0.912	263.190	263.195	LT IO:O	3×120	B	148.1	18.654 ± 0.009
2015 Aug 29.301	1.921	263.301		MLO 1.0 m	1200	B	…	18.71 ± 0.06[b]
2015 Aug 29.405	1.125	263.405		MLO 1.0 m	1200	B	…	18.71 ± 0.06[b]
2015 Aug 29.462	1.182	263.460	263.465	LCOGT Spectral	3×120	B	25.6	18.966 ± 0.044

References. (a) Darnley et al. ([2015d](#)), (b) Shafter et al. ([2015b](#)), (c) Hornoch et al. ([2015a](#)), (d) Darnley et al. ([2015c](#)), (e) Henze et al. ([2015c](#)), (f) Darnley et al. ([2015a](#)), (g) Arai et al. ([2015](#)), (h) Chen et al. ([2015](#)), (i) Hornoch et al. ([2015b](#)), (j) Shafter ([2015](#)), (k) Darnley et al. ([2015b](#)), (l) Fabrika et al. ([2015](#)), (m) Hornoch & Fabrika ([2015](#)).

(This table is available in its entirety in machine-readable form.)

The photometry was reported in Hornoch et al. ([2015a](#), [2015b](#)) and is presented in Table [11](#).

A.4. MLO 1.0 m Photometry

Photometric observations of M31N 2008-12a were carried out on 2015 August 29 UT over a 7 hr period between August 29.238 and August 29.511 (within a day of the discovery of the 2015 eruption) and on August 30.292 and 30.312 using the MLO 1 m reflector. Exposures were taken through each of the Johnson–Cousins B, V, R, and I filters (see Bessell [1990](#); I-band only on August 30) and imaged on a Loral 2, 048 $\times$ 2, 048 pixel CCD camera. The data were initially processed (bias-subtracted and flat-fielded) using standard routines in the IRAF software package. The individual images for a given filter were subsequently aligned to a common coordinate system and averaged forming master B-, V-, R-, and I-band images. Calibrated B, V, R, and I magnitudes for M31N 2008-12a were then determined by comparing the instrumental magnitudes for the nova with those of several nearby secondary standard stars (#9–12 and #14; see Table [10](#)) using the IRAF `apphot` package. The resulting magnitudes were reported in Shafter et al. ([2015b](#)), Shafter ([2015](#)), and Hornoch et al. ([2015b](#)); they are presented in Table [11](#).

A.5. BTA 6.0 m Photometry

Additional photometry of M31N 2008-12a was collected by the Russian BTA 6 m telescope at the Special Astrophysical Observatory in the Caucasus Mountains in the south of the Russian Federation. The observations were conducted using the SCORPIO instrument (Afanasiev & Moiseev [2005](#)) on 2015 September 4.85 UT and September 6.03. Photometric calibration was conducted using stars from the Massey et al. ([2006](#)) catalog. The photometry was reported in Fabrika et al. ([2015](#)) and Hornoch and Fabrika ([2015](#)), and these data are included in Table [11](#).

A.6. CBO 0.3 m Telescope Photometry

Observations of M31N 2008-12a were conducted on 2015 August 28 and 30 UT using the 0.3 m telescope at the CBO in Kunsha Town, Ngari, Tibet, China. On each night, a series of three 4×600 s observations was taken through a V-band filter. The subsequent photometry was calibrated using reference stars from the UCAC-4 catalog (Zacharias et al. [2013](#)). The

CBO photometry was reported in Chen et al. ([2015](#)) and is contained within Table [11](#).

A.7. Nayoro Observatory of Hokkaido University 1.6 m Photometry

M31N 2008-12a was observed by the 1.6 m Pirka telescope at the Nayoro Observatory, Faculty of Science, Hokkaido University, Japan, on the night of 2015 August 28. A pair of V-band exposures were obtained using the multispectral imager (Watanabe et al. [2012](#)). These observations were reported by Arai et al. ([2015](#)) and are recorded in Table [11](#).

A.8. OAO 0.5 m Photometry

A pre-eruption upper limit for M31N 2008-12a was obtained by the OAO 0.5 m MITSuME Telescope (Kotani et al. [2005](#)), equipped with an Apogee Alta U6 camera, on 2015 August 27.677 UT. The MITSuME observation was published in Arai et al. ([2015](#)) and is included in Table [11](#).

A.9. iTelescope.net T24 Photometry

Photometric observations of M31N 2008-12a were carried out remotely with iTelescope.net utilizing the T24 telescope, a Planewave 24 inch CDK Telescope f/6.5, and a FLI PL-9000 CCD camera at the hosting site in Sierra Remote Observatory, Auberry, CA, USA. V-band observations were taken at 2015 August 30.2041 UT; they were reported by Arai et al. ([2015](#)) and are presented in Table [11](#).

APPENDIX B
VISIBLE SPECTROSCOPY

B.1. LT SPRAT Spectroscopy

Spectroscopy of the 2015 eruption of M31N 2008-12a was obtained on five successive nights from 2015 August 28–September 02 using the SPRAT spectrograph (Piascik et al. [2014](#)) in the blue-optimized mode on the LT. A slit width of $1''8$ was used, yielding a spectral resolution of ~20 Å and a velocity resolution of ~1000 km s^{-1} at the central wavelength of 5850 Å.

On the night of 2015 August 28, following the detection of the 2015 eruption, the LT made four separate spectroscopic visits, attempting 3×900 s exposures each time. The first visit occurred at August 28.95 UT, just half a day after the discovery of the eruption. The second and third epochs at August 29.06 UT and August 29.13 both suffered significantly from variable
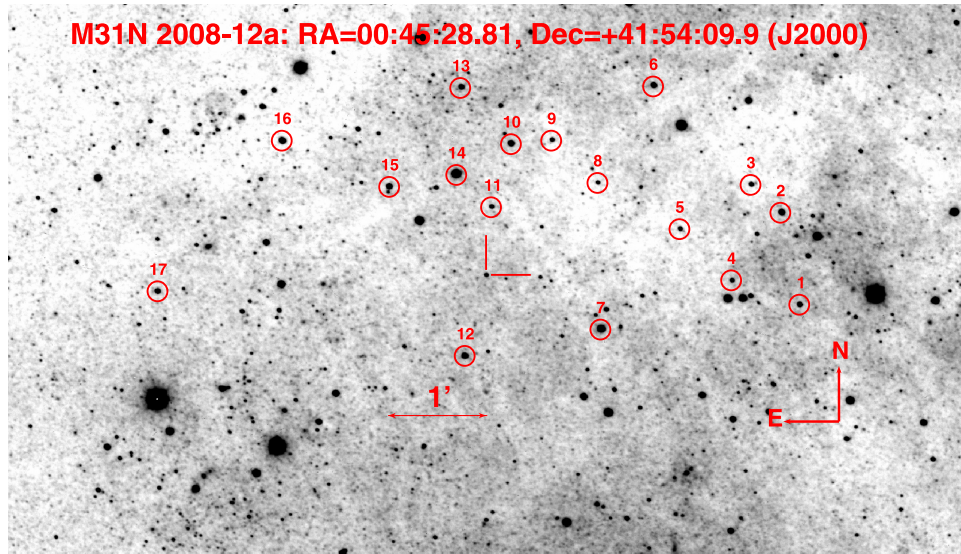
Figure 19. Eruption finding chart for M31N 2008-12a also indicating the 17 photometry calibration stars used throughout and summarized in Table 10.

Table 12
Color Evolution of the 2015 Eruption of M31N 2008-12a

Date (UT)	$t - t_{max}$ (days)	JD 2 456 000.5+		Telescope and Instrument	Filters	Color
		Start	End			
2015 Aug 28.906	0.626	262.802	263.009	*Swift* UVOT / LT IO:I	$(uvw1 - u')$	-1.066 ± 0.190
2015 Aug 29.505	1.225	263.398	263.612	*Swift* UVOT / LT IO:I	$(uvw1 - u')$	-1.100 ± 0.176
2015 Aug 29.921	1.641	263.796	264.046	*Swift* UVOT / LT IO:I	$(uvw1 - u')$	-0.848 ± 0.151
2015 Aug 30.248	1.968	264.200	264.296	*Swift* UVOT / LT IO:I	$(uvw1 - u')$	-0.542 ± 0.102
2015 Aug 30.920	2.640	264.895	264.944	*Swift* UVOT / LT IO:I	$(uvw1 - u')$	-0.566 ± 0.301

(This table is available in its entirety in machine-readable form.)

but thick cloud and the effects of a bright, full, and nearby moon, and the data were subsequently discarded due to low signal-to-noise; the fourth visit took place at August 29.24. Significant spectral evolution (see Section 6) was seen between the first and fourth visits, so these spectra were not combined.

On each of the nights of 2015 August 29 and 30, the LT made two separate spectroscopic observations with 3 × 900 s exposures each. As the nova had faded substantially and no significant evolution was seen between the spectra, the six exposures from each of these two nights were combined into a pair of spectra. On each of the nights of 2015 September 01 and 02, the LT made a single spectroscopic observation with 3 × 1200 s exposures each. The exposure time was increased from previous nights to counter the decreasing luminosity of the nova. Spectroscopic observations on subsequent nights were not attempted as M31N 2008-12a had faded below the useful brightness of the instrument. The nights of 2015 August 29 and 31 and September 01 and 02 were photometric, August 28 suffered from thick cloud, and August 30 had light cloud. A log of the spectroscopic observations subsequently used for analysis is provided in Table 2.

Following bias subtraction, flat fielding, and cosmic-ray removal, data reduction was carried out using the Starlink figaro (v5.6-6; Cohen 1988) package. Sky subtraction was accomplished in the 2D images via a linear fit of the variation of the sky emission in the spatial direction (parallel to the slit). Following this, a simple extraction of the spectra was carried out. No trace of residual sky emission could be detected in the extracted spectra. The extracted spectra were then wavelength calibrated using observations of a Xe arc lamp obtained directly after each exposure (rms residual ∼1 Å). Following wavelength calibration the spectra were rebinned to a uniform wavelength scale of 6.46 Å pixel^{-1} between 4200 and 7500 Å. The spectra were then co-added as described in the previous paragraphs.

The co-added spectra were flux calibrated using observations of the spectrophotometric standard BD+33 2642 (Stone 1977) obtained at 2015 August 29.90 UT (with the same spectrograph configuration and slit width) and are therefore presented in units of F_ν (mJy). Comparison of imaging observations between the calibration night and the LT spectra shows zero-point differences of <0.1 mag (i.e., <10%). The greatest uncertainties in the flux calibration will therefore be due to slit losses caused by seeing variations and misalignment of the object with the slit. We measure this from our repeated observations of the source on the same night to be ∼15%. Hence, we estimate a total flux uncertainty of ∼20%.

B.2. LCOGT 2 m Spectroscopy

We obtained a pair of spectra of the 2015 eruption of M31N 2008-12a using the Floyds spectrograph mounted on the LCOGT 2 m, Hawaii. Floyds uses a low-dispersion grating (235 lines per mm) and a cross-dispersed prism in concert to work in the first and second order simultaneously, allowing for

Table 13
Swift Observations of Nova M31N 2008-12a Following the 2015 Eruption

ObsID[a]	Exp[b] (ks)	Date[c] (UT)	MJD[c] (d)	Δt[d] (d)	UV[e] (mag) uvm2	uvw1	Rate (10^{-2} ct s^{-1})	$L_{0.2-1.0}$[f] (10^{38} erg s^{-1})
00032613104_1	0.11	2015 Aug 28.01	57262.01	−0.27	>18.9	⋯	<8.0	<6.0
00032613096	0.7	2015 Aug 28.01	57262.01	−0.27	⋯	>20.2	<2.0	<1.5
00032613104_2	0.23	2015 Aug 28.40	57262.40	0.12	17.3 ± 0.2	⋯	<4.2	<3.2
00032613097	0.8	2015 Aug 28.41	57262.41	0.13	⋯	17.6 ± 0.1	<2.9	<2.2
00032613104_3	0.12	2015 Aug 28.60	57262.60	0.32	17.0 ± 0.2	⋯	<7.0	<5.2

Notes.
[a] ObsIDs 104 and 105 consisted of four short exposures each immediately prior to ObsIDs 096–103.
[b] Dead-time-corrected XRT exposure time.
[c] Start date of the observation.
[d] Time in days after the eruption on 2015 Aug 28.28 UT (MJD 57262.28; see Section 4.4).
[e] The *Swift* UVOT filter was uvw1 (central wavelength 2600 Å) throughout except for one initial uvm2 (2250 Å) observation consisting of four snapshots.
[f] X-ray luminosities (unabsorbed, blackbody fit, 0.2–10.0 keV) and upper limits were estimated according to Section 4.4.

(This table is available in its entirety in machine-readable form.)

Table 14
X-Ray Model Parameters for the 9 Groups of Spectra Shown in Figure 15 and the High/Low-State Spectra Shown in Figure 9(c)

Group[a]	Blackbody Only			Blackbody Plus Emission Lines					
ID: Days Color	N_H (10^{21} cm^{-2})	kT (eV)	cstat dof	N_H (10^{21} cm^{-2})	kT (eV)	Line energies[b] (keV) (Prominent Nearby Lines[c])			cstat dof
1:6-7 black	$0.6^{+0.7}_{-0.6}$	65^{+13}_{-9}	66 / 88						
2:8 orange	$1.1^{+0.9}_{-1.0}$	82^{+18}_{-12}	66 / 101						
3:9 purple	$4.0^{+1.5}_{-1.1}$	69^{+9}_{-9}	148 / 195	$0.6^{+0.2}_{-0.5}$	123^{+24}_{-13}	$0.52^{+0.03}_{-0.03}$ (N VIIα)	$0.68^{+0.04}_{-0.04}$ (O VIIIα)		115 / 173
4: 10 red	$5.5^{+2.0}_{-0.5}$	75^{+8}_{-12}	185 / 222	$0.3^{+0.4}_{-0.3}$	123^{+37}_{-35}	$0.55^{+0.05}_{-0.04}$ (O VII α)	$0.70^{+0.05}_{-0.06}$ (O VIII α)	$0.86^{+0.04}_{-0.03}$ (O VIII?)	139 / 183
5: 11 blue	$0.9^{+0.6}_{-0.6}$	123^{+16}_{-12}	175 / 229	$0.7^{+0.3}_{-0.3}$	119^{+16}_{-31}	$0.41^{+0.04}_{-0.04}$ (N VI α)	$0.62^{+0.04}_{-0.03}$ (N VII γ)	$0.85^{+0.03}_{-0.03}$ (O VIII?)	115 / 173
6: 12 red	$2.7^{+1.3}_{-0.7}$	96^{+9}_{-13}	172 / 212	$0.7^{+0.4}_{-0.3}$	110^{+6}_{-10}	$0.67^{+0.04}_{-0.04}$ (O VIII α)	$0.76^{+0.05}_{-0.08}$ (O VIII β)	$0.89^{+0.06}_{-0.05}$ (Ne IX α)	115 / 173
7: 13-14 purple	$3.0^{+1.3}_{-1.1}$	87^{+15}_{-12}	136 / 166	$0.7^{+0.4}_{-0.3}$	103^{+14}_{-34}	$0.52^{+0.03}_{-0.06}$ (N VIIα)	$0.73^{+0.03}_{-0.03}$ (O VII?)	$0.92^{+0.08}_{-0.06}$ (Ne IXα)	107 / 133
8: 15 orange	$1.5^{+1.0}_{-0.8}$	106^{+20}_{-15}	108 / 135	$0.8^{+0.9}_{-0.7}$	101^{+18}_{-17}		$0.72^{+0.04}_{-0.05}$ (O VII?)		95 / 124
9: 16-17 black	$0.6^{+0.9}_{-0.6}$	88^{+17}_{-14}	70 / 79						
high red	$4.3^{+0.8}_{-1.1}$	82^{+10}_{-6}	254 / 310	$1.1^{+0.2}_{-1.1}$	118^{+5}_{-7}	$0.56^{+0.04}_{-0.03}$ (O VIIα)	$0.72^{+0.03}_{-0.04}$ (O VII?)	$0.85^{+0.03}_{-0.03}$ (O VIII?)	193 / 265
low blue	$0.0^{+0.4}_{-0.0}$	143^{+11}_{-15}	98 / 136	$1.5^{+3.4}_{-0.6}$	87^{+11}_{-69}	$0.39^{+0.07}_{-0.19}$ (N VI α)	$0.78^{+0.03}_{-0.05}$ (O VIII β)	$0.91^{+0.06}_{-0.05}$ (Ne IX α)	70 / 88

Notes.
[a] Spectral groups are identified by their number and color in Figure 15 and the associated time-span in days post-eruption.
[b] The quoted errors combine the statistical uncertainties, as estimated in XSPEC, and the calibration precision of the *Swift*/XRT energy scale (∼0.02 keV; see Mingo et al. 2016).
[c] Known H-like (C VI, N VII, O VIII, Ne X) and He-like (N VI, O VII, Ne IX) transitions close to the potential emission line energies. These are *not* clear identifications but first tentative suggestions.

3200–10000 Å wavelength coverage in a single exposure. Wavelength calibration is accomplished with a HgAr lamp, and flat fielding with a tungsten–halogen lamp.

These spectra were reduced using the PyRAF-based floyds-spec pipeline, which rectifies, trims, and extracts spectra and performs cosmic-ray removal, fringe correction, wavelength calibration, flux calibration (using a library sensitivity function and observations of a standard star observed on the second night), and telluric correction.

B.3. Kitt Peak National Observatory 4 m Spectroscopy

A spectrum of M31N 2008-12a was obtained on 2015 August 29.38 UT with the KOSMOS (Kitt Peak Ohio State

Multi Object Spectrograph) on the KPNO 4 m telescope. We used the blue VPH grism, a 0″9 slit, and imaged the spectrum onto a E2V CCD detector. An FeAr hollow cathode lamp was used for the wavelength calibration. The resulting spectrum, which has an integration time of 1200 s, a wavelength range of 3806–6628 Å, and a dispersion of 0.689 Å pixel^{-1}, was processed and extracted with standard IRAF software.

APPENDIX C
M31N 2008-12A FINDER CHART

In Figure 19 we provide a finder chart indicating the position of M31N 2008-12a and the 17 photometric calibration stars (see Table 10). The chart is approximately 10′ wide and 5′ high, with north at the top and east to the left.

APPENDIX D
OBSERVATIONS OF THE 2015 ERUPTION OF M31N 2008-12A

The following Tables 11–14 provide full details of the observations and X-ray spectral modeling of the 2015 eruption of M31N 2008-12a.

REFERENCES

Afanasiev, V. L., & Moiseev, A. V. 2005, AstL, 31, 194
Allen, D. A. 1980, MNRAS, 190, 75
Arai, A., Naito, H., Watanabe, F., et al. 2015, ATel, 7979, 1
Arnaud, K. A. 1996, in ASP Conf. Proc. 101, Astronomical Data Analysis Software and Systems V, ed. G. H. Jacoby & J. Barnes (San Francisco, CA: ASP), 17
Balucinska-Church, M., & McCammon, D. 1992, ApJ, 400, 699
Banerjee, D. P. K., Joshi, V., Venkataraman, V., et al. 2014, ApJL, 785, L11
Barnsley, R. M., Jermak, H. E., Steele, I. A., et al. 2016, JATIS, 2, 015002
Barsukova, E., Fabrika, S., Hornoch, K., et al. 2011, ATel, 3725, 1
Bateson, F. M., & Hull, O. 1979, IAUC, 3341
Bessell, M. S. 1979, PASP, 91, 589
Bessell, M. S. 1990, PASP, 102, 1181
Bode, M. F. 2010, AN, 331, 160
Bode, M. F., Darnley, M. J., Beardmore, A. P., et al. 2016, ApJ, 818, 145
Bode, M. F., Darnley, M. J., Shafter, A. W., et al. 2009, ApJ, 705, 1056
Bode, M. F., & Evans, A. (ed.) 2008, Classical Novae, Vol. 43 (2nd ed.; Cambridge: Cambridge Univ. Press)
Bode, M. F., & Kahn, F. D. 1985, MNRAS, 217, 205
Bode, M. F., O'Brien, T. J., Osborne, J. P., et al. 2006, ApJ, 652, 629
Breeveld, A. 2010, SWIFT-UVOT-CALDB-16-R01, Swift Calibration Database http://heasarc.gsfc.nasa.gov/docs/heasarc/caldb/swift/docs/uvot/uvot_caldb_AB_10wa.pdf
Brown, T. M., Baliber, N., Bianco, F. B., et al. 2013, PASP, 125, 1031
Burrows, D. N., Hill, J. E., Nousek, J. A., et al. 2005, SSRv, 120, 165
Cameron, A. G. W. 1959, ApJ, 130, 916
Cardelli, J. A., Clayton, G. C., & Mathis, J. S. 1989, ApJ, 345, 245
Cash, W. 1979, ApJ, 228, 939
Chandrasekhar, S. 1931, ApJ, 74, 81
Chen, H.-L., Woods, T. E., Yungelson, L. R., Gilfanov, M., & Han, Z. 2016, MNRAS, 458, 2916
Chen, T., Lau, K. M., & Xu, Z. 2015, ATel, 7974, 1
Cheung, C. C., Jean, P., & Shore, S. N. 2014, ATel, 5879
Chomiuk, L., Linford, J. D., Yang, J., et al. 2014, Natur, 514, 339
Ciardullo, R., Ford, H. C., Neill, J. D., Jacoby, G. H., & Shafter, A. W. 1987, ApJ, 318, 520
Ciardullo, R., Shafter, A. W., Ford, H. C., et al. 1990a, ApJ, 356, 472
Ciardullo, R., Tamblyn, P., Jacoby, G. H., Ford, H. C., & Williams, R. E. 1990b, AJ, 99, 1079
Cohen, J. G. 1988, in Instrumentation for Ground-Based Optical Astronomy, ed. L. B. Robinson (New York: Springer-Verlag), 448
Connelley, M., & Sandage, A. 1958, PASP, 70, 600
Curtin, C., Shafter, A. W., Pritchet, C. J., et al. 2015, ApJ, 811, 34

Darnley, M. J., Bode, M. F., Harman, D. J., et al. 2014a, in ASP Conf. Proc. 490, Stellar Novae: Past and Future Decades, ed. P. A. Woudt & V. A. R. M. Ribeiro (San Francisco, CA: ASP), 49
Darnley, M. J., Bode, M. F., Kerins, E., et al. 2004, MNRAS, 353, 571
Darnley, M. J., Bode, M. F., Kerins, E., et al. 2006, MNRAS, 369, 257
Darnley, M. J., Henze, M., Shafter, A. W., & Kato, M. 2015a, ATel, 8029, 1
Darnley, M. J., Henze, M., Shafter, A. W., & Kato, M. 2015b, ATel, 7964, 1
Darnley, M. J., Henze, M., Shafter, A. W., & Kato, M. 2015c, ATel, 7980, 1
Darnley, M. J., Henze, M., Shafter, A. W., & Kato, M. 2015d, ATel, 7965, 1
Darnley, M. J., Henze, M., Steele, I. A., et al. 2015e, A&A, 580, A45
Darnley, M. J., Henze, M., Steele, I. A., et al. 2016a, A&A
Darnley, M. J., Hounsell, R. A., & Bode, M. F. 2008, in ASP Conf. Proc. 401, RS Ophiuchi (2006) and the Recurrent Nova Phenomenon, ed. A. Evans et al. (San Francisco, CA: ASP), 203
Darnley, M. J., Kerins, E., Newsam, A., et al. 2007, ApJL, 661, L45
Darnley, M. J., Kuin, N. P. M., Page, K. L., et al. 2016b, ATel, 8587
Darnley, M. J., Ribeiro, V. A. R. M., Bode, M. F., Hounsell, R. A., & Williams, R. P. 2012, ApJ, 746, 61
Darnley, M. J., Ribeiro, V. A. R. M., Bode, M. F., & Munari, U. 2011, A&A, 530, A70
Darnley, M. J., Williams, S. C., Bode, M. F., et al. 2014b, A&A, 563, L9
Darnley, M. J., Williams, S. C., Bode, M. F., et al. 2014c, ATel, 6527, 1
Della Valle, M., Pasquini, L., Daou, D., & Williams, R. E. 2002, A&A, 390, 155
Dilday, B., Howell, D. A., Cenko, S. B., et al. 2012, Sci, 337, 942
Disney, M. J., & Wallace, P. T. 1982, QJRAS, 23, 485
Drake, J. J., Delgado, L., Laming, J. M., et al. 2016, ApJ, 825, 95
Dufay, J., Bloch, M., Bertaud, C., & Dufay, M. 1964, AnAp, 27, 555
Evans, A., Kerr, T., Yang, B., et al. 2007, MNRAS, 374, L1
Evans, A., Bode, M. F., O'Brien, T. J., & Darnley, M. J. (ed.) 2008, in ASP Conf. Proc. 401, RS Ophiuchi (2006) and the Recurrent Nova Phenomenon (San Francisco, CA: ASP)
Fabrika, S., Barsukova, E. A., Valeev, A. F., et al. 2015, ATel, 8033
Freedman, W. L., & Madore, B. F. 1990, ApJ, 365, 186
Gallagher, J. S., & Ney, E. P. 1976, ApJL, 204, L35
Gurevitch, L. E., & Lebedinsky, A. I. 1957, in IAU Symp. 3, Non-stable Stars, ed. G. H. Herbig (Cambridge, UK: Cambridge Univ. Press), 77
Gutierrez, J., Garcia-Berro, E., Iben, I., Jr., et al. 1996, ApJ, 459, 701
Güver, T., & Özel, F. 2009, MNRAS, 400, 2050
Hachisu, I., & Kato, M. 2006, ApJS, 167, 59
Hachisu, I., & Kato, M. 2007, ApJ, 662, 552
Hachisu, I., & Kato, M. 2010, ApJ, 709, 680
Hachisu, I., & Kato, M. 2014, ApJ, 785, 97
Hachisu, I., & Kato, M. 2016, ApJS, 223, 21
Hachisu, I., Kato, M., Kiyota, S., et al. 2008, in ASP Conf. Proc. 401, RS Ophiuchi (2006) and the Recurrent Nova Phenomenon, ed. A. Evans et al. (San Francisco, CA: ASP), 206
Hachisu, I., Kato, M., & Nomoto, K. 1999a, ApJ, 522, 487
Hachisu, I., Kato, M., Nomoto, K., & Umeda, H. 1999b, ApJ, 519, 314
Hachisu, I., Saio, H., & Kato, M. 2016, ApJ, 824, 22
Henze, M., Darnley, M. J., Kabashima, F., et al. 2015a, A&A, 582, L8
Henze, M., Darnley, M. J., Shafter, A. W., et al. 2015b, ATel, 8062, 1
Henze, M., Darnley, M. J., Shafter, A. W., et al. 2015c, ATel, 7984, 1
Henze, M., Meusinger, H., & Pietsch, W. 2008, A&A, 477, 67
Henze, M., Ness, J.-U., Darnley, M. J., et al. 2014a, A&A, 563, L8
Henze, M., Ness, J.-U., Darnley, M. J., et al. 2015d, A&A, 580, A46
Henze, M., Pietsch, W., Haberl, F., et al. 2010, A&A, 523, A89
Henze, M., Pietsch, W., Haberl, F., et al. 2011, A&A, 533, A52
Henze, M., Pietsch, W., Haberl, F., et al. 2014b, A&A, 563, A2
Hernanz, M., & José, J. 2008, NewAR, 52, 386
Hillebrandt, W., & Niemeyer, J. C. 2000, ARA&A, 38, 191
Hillman, Y., Prialnik, D., Kovetz, A., & Shara, M. M. 2015, MNRAS, 446, 1924
Hillman, Y., Prialnik, D., Kovetz, A., & Shara, M. M. 2016, ApJ, 819, 168
Hornoch, K., & Fabrika, S. 2015, ATel, 8038
Hornoch, K., Henze, M., Darnley, M. J., Shafter, A. W., & Kato, M. 2015a, ATel, 7969, 1
Hornoch, K., Kucakova, H., Quimby, R., et al. 2015b, ATel, 7976, 1
Hounsell, R., Bode, M. F., Hick, P. P., et al. 2010, ApJ, 724, 480
Hounsell, R., Darnley, M. J., Bode, M. F., et al. 2016, ApJ, 820, 104
Hubble, E. P. 1929, ApJ, 69, 103
Hurkett, C. P., Vaughan, S., Osborne, J. P., et al. 2008, ApJ, 679, 587
Iijima, T. 2009, A&A, 505, 287
Jester, S., Schneider, D. P., Richards, G. T., et al. 2005, AJ, 130, 873

José, J. 2016, Stellar Explosions: Hydrodynamics and Nucleosynthesis (Boca Raton, FL, USA: CRC/Taylor and Francis)
José, J., & Shore, S. N. 2008, in Classical Novae, ed. M. F. Bode & A. Evans (2nd ed.; Cambridge: Cambridge Univ. Press)
Joy, A. H. 1954, ApJ, 120, 377
Joy, A. H., & Swings, P. 1945, ApJ, 102, 353
Kato, M., Saio, H., & Hachisu, I. 2015, ApJ, 808, 52
Kato, M., Saio, H., Hachisu, I., & Nomoto, K. 2014, ApJ, 793, 136
Kato, M., Saio, H., Henze, M., et al. 2016, ApJ, 830, 40
Kerins, E., Darnley, M. J., Duke, J. P., et al. 2010, MNRAS, 409, 247
Korotkiy, S., & Elenin, L. 2011, CBAT, IAU, http://www.cbat.eps.harvard.edu/unconf/followups/J00452885+4154094.html
Kotani, T., Kawai, N., Yanagisawa, K., et al. 2005, NCimC, 28, 755
Kovetz, A., & Prialnik, D. 1994, ApJ, 424, 319
Kraft, R. P. 1964, ApJ, 139, 457
Kramida, A., Ralchenko, Yu., Reader, J. & N.I.S.T. ASD Team 2015, NIST Atomic Spectra Database (ver. 5.3), [Online]. Available: http://physics.nist.gov/asd [2016, July 7]., National Institute of Standards and Technology, Gaithersburg, MD.
Krautter, J. 2008, in ASP Conf. Proc. 401, RS Ophiuchi (2006) and the Recurrent Nova Phenomenon, ed. A. Evans et al. (San Francisco, CA: ASP), 139
Litvinchova, A. A., Pavlenko, E. P., & Shugarov, S. Y. 2011, Ap, 54, 36
Lomb, N. R. 1976, AP&SS, 39, 447
Maguire, K., Taubenberger, S., Sullivan, M., & Mazzali, P. A. 2016, MNRAS, 457, 3254
Maoz, D., Mannucci, F., & Nelemans, G. 2014, ARA&A, 52, 107
Massey, P., Neugent, K. F., & Smart, B. M. 2016, arXiv:1604.00112
Massey, P., Olsen, K. A. G., Hodge, P. W., et al. 2006, AJ, 131, 2478
Massey, P., Olsen, K. A. G., Hodge, P. W., et al. 2011, AJ, 141, 28
Mingo, B., Pagani, C., Beardmore, A., et al. 2016, SWIFT-XRT-CALDB-04, Swift Calibration Database, http://heasarc.gsfc.nasa.gov/docs/heasarc/caldb/swift/docs/xrt/xrt_gain_CALDB-04_v16.pdf
Moore, C. E. 1945, CoPri, 20, 1
Moro-Martín, A., Garnavich, P. M., & Noriega-Crespo, A. 2001, AJ, 121, 1636
Mróz, P., Udalski, A., Poleski, R., et al. 2016, ApJS, 222, 9
Munari, U., Ribeiro, V. A. R. M., Bode, M. F., & Saguner, T. 2011, MNRAS, 410, 525
Ness, J., Starrfield, S., Beardmore, A. P., et al. 2007, ApJ, 665, 1334
Ness, J.-U. 2010, AN, 331, 179
Ness, J.-U., Beardmore, A. P., Osborne, J. P., et al. 2015, A&A, 578, A39
Ness, J.-U., Osborne, J. P., Henze, M., et al. 2013, A&A, 559, A50
Ness, J.-U., Schaefer, B. E., Dobrotka, A., et al. 2012, ApJ, 745, 43
Nishiyama, K., & Kabashima, F. 2008, CBAT, IAU, http://www.cbat.eps.harvard.edu/iau/CBAT_M31.html#2008-12a
Nishiyama, K., & Kabashima, F. 2012, CBAT, IAU, http://www.cbat.eps.harvard.edu/unconf/followups/J00452884+4154095.html
Norton, A. J., Wynn, G. A., & Somerscales, R. V. 2004, ApJ, 614, 349
Nussbaumer, H., Schmid, H. M., & Vogel, M. 1989, A&A, 211, L27
Nussbaumer, H., Storey, P. J., & Storey, P. J. 1982, A&A, 113, 21
O'Brien, T. J., Bode, M. F., & Kahn, F. D. 1992, MNRAS, 255, 683
O'Brien, T. J., Bode, M. F., Porcas, R. W., et al. 2006, Natur, 442, 279
O'Brien, T. J., & Kahn, F. D. 1987, MNRAS, 228, 277
Orio, M., Rana, V., Page, K. L., Sokoloski, J., & Harrison, F. 2015, MNRAS, 448, L35
Orlando, S., Drake, J. J., & Laming, J. M 2009, A&A, 493, 1049
Osborne, J. P. 2015, JHEAp, 7, 117
Osborne, J. P., Page, K. L., Beardmore, A. P., et al. 2011, ApJ, 727, 124
Overbeek, D., McNaught, R. H., Whitelock, P., Cragg, T., & Verdenet, M. 1987, IAUC, 4395
Page, K. L., Osborne, J. P., Evans, P. A., et al. 2010, MNRAS, 401, 121
Page, K. L., Osborne, J. P., Kuin, N. P. M., et al. 2015, MNRAS, 454, 3108
Pagnotta, A., & Schaefer, B. E. 2014, ApJ, 788, 164
Pagnotta, A., Schaefer, B. E., Clem, J. L., et al. 2015, ApJ, 811, 32
Piascik, A. S., Steele, I. A., Bates, S. D., et al. 2014, Proc. SPIE, 9147, 8
Pickering, E. C., & Fleming, W. P. 1896, ApJ, 4, 369
Pietsch, W. 2010, AN, 331, 187
Pietsch, W., Fliri, J., Freyberg, M. J., et al. 2005, A&A, 442, 879
Pietsch, W., Haberl, F., Sala, G., et al. 2007, A&A, 465, 375
Pietsch, W., Henze, M., Haberl, F., et al. 2011, A&A, 531, A22
Poole, T. S., Breeveld, A. A., Page, M. J., et al. 2008, MNRAS, 383, 627
Pottasch, S. R. 1967, BAN, 19, 227
Pravec, P., Hudec, R., Soldán, J., Sommer, M., & Schenkl, K. H. 1994, ExA, 5, 375
Prialnik, D., & Kovetz, A. 1995, ApJ, 445, 789
Prialnik, D., Shara, M. M., & Shaviv, G. 1978, A&A, 62, 339

R Development Core Team 2011, R: A Language and Environment for Statistical Computing (Vienna, Austria: R Foundation for Statistical Computing)
Raman, C. V. 1928, Indian J. Phys., 2, 387
Rauch, T., Orio, M., Gonzales-Riestra, R., et al. 2010, ApJ, 717, 363
Ribeiro, V. A. R. M., Bode, M. F., Darnley, M. J., et al. 2009, ApJ, 703, 1955
Ribeiro, V. A. R. M., Bode, M. F., Darnley, M. J., et al. 2013, MNRAS, 433, 1991
Ribeiro, V. A. R. M., Darnley, M. J., Bode, M. F., et al. 2011, MNRAS, 412, 1701
Ritchey, G. W. 1917, PASP, 29, 210
Roming, P. W. A., Kennedy, T. E., Mason, K. O., et al. 2005, SSRv, 120, 95
Rosino, L., & Iijima, T. 1987, in RS Ophiuchi (1985) and the Recurrent Nova Phenomenon, ed. M. F. Bode (Utrecht: VNU Science Press), 27
Rupen, M. P., Mioduszewski, A. J., & Sokoloski, J. L. 2008, ApJ, 688, 559
Sanford, R. F. 1949, ApJ, 109, 81
Scargle, J. D. 1982, ApJ, 263, 835
Schaefer, B. E. 2005, ApJL, 621, L53
Schaefer, B. E. 2010, ApJS, 187, 275
Schaefer, B. E., Pagnotta, A., LaCluyze, A. P., et al. 2011, ApJ, 742, 113
Schaefer, B. E., Pagnotta, A., Xiao, L., et al. 2010, AJ, 140, 925
Schatzman, E. 1949, AnAp, 12, 281
Schatzman, E. 1951, AnAp, 14, 294
Schmid, H. M. 1989, A&A, 211, L31
Schwarz, G. J., Ness, J.-U., Osborne, J. P., et al. 2011, ApJS, 197, 31
Shafter, A. W. 2015, ATel, 7968, 1
Shafter, A. W. 2016, arXiv:1606.02358
Shafter, A. W., Bode, M. F., Darnley, M. J., et al. 2011a, ApJ, 727, 50
Shafter, A. W., Darnley, M. J., Hornoch, K., et al. 2011b, ApJ, 734, 12
Shafter, A. W., Henze, M., Rector, T. A., et al. 2015a, ApJS, 216, 34
Shafter, A. W., Hornoch, K., Ciardullo, J. V. R., Darnley, M. J., & Bode, M. F. 2012, ATel, 4503, 1
Shafter, A. W., Horst, J. C., & Darnley, M. J. 2015b, ATel, 7967, 1
Shafter, A. W., & Irby, B. K. 2001, ApJ, 563, 749
Shafter, A. W., Rau, A., Quimby, R. M., et al. 2009, ApJ, 690, 1148
Shara, M. M., Doyle, T., Lauer, T. R., et al. 2016, arXiv:1602.00758
Shore, S. N., De Gennaro Aquino, I., Scaringi, S., & van Winckel, H. 2014, A&A, 570, L4
Shore, S. N., Kenyon, S. J., Starrfield, S., & Sonneborn, G. 1996, ApJ, 456, 717
Shore, S. N., Sonneborn, G., Starrfield, S. G., et al. 1991, ApJ, 370, 193
Skopal, A., Pribulla, T., Buil, C., Vittone, A., & Errico, L. 2008, in ASP Conf. Proc. 401, RS Ophiuchi (2006) and the Recurrent Nova Phenomenon, ed. A. Evans et al. (San Francisco, CA: ASP), 227
Skrutskie, M. F., Cutri, R. M., Stiening, R., et al. 2006, AJ, 131, 1163
Sokoloski, J. L., Rupen, M. P., & Mioduszewski, A. J. 2008, ApJL, 685, L137
Soraisam, M. D., Gilfanov, M., Wolf, W. M., & Bildsten, L. 2016, MNRAS, 455, 668
Sostero, G., & Guido, E. 2006a, IAUC, 8673
Sostero, G., & Guido, E. 2006b, IAUC, 8681
Sostero, G., Guido, E., & West, J. D. 2006, CBET, 502
Stark, A. A., Gammie, C. F., Wilson, R. W., et al. 1992, ApJS, 79, 77
Starrfield, S., Iliadis, C., & Hix, W. R. 2008, in Classical Novae, ed. M. F. Bode & A. Evans (2nd ed.; Cambridge: Cambridge Univ. Press)
Starrfield, S., Iliadis, C., & Hix, W. R. 2016, PASP, 128, 051001
Starrfield, S., Iliadis, C., Timmes, F. X., et al. 2012, BASI, 40, 419
Starrfield, S., Sparks, W. M., & Truran, J. W. 1985, ApJ, 291, 136
Starrfield, S., Truran, J. W., Sparks, W. M., & Kutter, G. S. 1972, ApJ, 176, 169
Steele, I. A., Smith, R. J., Rees, P. C., et al. 2004, Proc. SPIE, 5489, 679
Stone, R. P. S. 1977, ApJ, 218, 767
Strope, R. J., Schaefer, B. E., & Henden, A. A. 2010, AJ, 140, 34
Tang, S., Bildsten, L., Wolf, W. M., et al. 2014, ApJ, 786, 61
Tang, S., Cao, Y., & Kasliwal, M. M. 2013, ATel, 5607, 1
Tarasova, T. N. 2009, ARep, 53, 203
Tatischeff, V., & Hernanz, M. 2007, ApJL, 663, L101
Taylor, A. R., Davis, R. J., Porcas, R. W., & Bode, M. F. 1989, MNRAS, 237, 81
Tody, D. 1993, in ASP Conf. Proc. 52, Astronomical Data Analysis Software and Systems II, ed. R. J. Hanisch, R. J. V. Brissenden, & J. Barnes (San Francisco, CA: ASP), 173
van Rossum, D. R. 2012, ApJ, 756, 43
van Rossum, D. R., & Ness, J. 2010, AN, 331, 175
Wallerstein, G., & Garnavich, P. M. 1986, PASP, 98, 875
Walter, F. M., Battisti, A., Towers, S. E., Bond, H. E., & Stringfellow, G. S. 2012, PASP, 124, 1057

Wang, B., & Han, Z. 2012, NewAR, 56, 122
Watanabe, M., Takahashi, Y., Sato, M., et al. 2012, Proc. SPIE, 8446, 84462O
Whelan, J., & Iben, I., Jr. 1973, ApJ, 186, 1007
White, N. E., Giommi, P., Heise, J., Angelini, L., & Fantasia, S 1995, ApJL, 445, L125
Williams, B. F., Garcia, M. R., Kong, A. K. H., et al. 2004, ApJ, 609, 735
Williams, R. 2012, AJ, 144, 98
Williams, R. E. 1992, AJ, 104, 725
Williams, R. E., Phillips, M. M., & Hamuy, M. 1994, ApJS, 90, 297
Williams, S. C., Darnley, M. J., Bode, M. F., Keen, A., & Shafter, A. W. 2014, ApJS, 213, 10
Williams, S. C., Darnley, M. J., Bode, M. F., & Shafter, A. W. 2013, ATel, 5611

Williams, S. C., Darnley, M. J., Bode, M. F., & Shafter, A. W. 2016, ApJ, 817, 143
Williams, S. C., Shafter, A. W., Hornoch, K., Henze, M., & Darnley, M. J. 2015, ATel, 8234
Wilms, J., Allen, A., & McCray, R. 2000, ApJ, 542, 914
Wolf, W. M., Bildsten, L., Brooks, J., & Paxton, B. 2013, ApJ, 777, 136
Worters, H. L., Eyres, S. P. S., Bromage, G. E., & Osborne, J. P. 2007, MNRAS, 379, 1557
Woudt, P. A., & Ribeiro, V. A. R. M. (ed.) 2014, in ASP Conf. Proc. 490, Stella Novae: Past and Future Decades (San Francisco, CA: ASP)
Wright, A. E., & Barlow, M. J. 1975, MNRAS, 170, 41
Yaron, O., Prialnik, D., Shara, M. M., & Kovetz, A. 2005, ApJ, 623, 398
Zacharias, N., Finch, C. T., Girard, T. M., et al. 2013, AJ, 145, 44